Laser Pulse Propagation in Plasmas and its implication on frequency up-shift and electron acceleration

PhD thesis

Naveen Chandra Pathak

Academic Supervisor:
Prof. Danilo Giulietti

CNR Co-supervisor:
Dr. Luca Labate

Scuola di Dottorato Galileo Galilei
Dipartimento di Fisica, E. Fermi
Largo Bruno Pontecorvo, 3, Ed. C
University of Pisa
56127 Pisa, Italy

March, 2011

Abstract

This thesis documents the study of elementary processes in interaction of intense, ultrashort laser pulses with underdense plasmas. Main objective of this thesis is to understand the basic phenomena resulting from the interaction of ultra-short ultra-intense laser pulses with matter and to study the mechanism which eventually leads to generation of high energetic electrons, in laser based plasma accelerators. In a broad prospective, the work here can be described as a detailed experimental and numerical study of laser matter interaction, plasma formation and acceleration of particles. The motivation for these experiments arises from the fact that the results are relevant from both fundamental and applied research point of view.

The light matter interaction is basically associated with the behaviour of individual atom exposed to high fields. The knowledge of this behaviour is important, as the basic interaction mechanism between laser and matter eventually drives the overall physical mechanism of the investigated phenomena. For this purpose numerical simulation based on optical field ionization was developed. These calculations yield information about the plasma density distribution within a given experimental conditions. The knowledge of the electron density distribution and its dynamics is very useful in interpreting many observed phenomena during the experiment. When working with short pulse laser systems, possible pre-pulses that precedes the main pulse have to be taken into account. The numerical study on ionization is further extended for the inclusion of the pre-pulse effect in high intense pulses.

One of the important feature during the experimental work is the use of time domain interferometry. This allowed to freeze the dynamics of the electron density evolution on femtosecond time scales up to several picoseconds. This was done by taking the snapshots of the process initiated by the main laser pulse by another pulse (called probe pulse) in terms of fringe shift.

With ultrashort and high intense laser pulses the physical behaviour of the medium changes drastically in a time comparable or shorter than the pulse duration. This ultrafast change in the physical properties of the medium induces spatial and spectral modification in the propagating laser pulses. Study of these modifications could enhance the understanding

of how intense optical pulses propagates in plasmas. Search for stable propagation of intense laser pulses in underdense plasmas and study of their spectrum modification was one of the most important work during the experiments.

High energetic electrons with good bunch parameters have been successfully generated during the first phase of the experiment at LNF, with the newly built FLAME laser system. The main objective of the new facility at LNF is to push the electron energy to GeV scale and to find ways for new compact radiation sources.

The present work is motivated by the need to gain understanding of laser pulse propagation in plasmas and its implications on electron acceleration by high-intensity laser irradiation of gas targets and their application. The results, in particular the frequency shift of the laser pulse, have taken a further step towards a broad application of laser gas interaction in a large variety of fields like accelerator physics and supercontinuum generation.

Acknowledgements

Foremost, I would like to thank Prof. Danilo for my integration in his group and allowing me to work in a nice scientific environment. These three years I spend as a part of ILIL laboratory proved to be very helpful for me in developing new scientific skills.

I owe special thanks to Dr. Antonio for his encouragement and care during my stay in the lab. His patient attitude and enthusiam was great. His friendly attitude keeps things going easy even in most difficult situations.

I owe special thank to Dr. Leonida for providing every opportunity to work and learn. He is one of the most dynamic and motivated person in the group. His never-give-up attitude is an excellent example for everyone.

I am highly indebted to Dr. Moreno and Prof. Konishi for their encouragement and advices.

I am very greatful to Paolo Tomassini, Luca and Carlo who sets everything for me to start on my project. I gained a lot from there experience and expertise. I learned useful things from Carlo on experimental side. My sincere thanks go to Giancarlo, Petra, Andrea, Sergio, Orlando, Francesco and Leonardo for their valuable support. Each one of them has something special to learn. Thanks to Walter, Antonella and Maouro for their technical support during the experiments.

Two people with whom I enjoyed every moment in Pisa are Tadzio and Bechir. They helped me in all spheres of life. I am fortunate to have friends like them. One thing we all admire during our discussions was philosophy. The time I spend with them will remain as a golden memorable moments in my life.

My special thanks go to Prof. H. Ruhl for allowing the use of PSC code.

I would like to acknowledge the UNIPI science promotion fund for financial support in the form of Galileo-Galilei scholarship. I am thankful to Illaria Fierro, secretary of Galieo-Galilei PhD school, for her valuable help in all administrative processes. I also acknowledge

Istituto Nazionale di Fisica Nucleare (INFN) for the financial support to attend experiment at LNF in the framework of the PLASMON-X Project.

The social life in Pisa has been wonderful with many friends - Lam, Rebecca, Peter, Yung Guo, Nayam, Sergei, Andrea, Fariborz, Daniele, Bjarke, Ruzhen, Antonio and Kim. Thanks are also due to numerous other friends in Pisa and in India.

Finally, I would like to thank all my family members for their unfailing love and support, which helped me to work motivatedly. Above all, I thank almighty God for providing me strength, motivation and courage.

Contents

List of Figures

List of Tables

Part I

Introduction

CHAPTER 1

Laser based plasma accelerators: Introduction and motivation

Lasers are one of the most significant inventions of the twentieth century. When laser made its debut in 1960 [1], it was called a solution looking for a problem. At that time, different groups across the world were working to understand the behaviour of matter, particularly atom, in the presence of an external applied field. Lasers provided and excellent source of high field to boost up these studies to a new level. The invention of pulsed lasers opened exciting research opportunities in the field of laser-matter interaction.

The initial free running laser oscillators were first Q-switched and later mode-locked to provide high peak power in nanosecond or picosecond duration pulses. After that, for about one and a half decades, there was not much progress in pushing up of the laser power. The last two decades have witnessed an outstanding development of ultrashort laser technologies and consequently, a completely multidisciplinary field has emerged, known as ultra-fast phenomena sciences. Dramatic breakthroughs have led to the advent of new solid-state laser sources that can deliver pulses as short as few tens of femtosecond. The implementation of the Chirped Pulse Amplification (CPA) technique [2, 3], for the amplification of short pulses, has opened up new opportunities for innovative approaches in the domain of ultrashort ultra-intense field physics. These ultrashort pulses allow to reach very intense fields [4]. For instance, a laser pulse with energy of 100 mJ in 100 fs pulse duration corresponds to a power of 1 TW $(10^{12}\mathrm{W})$. When focused to a diameter of $10\mu\mathrm{m}$, it gives an intensity close to $3 \times 10^{18}\mathrm{W/cm^2}$. Thus, ultra-short laser pulses can deposit a certain amount of laser energy in a very small area in a very short time interval and opens a completely new regime of laser-matter interaction, which is complex but rich in physics [5].

Plasma physics is one of the major scientific fields to use these lasers. A major impetus was provided by the proposal of initiating fusion reactions for viable energy production using high power laser beams [6, 7, 8, 9, 10]. This quest still continues. Along the way, however, the field has branched into a number of exciting research areas and particle acceleration is one of them [11, 12, 13, 14].

From the beginning, nature and its constitution remains one of the great mysteries to resolve for the human being. The quest for understanding the fundamental laws of nature brought several discoveries and inventions in science and technology. The most distinguished experiment to understand the structure of atom was done by Ernest Rutherford in 1909. By analysing the nature of the collision between the target and projectile the basic structure of the atom has been found. To look deep inside the matter it is required to overcome the large force created by the constituents of the matter. Accelerator physics gets its origin from the quest to generate such energetic particles to probe the atomic structure and became an outstanding tool to answer some of the most remarkable questions about the nature of the universe.

In present days, particle accelerators are one of the largest machines built by humans. It is among the main tool for elementary particle research from last five decades. The conventional particle accelerators are now approaching to their limits. In the conventional accelerators such as LINACs, the acceleration gradients are limited to some tens of MV/m due to material break down considerations [15]. Consequently, as the energy gain of particles is the product of such gradient times the acceleration distance, one is obliged to extend the acceleration distance in order to reach high energies. This is why these tools for high energy physics are becoming larger and larger and increasingly more expensive.

It was realized by Tajima and Dawson [11] way back in 1979 that a laser beam propagating in plasma can excite electron plasma waves, which being longitudinal can be used to accelerate electrons. To understand the rationale for plasma-based acceleration, consider the limits of conventional particle accelerators based on radio-frequency waves propagating in metallic cavities. They are limited first by the availability of high peak power drivers and ultimately by electrical breakdown of the metal structure. Due to these inevitable features in conventional accelerators their accelerating gradient is limited to 20-100 MV/m. Plasmas, on the other hand are not limited by material breakdown consideration as they are already ionized and indeed support huge electric field of the order of 10-100 GV/m. Consequently, with regard to the energy gain of particles in accelerators, a plasma accelerator can cut

(a) (b)

Figure 1.1: The figure shows the fundamental difference between the laser based particle accelerators and the conventional accelerators. (a) Plasma produced by an intense laser pulse incident on a gas jet. The length of the plasma column or accelerating structure is 4 mm. The bright column support hundreds of GV/m accelerating gradient (b) Satellite view of LHC at CERN. The radius of the accelerating structure is 4.3 KM. The laser based plasma accelerators potentially reduces the dimension of the accelerating structures by many orders of magnitude and still provides high quality energetic particles.

down significantly the acceleration distance to boost particles to several MeV over a short distance below the millimetre range and still provide a good quality electron beam. Thus, plasma based particle acceleration opened a new and exciting field of extreme gradient beyond 1 TV/m. Fig. 1.1 illustrate the difference in the size of accelerating structure between laser based plasma accelerators and conventional accelerators.

In last two decades there has been a tremendous progress in laser based plasma accelerators due to the advances in technology [16, 17, 18], particularly by the development of compact terawatt laser systems based on the technique of chirped-pulse amplification. One of the most remarkable developments brought by the invention of CPA was that it enabled construction of table-top terawatt lasers, employing high energy storage materials such as Ti:Sapphire and Nd:glass, and leading to a significant progress in the techniques of short pulse generation. Typical parameters of this class of laser system are: few hundreds of mJ energy in a single pulse of multi femtosecond duration, delivering multi terawatt peak power, which is high enough to reach laser intensities of the order of $10^{20}\mathrm{W}/\mathrm{cm}^2$ at the focus. Due to the significant decrease in energy consumption as compared to megajoule laser facilities, these devices fits very well in small laboratories and enable researchers to create and study extreme condition of light matter interaction on small scale environment.

The basic principle of particle acceleration using laser or charged particles beams is as follows: A plasma as a whole is electrically neutral, containing equal amounts of negative

charge (electrons) and positive charge (ions). A pulse from an intense laser or particle beam, however, creates a disturbance in the plasma. In essence, the beam pushes the lighter electrons away from the heavier positive ions, which in turn get left behind, creating a region of excess positive charge and a region of excess negative charge. This separation of positive and negative charges produces a large electric field that points from the positive to the negative charge region. This high electric field travels through the plasma as a wave, trailing in the wake of the light pulse at nearly the speed of light, and accelerates any charged particles that comes under its influence [19]. There are several variants of plasma-based accelerators [20]. The most widely investigated are plasma wakefield accelerator, plasma beat wave accelerator and laser wakefield accelerator including the self-modulated ones.

The plasma-based accelerators in which the plasma wave is driven by one ore more electron beams are referred to as the plasma wakefield accelerators (PWFAs) [21]. In the PWFA, the plasma wakefield can be excited by a relativistic electron beam provided that the electron beam has a shorter spatial extent than the plasma period.

In the plasma beat wave accelerator (PBWA), two long pulse laser beams of nearly equal frequency are used to resonantly excite an electron plasma wave [22]. This is done by beating the laser beams such that the difference in the frequencies is equal to the plasma frequency. The laser exerts a longitudinal ponderomotive force on the plasma electrons and resonantly drives a plasma wave.

In the laser wakefield accelerator (LWFA), a single short and high intensity laser pulse drives a plasma wave [23]. The wakefield is driven most efficiently when the laser pulse length is equal to the plasma wavelength.

The self-modulated LWFA uses a single short high intensity laser pulse, as in the standard LWFA. The self-modulated LWFA, however, operates at higher densities than the standard LWFA, such that the laser pulse length is long compared to the plasma wavelength and the laser power is somewhat larger than the critical power for relativistic guiding [24]. In this high density regime, the laser pulse undergoes a self-modulation instability, which causes the pulse to become axially modulated at the plasma period. Among all the different versions of the plasma-based accelerators, LWFA (including the Sm-LWFA) is the most successful one.

In addition to the above acceleration mechanisms, direct laser acceleration of electrons in a plasma of relatively higher density have been reported [25, 26]. A laser of finite spot size and pulse duration ($\tau > 2\pi\omega_p^{-1}$) exerts a radial ponderomotive force on plasma elec-

trons and pushes them out of the laser column, creating a radial electric field due to the stationary ion space charge. The energetic electrons, due to their higher relativistic mass, experience a smaller ponderomotive force and execute betatron oscillations under the space charge electric field. Their motion along the laser axis produces an azimuthal magnetic field, reinforcing the betatron oscillations. The electron velocity due to betatron oscillations couples with the magnetic field of the laser to exert an axial Lorentz force on the electrons at frequency $\omega - \omega_b$ and wave number k, where ω and k are the frequency and wave vector of the laser and ω_b is the betatron frequency. When the electron axial velocity v_z equals the phase velocity of this Lorentz force $\omega - \omega_b = kv_z$, or the Doppler shifted laser frequency (as seen by the relativistic electrons) equals the betatron frequency, resonant energy exchange occurs between the laser and the electrons.

At very high intensity ($\geq 10^{19}\mathrm{Wcm}^{-2}$), a new scenario of mono-energetic electron acceleration with energy spread $\leq 3\%$ is emerging. Particle-in-cell simulations of laser-plasma interaction with pulse duration short enough and with very high intensity reveal that an electron evacuated ion bubble is formed at the rear of the laser pulse [27, 28]. The electron density at the backward point of the bubble piles up to form a double layer. Electrons in this pile can be accelerated by the bubble space charge to high energy while focusing in phase space, forming mono-energetic electron beam.

The acceleration of electrons using a single laser pulse was first demonstrated by Nakajima et. al. in 1995 [29]. In that experiment electrons with energy up to 18 MeV were observed using externally injected electrons with initial energy of 1 MeV. The experiment was done with a 1 ps, 3 TW laser pulse at high electron density ($\sim 10^{19}\mathrm{cm}^{-3}$) in self-modulated laser wakefield acceleration regime. The first experimental observation of LWFA was done by Amiranoff et. al. with an externally injected electron beam [30, 31]. This scheme of external injection of electrons was not very practical due to low coupling efficiency between the injected electrons (generated from RF-cavities) and the plasma-based accelerating structures. The first experiment on acceleration of self-injected electrons has been demonstrated by self modulated laser wakefield acceleration mechanism [32]. A laser pulse longer than the plasma period undergoes the self modulation, and eventually leads to the generation of large amplitude wakefields and self-trapping of electrons into plasma accelerating structures via wave-breaking. Many experiments on the generation of MeV electrons and measurement of the acceleration gradient have been reported [33, 34, 35]. In the experiment [36] electron acceleration up to 30 MeV was achieved in a length of about 1 cm, giving the acceleration

gradient of 0.03 GeV/cm. In a recent experiment [35], the direct measurement of real acceleration gradient has been shown. By employing a tomographic diagnosis, the acceleration of monoenergetic electrons from 5 MeV to 55 MeV in a distance of 200μm is reported.

Earlier experiments on electron acceleration showed a wide width in electron energy spectra. In 2004 breakthrough in this direction has achieved and a beam of monoenergetic electrons has been experimentally produced by three groups [37, 38, 39]. Mangles et. al. have observed 25 MeV and 75 MeV electrons with less than 3% energy spread by impinging a 0.8μm, $2.5 \times 10^{18}\mathrm{W/cm^2}$, 40 fs, laser pulse of 12μm spot size on helium gas at electron density $n_e = 2.3 \times 10^{19}\mathrm{cm^{-3}}$. Faure et. al. have observed beam of 170 MeV energy by a similar mechanism. Geddes et. al. have reported 80 MeV electron beam with less than 1% energy spread using a preformed plasma channel guiding. The acceleration in these experiments is believed to occur in so called "bubble regime" [27]. This bubble has been seen to be formed behind a high power short laser pulse in plasmas and it is completely devoid of electrons. This is sometime also referred as an ion channel. However, this type of ion channel is different from the one observed by Durfee et. al. [40]. This ion channel lasts only for few ps while the one observed in [40] lasts for few ns. The electrons initially pushed by the laser ponderomotive force, collide at the base of this bubble and a bunch of electrons is injected into the bubble as seen in simulations. These electrons are accelerated inside the bubble and show a monoenergetic energy spectrum. The observation of monoenergetic electrons in laser plasma interaction has revived the hope of replacing the large size conventional accelerators by compact tabletop laser plasma accelerators.

There are two important parameters governing the length over which acceleration can take place, these are **(1) plasma density**, which control the dephasing length and **(2) the interaction length** [1], which is normally equal to the Rayleigh length. Since dephasing length is inversely proportional to plasma density, higher plasma density gives shorter dephasing length and consequently smaller energy gain. The interaction length or Rayleigh length is the length up to which the laser pulse remains intense enough to drive a plasma wave. The useful acceleration length is the shortest of these two lengths. When the laser pulse energy is not high enough, normally, to have high intensity the pulse is focused to a very small spot

[1] In principle there is another parameter known as pump depletion length. It is defined as the distance over which the laser pulse energy depleted significantly. After that the pulse cannot excite plasma waves. The effective interaction length is the shortest among dephasing length, pump depletion length and Rayleigh length.

size. This limits the interaction length up to few microns and eventually limits the energy gain by surfing particles. With the development of high power laser systems, energies up to few Joules are now available and the pulse needs not to be focused to a very small spot size for high intensities. This extends the interaction length and also maintains the intensity of the laser pulse up to several hundreds microns. In experiments, the dephasing length was controlled by changing the backing pressure of the gas-jet and the interaction length was extended by using a high ”F” number focusing optics or by pre-formed plasma channelling.

After the generation of quasi-monoenergetic electron bunches the other important parameters which need to be controlled are bunch quality, stability and reproducibility. A major breakthrough in this effort was achieved by Faure et. al. in 2006 by controlled injection of electrons into plasma wakefields using colliding laser pulses [41]. In all previous experiments the electron self-injection was relied on self-trapping via wave-breaking which was not actually a controlled way of particle injection. With the use of a second, injecting, laser pulse tunability of the electron bunch energy and stability were achieved with high accuracy. At a broader prospective the performance, stability and good out-put of laser based plasma accelerator depend on laser and plasma parameters. For laser systems these are laser energy, pulse length, power, focusability, pointing stability and contrast ratio between main and pre-pulse. For the plasma these can be plasma density, temperature and their profile.

The experimental work done in the last two decades have shown that the outstanding and competing features (low emittance, high bunch charge) of laser-accelerated electron beams promise their use in a large variety of applications. The beams can be used as a diagnostic tool in basic plasma research, e.g. for the diagnostics of electromagnetic fields in dense plasmas with picosecond time resolution. Laser-accelerated electrons could be applied as compact particle accelerators, as a driver for neutron production [42], for radio-isotope generation [43, 44], for table-top nuclear physics [45], for the generation of intense x-rays [46] or even for medical applications as a compact radiotherapy system for tumor treatment. In addition to this practical advantage, it is of great interest to investigate the applications of particular characteristics of the electron beams generated in plasmas, such as the high density (4 or 5 orders of magnitude greater than in RF bunches) and the short temporal duration of the electron bunches, derived from the shortness of the laser pulse. Furthermore, the application of such electron bunches can be pushed to explore terahertz (THz) radiation generation [47]. As a THz radiation source, LWFA may provide not only a compact apparatus compared to conventional accelerators, but also electron bunches with much

shorter duration and hence higher THz frequencies. Synchrotron radiation from LWFA was demonstrated experimentally and has been studied by many authors [48, 49, 50]. Although conventional synchrotron light sources can generate very high energy photons, this few KeV ultrafast x-ray radiation could provide a powerful tool for femtosecond x-ray diffraction or absorption spectroscopy. By using an undulator, LWFA driven XUV FEL could be designed. For all kind of applications, stability and reproducibility of electron bunches remain the key issues and there are still many things to be addressed for the applications. With the continuous development in technology, understanding of the physical mechanism and commissioning of new high power laser facilities across many laboratories around the world, it can be expected that these applications can be realized in the near future.

1.1 Thesis structure

This PhD dissertation is a report of an experimental study on particle generation with high intensity lasers. Most of the work described in this thesis has been carried out at the Intense Laser Irradiation Laboratory in Pisa [Italy], lead by Dr. L. A. Gizzi. This laboratory belongs to the Unit of Pisa (headed by Dr. A. Giulietti) of the National Institute of Optics of the italian National Research Council (CNR). Part of the work was also carried out at the Laboratori Nazionali di Frascati of the Italian National Institute for Nuclear Physics (INFN), in the framework of the INFN project PLASMONX (whose national representative is currently Prof. Danilo Giulietti). The purpose of these experiments were to study the propagation of intense laser pulses in plasmas and to efficiently generate high energetic electrons. This manuscript is divided into five parts:

Part-I provides introduction to laser based plasma accelerators. Their scientific context and competitiveness over conventional accelerators is discussed briefly.

Part-II is dedicated to basic concepts and terminology used in laser plasma interaction studies. With simple mathematical expressions, the physical mechanism of particle generation and their acceleration is described.

Part-III describes the ionization model used in this thesis. A quantitative knowledge of ionization of neutral gases with intense laser pulse helps in understanding and interpreting many physical processes during interaction (propagation) of laser pulses with gases (plasmas).

Part-IV describes the experiment on electron acceleration with moderate power laser system. The salient feature of the experiment was generation of supercontiuum from laser gas interaction. It is for the first time that the new frequency generation has been observed from gases in such a large extent and recorded spatially (spatial variation of frequency with propagation of laser pulse in plasmas) as well.

Part-V presents the preliminary experiment on electron acceleration with very high power laser system under commissioning at LNF. Finally, a summary of the observed results will be given and how these studies can and should be extended in the near future will conclude this manuscript.

Part II

Basic concepts and physical mechanism of laser based plasma accelerator

CHAPTER 2

Generation of ultra-short laser pulses

2.1 Outline

Laser plasma interaction physics is one of the most rich, innovative and well established branch in physics. The inclusion of ultra-intense ultrashort lasers is, however, relatively quite recent. This chapter is devoted to the physics and technology concerned with the generation of ultrashort laser pulses that was triggered by the invention of laser mode-locking, one of the most striking interference phenomena in nature. Simultaneous oscillation of large number of highly coherent, phase-locked longitudinal modes in a laser yields a resultant field equal to zero most of the time except for very short intervals [51]. As a result of constructive interference between the oscillating waves, the entire energy of the radiation field is concentrated within these short periods. As a consequence, laser mode-locking leads to the formation of a short light pulse circulating in the resonator. Each time the pulse hits a partially reflecting mirror, a small portion of its energy is coupled out of the oscillator, resulting in a train of ultrashort pulses at the out-put of the mode-locked laser.

Section 2.2 of this chapter is concerned with the generation of ultrashort laser pulses and in Section 2.3 amplification of the short pulses is described.

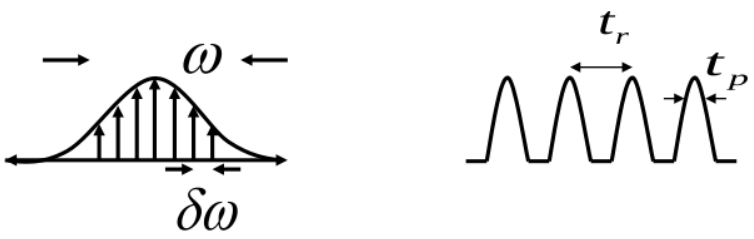

Figure 2.1: Schematic of laser emission and mode-locked laser output. (a) represents the oscillations of the modes locked in constant phase in frequency domain. (b) represents the output pulses in time domain. The pulses are separated by the round trip time, t_r, of the cavity and t_p is the pulse duration.

2.2 Ultrashort light pulse generation

The development of compact table-top tera-watt laser systems delivering intense, ultra-short pulses relies on two major advancement in technology. One is the chirped pulse amplification (CPA) [2, 3] developed in mid eighties and the other is Kerr-lens mode-locking [52] of the Ti:Sapphire oscillator developed in early nineties. Today, most of the compact high power lasers are based on Ti:Sapphire oscillators. Apart from the obvious advantages of being a solid state laser in comparison to the dye-based lasers of the earlier generation, Ti:Sapphire has several other advantages such as large lasing bandwidth, very good thermal conductivity and excellent mechanical properties.

A cavity consisting of a gain medium normally yields output in continuous wave operation where intensity is constant in time. If, however, the energy emitted by the cavity can be compressed into short temporal duration, the resulting pulse would have much higher peak power and can result in high intensity upon focusing. In order to generate very short pulses the Ti:Sapphire laser relies on the process of Kerr-lens mode-locking. It involves phase locking of a large number of longitudinal modes (i.e. wavelengths whose half-integral multiples equal the cavity length) of the laser. The frequency spacing $(\Delta\omega)$ between two adjacent modes is the inverse of the round trip time $(t_r = \frac{c}{2L})$ in the cavity (Fig.2.1).

The large number of constant phase locked modes in frequency domain corresponds to an infinite series of short pulses [53], spaced by t_r in the time domain. This effect occurs due to the interference between various modes and one can show this effect by a simple

calculation. Let us consider N frequency modes locked in phase, with central frequency ω_0 and the mode spacing $\Delta\omega$. The resultant electric field and intensity are given by

$$E(t) = \Sigma e^{i(\omega_0 + n\Delta\omega t)} = \frac{e^{iN\Delta\omega t} - 1}{e^{i\Delta\omega t} - 1} e^{i\omega_0 t} \tag{2.1}$$

$$I(t) = |E(t)|^2 \approx \frac{sin^2(N\Delta\omega t/2)}{sin^2(\Delta\omega t/2)} \tag{2.2}$$

The intensity profile is thus a series of pulses whose width is determined by the number of modes that are locked in phase. A large number of phase locked modes implies a large bandwidth $(N\Delta\omega)$ and hence a shorter pulse width $t_p \sim 1/N\Delta\omega$ with higher peak power.

In order for a laser to operate preferentially in mode-locked (short-pulse) state in contrast to normal continuous lasing (i.e. free running), one needs a device to switch from the normal state to the mode-locked one. Before the advent of Kerr-lens mode-locking, the switching action could only be achieved by introducing an additional element in the cavity to provide a time-dependent loss mechanism $-$ a saturable absorber or an acousto-optic modulator. A large number of lasers still operate in this fashion, usually in the picosecond regime. The duration of the pulse in such a laser is typically determined by the speed at which the time-dependent loss mechanism can be switched between the 'on' and 'off' state.

In a Kerr-lens mode-locked laser, such a switch is essentially inherent and instantaneous by mapping on to the spatial domain. It is a process that takes advantage of the non-linear effect of self-focusing. For high intensity pulse propagation through the lasing medium, the refractive index is no longer a constant (as in the case of low intensity laser) but is intensity dependent. The non-linear intensity-dependent refractive index in the optical elements of the laser cavity is given by

$$n = n_0 + n_2 I(r) \tag{2.3}$$

Thus, the refractive index varies over radial (transverse) direction of the beam such that the crystal acts as a lens. This non-linear effect due to dependence of the intensity on transverse spatial coordinates of the laser beam is called ***self-focusing***. Thus, for a Gaussian shaped beam passing through a material, with the beam more intense at the center than at the edges, the index of refraction for the material will become higher at the center than at the edges of the beam, thereby effectively creating a lens that in turn slightly focuses the beam within the material. The path length that the beam traverses and the beam intensity will determine how much focusing occurs before the beam emerges from the material.

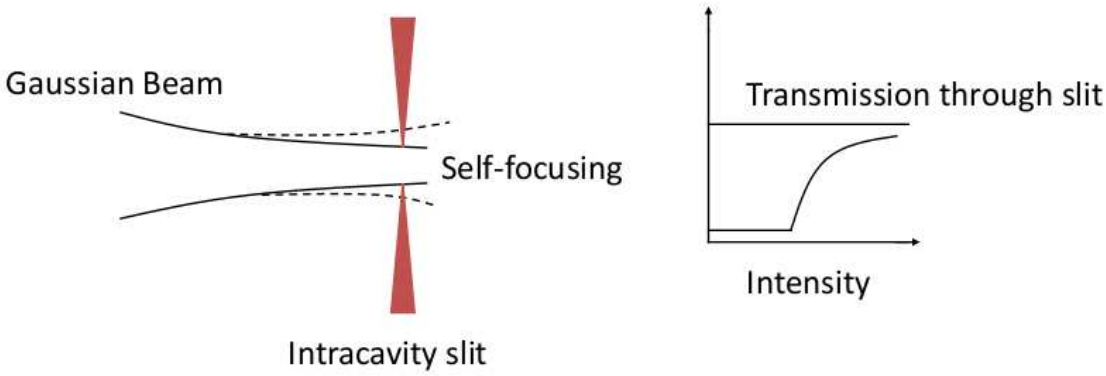

Figure 2.2: Schematic of KLM for achieving mode-locking. (a) shows a Gaussian laser beam passing through a solid state gain material. The normal continuous wave propagation is shown with dashed lines. A small aperture is placed in the path of the laser beam to provide high loss to the continuous wave mode. (b) shows the transmission of the pulse as a function of intensity. High intensity pulse undergoes self-focusing which reduces its diameter and hence transmission of the beam increases.

In Kerr lens mode-locking, the self-focusing effect is used to preferentially select the mode-locked set of modes that provide short-pulses, rather than a single steady-state continuous wave (cw) mode. Due to this effect, short pulse operation leads to a smaller beam radius than cw operation. By placing a slit of suitable size at an appropriate location, the loss in the cavity for cw operation can be selectively increased while there is no attenuation for a short pulse (Fig. 2.2), which constitutes a fast saturable absorber effect. Under such circumstances, the laser operates in the pulsed mode. The laser pulses obtained in this way are as short as few femtosecond.

The seeding of a high intensity pulse relies either on a spike due to noise, or external intervention in the form of cavity modulation to enforce the coupling of the phases of different modes. This is usually achieved by vibrating an optical element in the cavity. After the initial seeding, successive passes in the cavity improve the mode locking leading to even shorter pulse width and higher peak intensity and after a few round trips laser settles into a stable pulsed operation. The stable limit to pulse width is due to combination of opposing tendencies of group velocity dispersion on one hand and the cavity compensation of such

dispersion on the other. A pair of prism is usually employed for adjustable dispersion compensation, and recently dispersion-compensated mirrors have also been used. Pulses as short as 5 fs in duration have been generated using this technique, which essentially consist of just a couple of oscillations of the light electric (magnetic) field. For a more detailed discussion on generation of short laser pulses the reader can refer to [54, 55].

2.2.1 Pulse amplification

The short pulse generated in an oscillator has a very little amount of energy associated with it, usually of the order of nano-joule. Thus, these short pulses need to be amplified. Prior to the advent of the chirped-pulse amplifiers, the architecture for high power solid-state laser systems consisted of an oscillator that produced a seed pulse of several nanosecond or picosecond duration, followed by an amplifier or amplifier chain that multiplied the seed pulse energy by several orders or magnitude. This architecture had restricted the peak power densities to a few GWcm^{-2} in the final amplifier. The path to even higher output intensities is blocked by the self-focusing effect, which can ruin the amplifier medium. Thus, whilst in the case of generation of short pulses the non-linear refractive index and the self-focusing is an asset, it is certainly not the case for amplification.

The problem is overcome by the chirped-pulse amplification technique, in which the pulse is first stretched in time by several orders of magnitude (without loss of bandwidth). This is called chirping of the pulse. The chirped pulse has an increased pulse width and hence a lower peak intensity. This permits the use of large gain amplifier systems. After the amplification, the pulse is recompressed to nearly its original pulse duration and consequently, a very high intensity pulse is obtained. In order to use this scheme, it is necessary to stretch and then recompress the pulse without the loss of bandwidth and without distortion.

However, subsequent amplification in a chirped-pulse amplification chain will result in a substantial lengthening of the ouput pulses owing to gain narrowing and uncompensated phase errors (as the femtosecond pulses are amplified or propagated through optical components they become lengthened and lose their shape). Maintaining a certain pulse duration after any form of propagation or amplification requires the use of a dispersion compensating technique or device. Various dispersion compensation mechanisms exits, including prisms, gratings etc. A novel approach to dispersion control using an acousto-optic modulator has also been invented. The commercially available Dazzler is an example of such an acousto-optic programmable dispersion filter (AOPDF) [56]. Dazzlers have been used

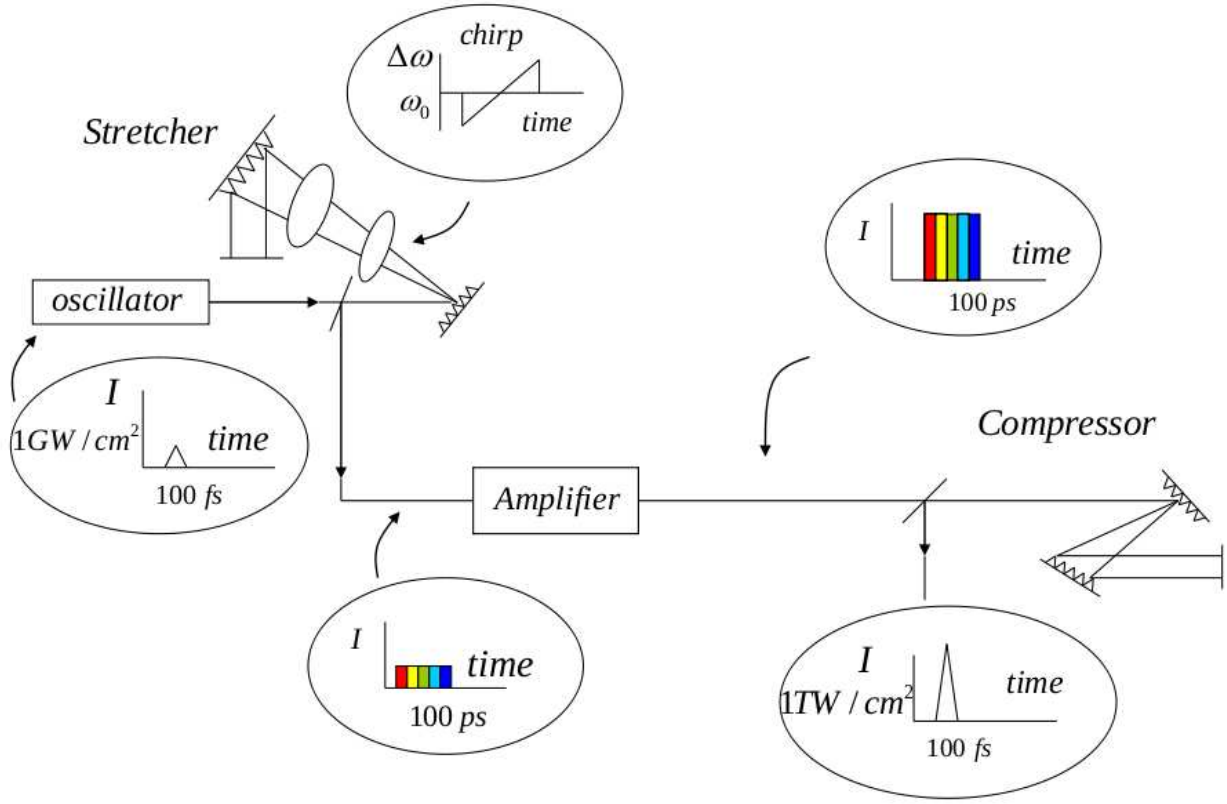

Figure 2.3: Schematic of CPA system, indicating pulse width and intensity at different stages of amplification.

in the amplification chain of short pulse lasers to control dispersion. AOPDF offer great flexibility and range of control of dispersion. A complete description of AOPDF is beyond the scope of the present work. Excellent literature, illustrating the process in detail can be found elsewhere [57, 58].

In a CPA system, the limit on the attainable intensity is decided by the maximum energy and lowest pulse duration. The maximum energy extracted from an amplifier system would in turn depend upon the damage threshold of the amplifying medium for the stretched pulse. It also depends on the saturation fluence. The typical values of the damage threshold for amplifying media used in a CPA systems vary from $10 - 20\mathrm{GWcm}^{-2}$. Practically, lasers are operated much below the damage threshold in order to avoid beam distortion due to the non-linear part of the refractive index. A schematic of a typical chirped pulse laser amplification scheme is shown in figure 2.3.

CHAPTER 3

Interaction of intense laser light with plasmas

3.1 Outline

In this chapter we focused on certain fundamental aspects of the laser-plasma interaction process. The purpose of this chapter is to give some of the nomenclature commonly used in laser plasma interaction studies. The basic definition of plasma and its characteristics are discussed in section 3.2. Section 3.3 briefly introduces the formation and propagation of electromagnetic and electrostatic waves in a collision-less, unmagnetized plasma, assuming a linear response of the medium. Absorption of laser light in plasma is given in section 3.4. In section 3.5 and 3.6 the interaction of free electrons with electromagnetic waves (both in non-relativistic and relativistic case) and the generation of ponderomotive force is described. Finally, in section 3.7 nonlinear optical phenomena associated with laser pulse in plasmas are discussed.

3.2 Plasma: An introduction

The general accepted definition of plasma is a collection of ionized matter that admits quasi-neutrality and exhibits collective behaviour [59]. The term quasi-neutrality implies ionized assembly is neutral enough so that the electron and ion charge densities are approximately equal over a large scale. Collective behaviour implies existence of long ranged electromagnetic force in a large collection of charged particles. Then the motion depends not only on local conditions, but on state of plasma in remote regions as well [60]. These requirements can also be equivalently put in terms of the following criteria on a collection of charged particles. Such a collection should have spatial dimension larger than the characteristic scale length λ_D, known as Debye length. It should exist for temporal duration greater than the characteristic time scale ω_p^{-1}, known as plasma frequency. Finally, such a collection should consists of an assembly large enough that it can be statistically treated i.e. number of particles in a sphere of Debye radius should be very large. A collection that satisfies the above conditions is defined as plasma.

One of the most important parameter in the study of a plasma is plasma frequency, ω_p. This characterizes its response to the external fields. Under normal conditions in plasma, which is a collection of electrons and ions, it is assumed that the ions are a background of charges which neutralizes the unperturbed plasma. In this case a perturbation is applied in space only to the electrons. Due to this externally applied perturbation the electrons in a plasma are displaced from a uniform background of ions, and an electric field is created in the plasma. The electric field sets up in such a way to restore the neutrality of the plasma by pulling the electrons back to their original positions. However, due to their inertia, the electrons will overshoot and oscillate around their equilibrium positions with a characteristic frequency known as plasma frequency. We can derive an expression for plasma frequency with assumptions of T=0 and B=0 i.e. cold, collisionless plasma with no externally applied magnetic fields. The plasma is infinite in extent and the electron motions occur only in the x-direction. As a consequence of the last assumption, we have $\nabla = \hat{x}\partial/\partial x, \mathbf{E} = E\hat{x}, \nabla \times \mathbf{E} = 0$ and $\mathbf{E} = -\nabla\phi$. The electron equation of motion and continuity are:

$$m_e n \left(\frac{\partial \mathbf{v}}{\partial t} + (\mathbf{v} \cdot \nabla)\, \mathbf{v} \right) = -en\mathbf{E} \tag{3.1}$$

$$\frac{\partial n}{\partial t} + \nabla \cdot (n\mathbf{v}) = 0 \tag{3.2}$$

Expanding the dependent variables into an equilibrium part and a perturbation as: $n =$

$n_0 + n_1, v = v_0 + v_1$ and $E = E_0 + E_1$ in equation 3.1 and 3.2, ignoring the cross terms higher than first order and assuming perturbations to vary sinusoidally, i.e. $\exp[\mathrm{i}(\mathrm{kx} - \omega \mathrm{t})]$, one can obtain the dispersion relation in this linear low amplitude limit as

$$\omega = \left(\frac{ne^2}{m_e \varepsilon}\right)^{1/2} = \omega_p \tag{3.3}$$

This frequency is the characteristic of electron-plasma oscillations and depends only on the electron density, independent of wave vector (k). The inverse of ω_p is the response time of the plasma electrons to perturbing fields. For example, if an electromagnetic wave of frequency ω is incident on a plasma, the electrons will not be able to shield the electromagnetic field if $\omega > \omega_p$, i.e. if the time period of the electromagnetic oscillation is smaller than the response time of the plasma electrons. Such a plasma is said to be underdense and it allows electromagnetic wave to propagate through it. However, if the plasma has higher density such that $\omega_p > \omega$, then the plasma electrons respond fast enough and reflect the electromagnetic wave. Such a plasma is termed as overdense. The density at which $\omega = \omega_p$, is called critical density of plasma.

In laser produced plasmas, the plasma density varies with the distance from the target. Since the refractive index of plasma varies according to the relation

$$\eta = \sqrt{1 - \frac{\omega_p^2}{\omega^2}} \tag{3.4}$$

the refractive index is unity for vacuum and decreases as the density increases and ultimately becomes zero at critical density. At this density, the laser light undergoes total internal reflection.

3.3 Waves in plasmas

Having examined the characteristic charge density oscillations, which are supported by a plasma, let us now consider other waves supported by the plasma, and how the plasma modifies the propagation of electromagnetic waves. We will continue to assume that there is no externally applied (or self-generated) magnetic field present in the plasma. We begin with the linearized plasma response to a high frequency field of the form

$$\mathbf{E} = \mathbf{E}(\mathbf{x}) exp(-i\omega t) \tag{3.5}$$

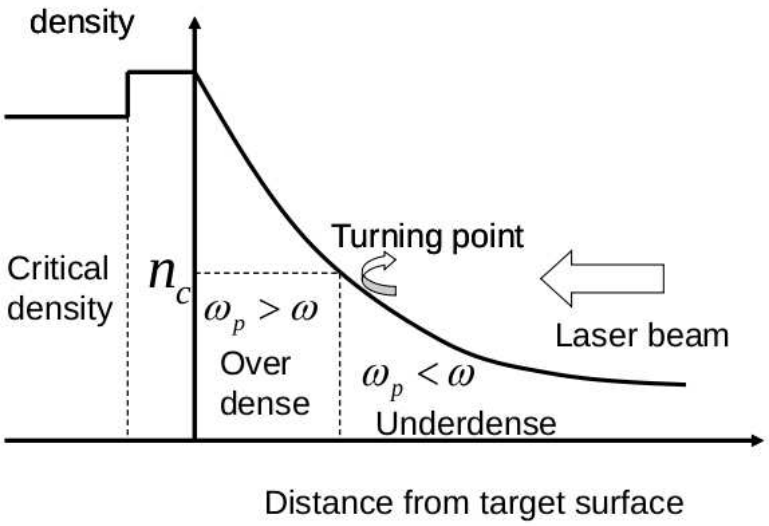

Figure 3.1: Schematic of the typical electron density profile in laser-produced plasma.

Since the frequency of the field is greater than the plasma frequency, the ions are treated as stationary. The linearized equation of motion of the electron can be written as

$$\frac{\partial \mathbf{v}}{\partial t} = -\frac{e}{m}\mathbf{E} \tag{3.6}$$

Since the current density is given as $J = -nev$ one can write

$$\frac{\partial \mathbf{J}}{\partial t} = -ne\frac{\partial \mathbf{v}}{\partial t} = \frac{ne^2}{m}\mathbf{E} \tag{3.7}$$

hence

$$\mathbf{J} = \frac{ine^2}{m\omega}\mathbf{E} = \sigma\mathbf{E} \tag{3.8}$$

where, $\sigma = \frac{ine^2}{m\omega}$, is the frequency dependent conductivity. To develop the wave equation for an oscillating electric and magnetic field, we consider Faraday and Ampere's laws, which give

$$\nabla \times \mathbf{E} = i\omega\mathbf{B} \tag{3.9}$$

and

$$\nabla \times \mathbf{B} = \mu_0\mathbf{J} + \frac{1}{c^2}\frac{\partial \mathbf{E}}{\partial t} \tag{3.10}$$

substituting for σ in above equations, one can arrive at

$$\nabla \times \mathbf{B} = -\frac{i\omega}{c^2}\varepsilon\mathbf{E} \tag{3.11}$$

where $\varepsilon = 1 - \frac{\omega_p^2}{\omega^2}$ defines the dielectric function of the plasma. Taking curl of equation 3.9, substituting from equation 3.10 and using standard vector identity gives

$$\nabla^2 \mathbf{E} - \nabla(\nabla \cdot \mathbf{E}) + \frac{\omega^2}{c^2}\varepsilon \mathbf{E} = 0 \tag{3.12}$$

A similar analysis can be carried out for the magnetic field, which gives

$$\nabla^2 \mathbf{B} + \frac{1}{\varepsilon}\nabla\varepsilon \times (\nabla \times \mathbf{B}) + \frac{\omega^2}{c^2}\varepsilon \mathbf{B} = 0 \tag{3.13}$$

Now let us consider waves associated with electron motion, which are allowed by equations 3.12 and 3.13.

3.3.1 Electromagnetic waves

Let us derive the dispersion relation for electromagnetic waves in plasma with a uniform density. Since $\nabla\varepsilon = 0$ and $\nabla \cdot \mathbf{E} = 0$, the wave equation for E and B becomes identical. Assuming a spatial dependence of exp(ikx), then equation 3.9 gives the dispersion relation for electromagnetic waves in a plasma as

$$\frac{\omega^2}{c^2}\varepsilon = k^2 \tag{3.14}$$

or

$$\omega^2 = \omega_p^2 + k^2 c^2 \tag{3.15}$$

The wave vector k is real only if $\varepsilon > 0$, i.e. $\omega > \omega_p$. This condition can also be written as the requirement that $n < n_c$, here n_c is the critical density and is given as

$$n_c = \frac{1.1 \times 10^{21}}{\lambda^2} cm^{-3} \tag{3.16}$$

where λ is the free-space wavelength of light in $\mu\mathrm{m}$. Thus, inside a plasma electromagnetic wave can only propagate in the underdense region and reflected back from the critical density. The critical density for the 800 nm laser light is $1.7 \times 10^{21}\mathrm{cm}^{-3}$.

3.3.2 Electron plasma waves

The electrostatic electron plasma wave corresponds to the condition $\nabla \times E = 0$. This yields $\varepsilon = 0$. Then the definition of ε gives $\omega = \omega_p$. Thus in cold, collision-less approximation the electrons only oscillate at a well defined frequency and there is no wave propagation

as ω does not depend on the wave-vector. However, the inclusion of thermal effects leads to the modification of dispersion relation for electron plasma oscillation and hence allows wave propagation.

At a finite temperature, the equation of motion for electrons in the linear theory acquires an additional term $-\nabla p_e$. Under the adiabatic assumption, we have $\nabla p_e = \gamma KT\nabla n$, with $\gamma = 3$ in the one dimensional case. Hence, the equation of motion now becomes

$$m_e n\frac{\partial \mathbf{v}}{\partial t} = -en\mathbf{E} - 3KT\nabla n \tag{3.17}$$

From equation of continuity, we have

$$\frac{\partial \rho}{\partial t} + \nabla \cdot \mathbf{J} = 0 \tag{3.18}$$

or,

$$\frac{\partial n}{\partial t} + \nabla \cdot (n\mathbf{v}) = 0 \tag{3.19}$$

Now, taking time derivative of equation 3.17 and using equation 3.19, we have

$$\frac{\partial^2 \mathbf{v}}{\partial t^2} = -\frac{e}{m}\frac{\partial \mathbf{E}}{\partial t} - \frac{3KT}{m_e n}\nabla(\nabla \cdot n\mathbf{v}) \tag{3.20}$$

Now substituting $\frac{\partial}{\partial t} = -i\omega$ and $\nabla = ik$ in equation 3.20, we have

$$v = \frac{-i\omega e}{m_e(\omega^2 - 3v_{th}^2 k^2)}E \tag{3.21}$$

where $v_{th}^2 = \frac{KT}{m_e}$.

In a homogeneous plasma, assuming an electric field varying sinusoidally and using $J = -env = \sigma E$, the expression for the conductivity in case of longitudinal electrostatic modes with k parallel to E is

$$\sigma = \frac{ine^2}{m}\frac{\omega}{(\omega^2 - 3k^2 v_{th}^2)} \tag{3.22}$$

Again, following the equations 3.9 to 3.11, the dielectric function now takes the form

$$\varepsilon = 1 - \frac{\omega_p^2}{(\omega^2 - 3k^2 v_{th}^2)} \tag{3.23}$$

and the dispersion relation obtained from $\varepsilon = 0$ is

$$\omega^2 = \omega_p^2 + 3k^2 v_{th}^2 \tag{3.24}$$

and now has a temperature dependence. The frequency depends on k, and the group velocity is finite. The existence of such electrostatic electron plasma waves also called Langmuir waves has been know experimentally since 1920's [61], however the detailed theory of wave propagation and excitation was developed in late 1940's by Bohm and Gross [62].

3.4 Laser light absorption in plasmas

Interaction of laser pulses with matter involves several physical issues. When a laser pulse is incident on a material, the first question that arises is how this laser energy is coupled to the material or plasma so formed. This question kept theoreticians busy for many years. Several elegant theories have been developed in this regard. A wide range of excellent material is available to understand the physical mechanism of laser light absorption in plasmas [63, 64, 65]. The most instinctive mechanism for the dissipation of laser energy is via collision between electrons and ions. This mechanism is more dominant in case of long duration pulses or very high density plasmas. Significant absorption is, however, possible even in collisionless or weakly collisional plasmas. In this section we will briefly summarise some of the basic laser energy absorption mechanisms in underdense plasmas formed by pulses of femtosecond duration.

3.4.1 Collisionless absorption mechanism

The interaction of ultra-short intense laser pulses with plasmas is quite a complicated physical phenomena. At high intensities, the motion of the electrons oscillating in the field of light wave is relativistic. On the other hand, the ions, due to their inertia, cannot respond to such high frequency field and remains practically stationary. The Coulomb collision cross-section σ, according to the Rutherford formula, is proportional to v^{-4}, so that the collision frequency, $\nu_{e,i} = nv\sigma$, varies as v^{-3} or as $T_e^{-3/2}$, where v is the electron thermal velocity, T_e is the electron temperature and n is the number density. Thus, with increase in T_e or v, the collision frequency decreases, which is opposite the situation for collisions with neutral particles. A collision-less plasma is thus best achieved by increasing the temperature. At high intensities, the plasma temperature is high enough, so that one cannot explain the absorption by inverse bremsstrahlung mechanism.

With this discrepancy, alternative mechanisms were sought for the intense laser light absorption in palsmas, which did not rely on collisions between electrons and ions. The best known mechanism is resonance absorption [66]. In the case of resonance absorption, a p-polarized light wave tunnels through the critical density surface $n_e = n_c$, where it excites a plasma wave. This wave grows over a number of laser periods and is eventually damped either by collisions at low intensities or by particle trapping and wave breaking at high intensities.

For a large density scale length ($L \gg \lambda$), the resonance absorption occurs in a small range of incident angles. However, in the case of short pulses where the density scale length is small ($L \ll \lambda$), the laser light is practically very close to the critical density for large ranges of incident angles. Hence, the resonance absorption occurs over a broad range of angles of incidence. In short, one can say that the angle dependence of the resonance absorption almost vanishes in the case of the short pulses. However, at large intensities, even a combination of these two absorption mechanisms (inverse bremsstrahlung and resonance absorption) failed to predict the observed absorption in the experiments [63]. This was due to the presence of other absorption mechanisms at higher intensities, as well as nonlinear effects that arises when the motion of the electrons in the laser field becomes relativistic.

In summary, inverse bremsstrahlung and resonance absorption can be the dominant absorption mechanisms for intensities $10^{13} \leq I\lambda^2 \leq 10^{17}$ and scale length as small as 0.1λ. In fact, they can even contribute to the total absorption past these intensities but they will not be the dominant mechanism.

3.4.2 Brunel effect or vacuum heating

This absorption mechanism was first discussed by Brunel in 1987 [67] and is also know as vacuum heating. This effect is related to the ”classical” resonance absorption, in that the electric field of the laser light drives electrons across a density gradient. The difference between the two is that in classical resonance absorption, the laser light is assumed to be incident on a gently increasing plasma density (i.e. the scale length of the density gradient is many laser wavelengths). The electric field of the laser can drive a large plasma wave at the turning point resonantly. In vacuum heating, where the density gradient scale length is taken to be much less than the wavelength of the light, no such resonance exists. Therefore, the laser light non-resonantly couples into an electrostatic plasma wave. Since the electric field associated with an intense laser pulse is quite large, a significant amount of energy can be transferred to the plasma electrons. In fact, this is one of the main mechanisms for absorption of laser light in plasmas at high density. If the density scale length is sufficiently small, and the laser is sufficiently intense, vacuum heating occurs when the excursion of an electron in the driven wave at the vacuum plasma interface is so large that it is literally pulled out into vacuum, and then sent into the plasma with random phase.

3.4.3 Absorption by parametric decay process

In general terms, a parametric instability is one that produces growing oscillations frequency (ω_1) in a system whose parameters are modulated at a frequency ($\omega_0 \neq \omega_1$) different from the pump frequency (ω_0). In plasma, it generally refers to a process in which a large amplitude incident wave (the pump wave) provides the driving oscillations and excites other waves within the plasma. Such instabilities provide a mechanism through which the incident laser light, acting as a pump wave, may feed energy into other waves. If the latter are longitudinal waves, they get absorbed in the plasma, thereby heating it. If they are electromagnetic waves, which propagates out of the plasma, they may enhance the scattering of the incident light and have an adverse effect on absorption.

There are four main parametric processes. These are: parametric decay instability, stimulated Brillouin scattering, stimulated Raman scattering and two-plasmon decay instability [68].

Parametric decay instability

In this case, the incident electromagnetic wave (laser) decays parametrically into an electron plasma wave and an ion-acoustic wave. Both these plasma waves decay by Landau damping (collision-less) or collisional damping processes. Thus the energy of the electromagnetic wave is transferred to the plasma.

The energy conservation relation for this process gives

$$\omega = \omega_p + \omega_{ia} \tag{3.25}$$

$$\omega = \omega_p \left(1 + \frac{3k_p^2 v_{th}^2}{\omega_p^2}\right)^{1/2} + k_{ia} c_s \geq \omega_p \tag{3.26}$$

$$\Rightarrow \qquad \omega_p \leq \omega \qquad \text{or} \qquad n_e \leq n_c \tag{3.27}$$

Thus, parametric decay instability takes place up to the critical density.

Stimulated Brillouin scattering

Stimulated Brillouin scattering has the potential of causing large premature reflection of the incident laser light before it reaches the critical density [68]. The incident laser light decays into an ion-acoustic wave and a reflected electromagnetic wave which can leave the plasma. The physical mechanism of this process is as follows. An initial low frequency

density perturbation produces a transverse current, due to the oscillatory motion of electrons in the laser electric field (E_0). This transverse current produces a reflected light wave with field E_R. The ponderomotive force $E_0 E_R$ of incident and reflected wave can in turn cause enhancement in the original density perturbation and thus further growth. The energy conservation for this process gives

$$\omega = \omega_{scattered} + \omega_{ia} \tag{3.28}$$

$$\omega = \omega_p \left(1 + \frac{k_s^2 c^2}{\omega_p^2}\right)^{1/2} + k_{ia} c_s \geq \omega_p \tag{3.29}$$

$$\Rightarrow \qquad \omega_p \leq \omega \qquad \text{or} \qquad n_e \leq n_c \tag{3.30}$$

i.e. this process takes place up to the critical density.

Stimulated Raman scattering

In stimulated Raman scattering the incident laser light decays into an electron plasma wave and a scattered electromagnetic wave. The feedback mechanism is similar to that for the stimulated Brillouin scattering, except that now the density fluctuation is associated with a high frequency electron plasma wave. Energy conservation in this process gives

$$\omega = \omega_{scattered} + \omega_p \tag{3.31}$$

$$\Rightarrow \qquad \omega_p \leq \frac{\omega}{2} \qquad \text{or} \qquad n_e \leq \frac{n_c}{4} \tag{3.32}$$

i.e. this process takes place up to quarter-critical density.

Two-plasmon decay

At the quarter-critical density, a second process called the two plasmon decay instability can compete with Raman scattering. In this case, the incident laser light decays into two electron plasma waves (Plasmon). From energy conservation we have

$$\omega = \omega_{p1} + \omega_{p2} \tag{3.33}$$

$$\Rightarrow \qquad \omega_p \leq \frac{\omega}{2} \qquad \text{or} \qquad n_e \leq \frac{n_c}{4} \tag{3.34}$$

3.5 Interaction of free electrons with EMWs and origin of the ponderomotive force

The dynamics of the electron motion under the influence of electromagnetic radiation, for a non-relativistic case, is given by the Lorentz equation

$$\frac{d\mathbf{p}}{dt} = m_e \frac{d\mathbf{v}}{dt} = -e\left(\mathbf{E} + \mathbf{v} \times \mathbf{B}\right) \tag{3.35}$$

where $\mathbf{E}$ denotes the electric field and $\mathbf{B}$ the magnetic field associated with the electromagnetic wave. $\mathbf{v}$ and $\mathbf{p}$ represents the velocity and momentum of the electron. In non-relativistic case, i.e. $v \ll c$, the effect of the magnetic field can be neglected and the equation of motion is reduced to

$$\frac{d\mathbf{p}}{dt} = -e\mathbf{E} \tag{3.36}$$

Consider a plane electromagnetic wave with an electric field given by

$$\mathbf{E}(\mathbf{r}, t) = \mathbf{E}_0 \cdot cos(\omega t - \mathbf{k} \cdot \mathbf{r}) \tag{3.37}$$

The electron oscillates under the influence of the electric field. The oscillatory velocity of the electron is given by

$$v = \frac{eE_0}{m_e \omega} \tag{3.38}$$

The time averaged energy acquired by the electron as a result of this oscillatory motion is

$$U_p = \frac{e^2 E_0^2}{4 m_e \omega^2} \tag{3.39}$$

This energy is more commonly known as ponderomotive energy. In practical units it is given as

$$U_p = 9.33 \times 10^{-14} \left(I\lambda^2\right) eV \tag{3.40}$$

where λ is in micron and I is in $\mathrm{Wcm^{-2}}$. For a pulse of wavelength $0.8\mu\mathrm{m}$ and intensity $10^{18}\mathrm{Wcm^{-2}}$ the ponderomotive energy is around 59.7 KeV. The quantity $I\lambda^2[\mathrm{W}\mu\mathrm{m}^2\mathrm{cm}^{-2}]$ is known as irradiance. Many of the effects in laser plasma interaction depend upon the laser irradiance, which means that the threshold intensity for a given phenomena can vary depending upon the laser wavelength. Thus, to give an electron an oscillation energy U_p of 1 KeV, we need a $1\mu m$ laser with $I = 10^{16}\mathrm{Wcm^{-2}}$ or a $0.248\mu\mathrm{m}$ laser with $I = 1.6 \times 10^{17}\mathrm{Wcm^{-2}}$.

In practical conditions, due to the radial intensity profile of the laser pulse the electric field is far from being a homogeneous plane wave. For a Gaussian intensity distribution, the peak intensity is achieved on the beam axis and a gradient across the field distribution is present. This gradient leads radially to an additional force and hence, acceleration of the quivering electrons into the direction of lower intensity. This force is known as ponderomotive force.

To derive a simple formula for ponderomotive force, consider a plane electromagnetic wave travelling in the z-direction, but with a radial intensity dependence, which we will assume to be in y-direction. The strength of the E-field may vary due to focusing $(i.e. E_0(y, z = 0) = E_{0,max} exp(-y^2/w^2)$ with a Gaussian width w and peak electric field strength of $E_{0,max}$, hence

$$\mathbf{E}(\mathbf{r}) = E_y(y, z).\hat{e_y} = E_0(y, z)cos(\omega t - kz).\hat{e_y} \tag{3.41}$$

Thus, the equation of motion of the electron placed in this field becomes

$$\frac{dv_y}{dt} = -\frac{e}{m_e} E_y(y, z) \tag{3.42}$$

Assuming $\psi = \omega t - kz$, on Taylor expansion of the electric field, it reads as

$$E_y(\mathbf{r}) = E_0(y, z)cos\psi + y\frac{\partial}{\partial y} E_0(y, z)cos\psi \tag{3.43}$$

The solution of equation 3.42 for the lowest order term yields

$$v_y^{(1)} = -vsin\psi \tag{3.44}$$

and

$$y^{(1)} = \frac{v}{\omega} cos\psi \tag{3.45}$$

This can be re-inserted in equation 3.42, giving

$$\frac{\partial v_y^{(2)}}{\partial t} = \frac{e^2}{m_e^2 \omega^2} E_0 \frac{\partial E_0(y)}{\partial y} cos^2\psi \tag{3.46}$$

On multiplying by m_e and averaging over a cycle, the expression for the ponderomotive force can be written as

$$F_p = \left\langle m_e \frac{\partial v_y}{\partial t} \right\rangle = -\frac{e^2}{4m_e\omega^2} \frac{\partial E_0^2}{\partial y} \tag{3.47}$$

On comparing with equation 3.37 the ponderomotive force is given by the negative gradient of the ponderomotive potential,

$$F_p = -\nabla U_p = -\nabla \frac{e^2 E^2}{4m_e\omega^2} \tag{3.48}$$

or,

$$F_p \propto -\nabla I \tag{3.49}$$

Thus, any spatial variation of the laser intensity will act to push the electrons / ions from the region of higher intensity to the region of lower intensity through the ponderomotive force, which is proportional to the gradient of light intensity.

3.6 Relativistic motion of a free electron in an EMW

At higher intensities the magnetic field component in the Lorentz equation becomes strong enough to induce a significant change in the electron dynamics which become nonlinear. In this case the quiver momentum of the electron starts approaching or even exceeding the rest mass momentum of the electron. This regime is known as relativistic regime. For simplicity, at high laser intensity the pulse is characterized by a dimensionless quantity, a_0, known as laser strength parameter. It is defined as

$$a_0 = \frac{v_\perp}{c} = \frac{eE_0}{m_e \omega c} \tag{3.50}$$

where $v_\perp$ is the transverse velocity of the electrons. Sometimes a_0, which is also known as normalized vector potential or normalised momentum, is expressed in terms of the ratio of electrons quiver momentum and rest mass momentum $a_0 = p_0/m_e c$. In practical units, the laser strength parameter is given as

$$a_0 = 8.5 \times 10^{-10} \sqrt{(I\lambda^2)} \tag{3.51}$$

where I is the laser intensity in Wcm^{-2} and λ is the laser wavelength in $\mu\mathrm{m}$. Following the definition of laser strength parameter, relativistic regime comes in when laser quiver momentum becomes close to the electron rest mass momentum, i.e. when $a_0 \simeq 1$.

The amplitude of the electric and magnetic field associated with the laser pulse can be expressed in terms of the laser strength parameter as

$$E_0 = 32.2 \times \frac{a_0}{\lambda} \left(\frac{GV}{cm} \right) \tag{3.52}$$

and

$$B_0 = \frac{E_0}{c} = 107 \times \frac{a_0}{\lambda} \, (MG) \tag{3.53}$$

where λ is in $\mu\mathrm{m}$.

At higher intensities when the electron motion enters relativistic regime it is required to add the relativistic correction in electron mass. The relativistic factor is given as

$$\gamma = \frac{1}{\sqrt{1 - \frac{v^2}{c^2}}} \tag{3.54}$$

The fully relativistic equation of motion of an electron oscillating in a plane electromagnetic wave can be solved exactly [69, 70]. Following [71], let us consider the relativistic Lagrange function of an electron in the electromagnetic wave, propagating along x-direction, with potential A and ϕ

$$L(\mathbf{r}, v, t) = -m_e c^2 \sqrt{1 - \frac{v^2}{c^2}} - e\mathbf{v} \cdot \mathbf{A} + e\phi \tag{3.55}$$

where, r is the position and v is the velocity of the particle. From the Euler-Lagrange equation

$$\frac{d}{dt}\frac{\partial L}{\partial \mathbf{v}} - \frac{\partial L}{\partial \mathbf{r}} = 0 \tag{3.56}$$

one can obtain the equation of motion as

$$\frac{d\mathbf{p}}{dt} = -e\left(\mathbf{E} + \mathbf{v} \times \mathbf{B}\right) \tag{3.57}$$

The canonical momentum can be written as

$$\frac{\partial L}{\partial \mathbf{v}} = m_e \gamma \mathbf{v} - e\mathbf{A} \tag{3.58}$$

where γ is given by equation 3.54.

For a plane light wave, there exist two symmetries which provide two constant of motion. Planar symmetry implies $\partial L/\partial \mathbf{r}_\perp = 0$ and therefore conservation of the canonical momentum in the transverse direction, i.e.,

$$\frac{\partial L}{\partial \mathbf{v}_\perp} = \mathbf{p}_\perp - e\mathbf{A}_\perp = constant \tag{3.59}$$

The second invariant derives from the wave form of $\mathbf{A}(t - x/c)$. Making use of the relation $dH/dt = \partial L/\partial t$ for the Hamiltonian function $H(x, p, t) = E(t)$, which express the time-dependent energy of the particle, one obtains

$$\frac{dE}{dt} = -\frac{\partial L}{\partial t} = c\frac{dp_x}{dt} \tag{3.60}$$

Taking into account that $A_x = 0$ for plane light wave, we have

$$E - cp_x = constant \tag{3.61}$$

and for an electron initially at rest, the kinetic energy is

$$E_{kin} = E - mc^2 = cp_x \tag{3.62}$$

For an electron initially at rest, the constants of motion give

$$\mathbf{a} = \frac{e\mathbf{A}_\perp}{mc^2} \tag{3.63}$$

$$\hat{\mathbf{p}}_\perp = \frac{\mathbf{p}_\perp}{mc} = \mathbf{a} = (0, a_y, a_z) \tag{3.64}$$

$$\hat{E}_{kin} = \frac{E_{kin}}{mc^2} = (\gamma - 1) = \hat{p}_x \tag{3.65}$$

Thus, one can see that

$$\gamma = 1 + \hat{p}_x \tag{3.66}$$

Also,

$$\gamma = \sqrt{1 + \hat{p}_x^2 + \hat{p}_y^2} \tag{3.67}$$

Thus, from equations 3.66 and 3.77, we have

$$\hat{p}_x = \frac{\hat{p}_\perp^2}{2} \tag{3.68}$$

An immediate observation at this point is

$$\hat{p}_x = \frac{a^2}{2} = \gamma\beta_x \tag{3.69}$$

$$\hat{p}_y = a_y = \gamma\beta_y \tag{3.70}$$

$$\hat{p}_z = a_z = \gamma\beta_z \tag{3.71}$$

Since $\gamma = 1 + a^2/2$, we obtain

$$\beta_x = \frac{a^2/2}{1 + a^2/2} \to 1 \tag{3.72}$$

$$\beta_y = \frac{a_y}{1 + a^2/2} \to 0 \tag{3.73}$$

$$\beta_z = \frac{a_z}{1 + a^2/2} \to 0 \tag{3.74}$$

This means that the electron, though oscillating transversely for low field strengths $(a \ll 1)$, moves more and more in the direction of light propagation for relativistic laser intensity $(a \geq 1)$.

As the laser intensity increases and the irradiance reaches around $\sim 10^{18}\mathrm{Wcm}^{-2}\mu\mathrm{m}^2$, the magnetic field associated with the laser pulse become non-negligible and also the electron enters the relativistic regime. The relativistic generalization of the ponderomotive force is done by many authors [72, 73]. It is given by

$$F_p = -\frac{e^2}{4\gamma m_e \omega^2}\nabla E_0^2 \tag{3.75}$$

3.7 Nonlinear optics of the laser propagation in plasmas

In laser plasma interaction studies the stable propagation of the laser pulse is essential for successful realization of many applications. In the absence of any external guiding, the laser beam diffracts in vacuum in one Rayleigh length, $Z_R = \frac{\pi w_0^2}{\lambda}$, where w_0 and λ are the spot size and wavelength of the laser pulse, respectively. For a $5\mu\mathrm{m}$ spot size and $0.8\mu\mathrm{m}$ wavelength, the Rayleigh length tuns out to be $\sim 100\mu\mathrm{m}$, which is small for any significant practical application. In case of two pulse propagation [1], the propagation over 24 Rayleigh lengths was achieved [40]. However, for single pulse experiments, propagation over many Rayleigh lengths without diffraction divergence is a difficult task, at least for low intensity laser pulses. For a Gaussian laser pulse, the ionization of the gaseous medium produces local electron density maximum along the axis of propagation. The refractive index corresponding to such electron density profile acts as a diverging lens and defocusses the laser light strongly, thus worsening the situation. At this point, the non-linearity of laser plasma interaction comes at the rescue. The charge displacement non-linearity caused by the ponderomotive force of the laser pulse and the relativistic mass non-linearity induce self focusing of the laser pulse and its intensity can be maintained over a long distance.

3.7.1 The relativistic mass nonlinearity

While a major source of non-linearity lies in the action of the ponderomotive force, the relativistic mass variation of electrons is another very important source of non-linearity. For long laser pulses (pulse length longer than the plasma wavelength) of moderate intensities, non-linearity caused by the ponderomotive force dominates over the relativistic mass non-linearity. However, the relativistic mass variation of electrons outcasts the ponderomotive

[1] The first pulse was used to form pre-plasma and the second pulse, injected after a suitable time delay, was guided in the pre-plasma channel.

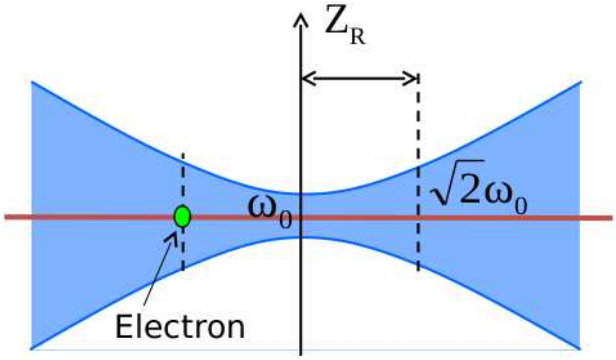

Figure 3.2: Schematic of acceleration of an electron for an unguided laser pulse. In the absence of any guiding medium the effective acceleration length is limited by the laser beam diffraction and is equal to the Rayleigh length. Consequently, the accelerating electrons can only gain few tens of MeV energy in spite of over 100GV/m accelerating gradient.

force non-linearity in high intensity short pulse (pulse length comparable to plasma wavelength) laser plasma interaction. In this case, the dynamics of the electron interaction with the laser field also changes completely. For instance, at low laser intensity the plasma electrons oscillate in the direction of the laser electric field while drift very slowly in the direction of the propagation of the laser. At laser intensity $\geq 10^{18}\mathrm{Wcm}^{-2}$, the scenario is reversed and electrons drift primarily in the direction of the laser propagation due to the $v \times B$ drift and acquire relativistic velocities due to severe oscillation in laser electric field. Once the electrons become relativistic, the origin of non-linearities shifts towards the relativistic mass variation.

3.7.2 The self focusing of the laser pulse

As pointed out above, the ponderomotive force of the laser pulse expels electrons away from the axis of propagation. Consequently, the non-relativistic index of refraction of a plasma

$$\eta = \sqrt{1 - \frac{\omega_p^2}{\omega^2}} \tag{3.76}$$

where $\omega_p^2 = n_0 e^2/m\epsilon_0$, n_0 being the plasma electron density and ω the frequency of the laser pulse, changes exhibiting a local maxima on the axis. This sort of refractive index profile changes the phase velocity of the wavefront and continuously bends the wavefront

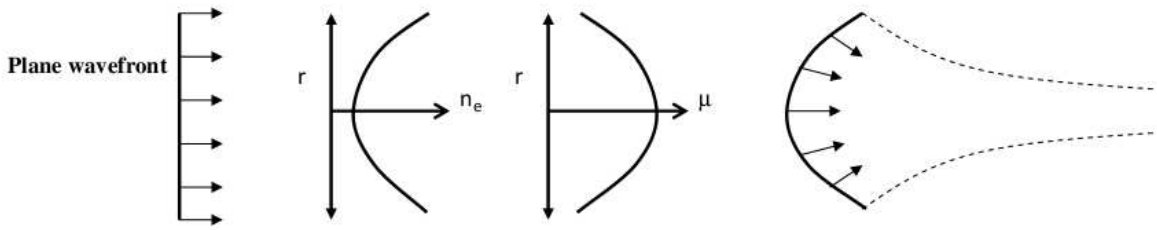

Figure 3.3: Schematic representation of self-focusing of a laser pulse in plasmas. An initially plane wave front is incident on a region of uneven radial density distribution. The electron density is minimum along the axial direction and maximum along the periphery. The refractive index profile is exactly opposite to that of the radial electron density. Consequently, the phase velocity is lower along the axis and higher towards region away from the axis. This result in focusing of the initial plane wave front.

of the laser pulse until the laser pulse is focused to a very small spot (limited by natural diffraction of the pulse).

The pioneering study in the area of self focusing of the laser pulse in a non-linear medium was done by G. A. Askar'yan. The phenomena was predicted theoretically in [74]. This paper also treated thermal and ponderomotive force induced self focusing of the laser pulse. Later on, a paraxial theory was developed for the laser propagation in a medium of cubic non-linearity by Akhmanov et al [75, 76]. The non-linear refractive index and phase of the light wave were expanded in near-axis approximation and curvature of the wavefront was calculated by incorporating the non-linearities simultaneously. This theory became very popular and has been widely used in scientific literature [77, 78]. The first experimental observation on the self-focusing was reported by Hercher [79].

In the relativistic regime of interaction, the refractive index of the plasma takes the form

$$\eta = \sqrt{1 - \frac{\omega_p^2}{\gamma\omega^2}} \tag{3.77}$$

where $\gamma = \sqrt{1 + a^2/2}$, $a = \frac{eE}{m\omega c}$, E is the electric field of the laser pulse. In this case, the uneven variation in γ along the wavefront of the laser pulse causes the same effect as the ponderomotive force does in the previous case. This is called relativistic self focusing (RSF) of the laser pulse. If the laser power exceeds the critical power for relativistic self focusing,

$\mathrm{P_c} = 17(\omega^2/\omega_\mathrm{p}^2)\mathrm{GW}$, then the RSF of the laser pulse occurs [80]. At high laser intensity, the RSF is a dominating mechanism of self focusing of the laser pulse. The theoretical work related to the relativistic non-linearities was first started by C. E. Max and others [81, 82, 83, 84]. The first experimental work on RSF of a laser pulse was reported in 1992 by Borisov et. al. [85]. A copious amount of work related to relativistic laser guiding, harmonic generation and wakefield acceleration have been reported by Sprangle and co-workers [86, 87, 88, 89, 90]. Recently, it was shown that other than P_c, the critical power for RSF, the laser pulse duration is an another very important parameter [91, 92]. The RSF of laser pulses does not occur if the pulse duration is too short compared to ω_p^{-1} even for laser power greater than P_c. For pulses longer than ω_p^{-1}, self focusing can occur even for powers lower than P_c. Associated with the RSF are many recently observed effects e.g. ion channel formation, monoenergetic electrons observation, x-ray radiation generation.

CHAPTER 4

Laser driven wakefield acceleration of electrons

4.1 Outline

The laser driven wakefield acceleration of electrons is one of the most important application of the laser plasma interaction. This scheme relies on the conversion of the transverse laser electric field into the longitudinal plasma wave electric field. A laser pulse propagating through an underdense plasma excites a running plasma wave behind it through the action of its ponderomotive force. This plasma wave is different from the conventional Langmuir wave in a sense that it trails the laser pulse with a very high phase velocity (equal to the group velocity of the laser pulse, which is close to c). These high phase velocity plasma waves can trap and accelerate plasma electrons to very high energies. Laser based plasma accelerators has demonstrated generation of multi MeV high quality electron bunches in several experiments. In this chapter, we will discuss the basic physics of this rapidly developing field, concentrating on the generation of the electron plasma wave and its role in particle acceleration.

4.2 Physical mechanism of laser based plasma accelerators

Although electric fields of the order of 1TV/m are readily achievable these days at the focus of a laser beam, these fields in vacuum cannot be used directly for particle acceleration. This is because they are transverse and oscillatory in nature. However, if laser light can be used to excite Langmuir waves in a plasma, these waves being longitudinal, can be used to accelerate charged particles.

As discussed in the previous chapter, to understand the excitation of Langmuir or electron plasma waves in plasmas using lasers, one needs to understand the concept of ponderomotive force. Free electrons, such as the ones present in plasma, can quiver in the electric field associated with the electromagnetic wave. The motion of the electron in the presence of electric field is governed by the Lorentz force. In the case of high, non-uniform electromagnetic (or purely electric) field, the expression for the Lorentz force has a second order term known as the ponderomotive force, which is proportional to the gradient of square of electric field [1].

$$\mathrm{F_p} \propto -\nabla \mathrm{E}^2 \tag{4.1}$$

or in terms of laser intensity

$$\mathrm{F_p} \propto -\nabla \mathrm{I} \tag{4.2}$$

where, E is the electric field and I is intensity of the laser pulse. Thus, one can notice from the above equation that any spatial variation in the laser intensity profile will act to push the electrons / ions from the region of higher intensity to the region of lower intensity through the ponderomotive force, which is proportional to the gradient of the light intensity. This is illustrated in Figure 4.1.

This displacement of electrons creates large amplitude plasma waves whose field could reach up to 100 GV/m, provided there is a resonance between the plasma frequency and the ponderomotive force. The electrons trapped in such a high electric field can be accelerated to high energies in the several hundred MeV range.

Two methods have been proposed to use the ponderomotive force exerted by intense laser pulse to excite plasma waves resonantly. These are:

1. Laser beat wave acceleration (**LBWA**).

2. Laser wakefield acceleration (**LWFA**).

[1] Refer equation 3.49

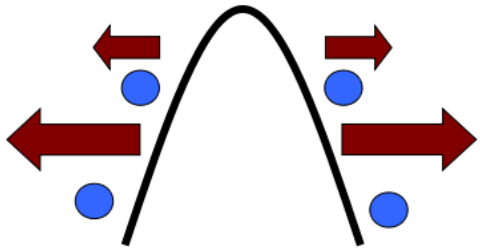

Figure 4.1: Figure shows the action of the ponderomotive force for a pulse with Gaussian intensity distribution. The blue circles corresponds to electrons / ions. The ponderomotive force pushes these particle away and excites a disturbance in plasma which result in excitation of plasma waves.

In 1992, a third mechanism called the self-modulated laser wakefield acceleration (**SM-LWFA**) has been proposed. We will discuss all these acceleration mechanisms in detail in the subsequent sections.

4.3 Laser beat wave acceleration

In the LBWA method, the plasma wave is excited by beating two optical waves of slightly different frequencies. Two laser waves of frequency ω_1 and ω_2, having polarization in the same direction, travelling in a preformed plasma of uniform density, n, corresponding to a plasma frequency ω_p, will beat at a frequency $\Delta\omega = \omega_1 - \omega_2$. If this frequency difference is exactly equal to the plasma frequency $(i.e. \Delta\omega = \omega_p)$, then strong Langmuir waves will be excited in the plasma by the longitudinal ponderomotive force of the beat wave. Since the beat wave moves with the laser pulse, the plasma wave will also move with a phase velocity equal to the group velocity (near light velocity) of the laser pulse. A properly placed bunch of electrons with a velocity slightly lesser than the laser group velocity will get accelerated by wave-to-particle energy transfer (explained latter). However, as the amplitude of oscillation becomes very large, the mass of the electrons becomes relativistic and the wave cannot be excited any more as it is no more in resonance $\left(\omega_p \propto \sqrt{\frac{1}{m_e}}\right)$.

Problems with this method are:

1. Necessity of preformed plasma of uniform density,

2. Strict requirement of plasma density to exactly match with the beat wave frequency, and

3. Clamping of field due to relativistic effects.

All these problems are absent for the laser wakefield acceleration method.

4.4 Laser wakefield acceleration

To understand the concept of laser wakefield acceleration, it is necessary to understand what a wake-field is. When a speed-boat travels in water, it produces two types of waves viz. bow waves and wake-field waves. The bow waves are conical waves having tip at the front of the boat. These are produced because the velocity of the boat exceeds that of the water waves. These waves are of similar character as that of the sonic boom produced when a supersonic jet flies in air. The wake-field waves are set up at the back (or wake) of the boat. These waves travel with the phase velocity equal to the velocity of the boat. By the principle of the Landau damping, a floating ball dropped in the wake-field wave of the boat will get accelerated to the velocity of the boat if its initial velocity is slightly less than that of the boat. This is exactly the principle of the laser wakefield acceleration mechanism.

For LWFA, one uses a short pulse of very high intensity. When such a high intensity laser pulse is incident on a gas target, its leading edge ionizes the gas. The laser light propagates in this plasma with a velocity equal to the group velocity $\left(v_g \approx c\left[1-\frac{\omega_p^2}{2\gamma\omega^2}\right]\right)$ in plasma, which is nearly equal to the velocity of the light. The short laser pulse has a strong intensity variation in time and correspondingly in space. This leads to a strong longitudinal ponderomotive force. The spatial extent of this ponderomotive force, and that of the density perturbation caused by it, is of the order of $2c\tau$, where τ is the pulse duration of the laser pulse. If this is made equal to the plasma wavelength $(\lambda_p = 2c\pi/\omega_p)$, then high amplitude wake-fields are produced due to resonance (see Fig. 4.2). As in the case of the boat, the laser wake-field moves with the pulse at a phase velocity equal to the group velocity of the laser pulse. Therefore, a correctly placed trailing bunch of relativistic electrons can be accelerated by the longitudinal field of the plasma waves.

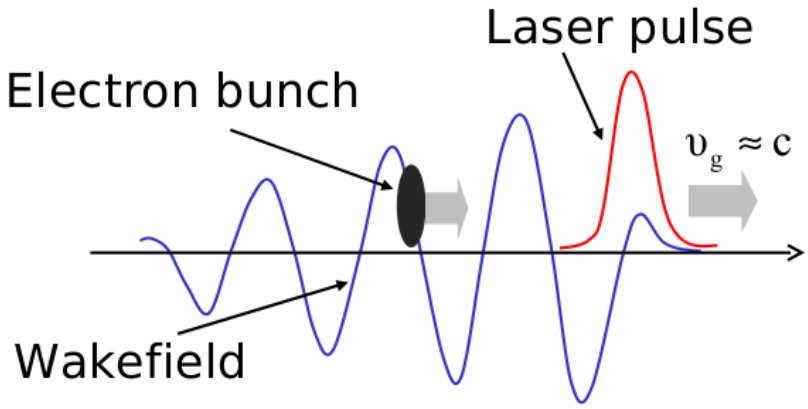

Figure 4.2: Schematic of laser wakefield acceleration mechanism. The laser pulse moving at nearly speed of light excites a plasma wave trailing behind it. A relativistic electron bunch placed in right phase experiences large accelerating field and gains energy.

4.5 Self-modulated laser wakefield acceleration

In this scheme, the electron plasma wave is excited resonantly by the modulation of the laser pulse envelope. This occurs for a laser pulse having spatial extent or length $(c\tau)$ few times longer than the plasma period (λ_p) and the pulse power larger than the power required for self-focusing of the laser beam (critical power). Owing to the finite pulse shape, a small plasma wave is excited non-resonantly, which results in growth of forward Raman scattering (FRS) instability. The FRS wave and the laser wave beat at the plasma frequency giving rise to enhancement of the electron plasma wave. Thus, there exist an oscillating density perturbation within the pulse envelope. The laser pulse therefore sees a refractive index, which is alternately peaked and dented at interval of $\lambda_p/2$, where λ_p is the wavelength of the plasma wave. As the phase velocity of the laser wave is dependent of the density, the modulation in density gives rise to redistribution of the photon flux within the laser pulse, leading to modulations in the envelope with a period λ_p. This modulation gives rise to a strong ponderomotive force with wavelength exactly equal to the plasma wavelength (as in LWFA), which strongly enhances the plasma wave amplitude. This effect grows in time thereby transforming the initial laser pulse envelope into a train of shorter pulses with width of λ_p or duration proportional to ω_p^{-1}. Since $\lambda_p \sim n^{-1/2}$ and $P_c \sim n^{-1}$, then for fixed laser

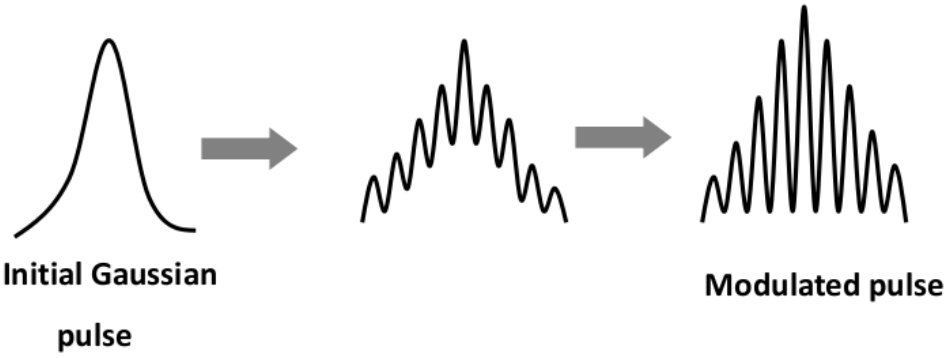

Figure 4.3: Self-modulated laser wakefield mechanism. The initial laser pulse undergoes density modulation instability and breaks up into a train of shorter pulse with width λ_p.

parameters, the conditions $L > \lambda_p$ and $P > P_c$ can usually be satisfied by operating at sufficiently high plasma density. Where L is the spatial extent of the laser pulse and P_c is the critical power for self-focusing. Figure 4.3 shows the self-modulated scheme of laser wakefield acceleration.

The advantages of the self-modulated LWFA over the standard LWFA are simplicity and enhanced acceleration. Simplicity in that a matching condition of $L \sim \lambda_p$, a preformed density channel and pulse tailoring are not required. Enhanced acceleration is achieved for several reasons:

1. The SM-LWFA operates at a higher density, hence a larger wake-field will be generated, since $E \sim \sqrt{n}$,

2. The wakefield is resonantly excited by a series of pulses as opposed to a single pulse as in the standard LWFA, and

3. Relativistic optical guiding allows the modulated pulse structure to propagate for several Rayleigh length, thus extending the acceleration distance.

So far, we have seen that when a short laser pulse propagates through an underdense plasma, a large amplitude plasma wave is excited in the wake of the laser pulse by the ponderomotive force associated with the temporal profile of the pulse. In addition, for loosely focused pulses (i.e. when $k_p \times w_0 \gg 1$), where k_p and w_0 are the plasma wave-vector and the

beam size at the waist respectively, only a longitudinal electron plasma wave is generated. Whereas, in tightly focused geometry (i.e. when $k_p \times w_0 \leq 1$), both components of the ponderomotive force, longitudinal and radial, generates a density perturbation. The amplitude of the wave is maximum when $\omega_p \times \tau \sim 1$, where τ is the pulse duration and ω_p is the plasma frequency.

4.6 Plasma wave excitation

After gaining the insight of the physical mechanism of plasma wave excitation and particle acceleration we will now discuss the mathematical derivation of the plasma wave excitation. Let us consider the propagation of a short laser pulse in a preformed underdense plasma of electron density n_0,

$$\mathbf{E_0} = \hat{x} A_0 e^{-(i\omega t - k_0 z)} \tag{4.3}$$

$$A_0^2 = A_{00}^2 e^{-(t-z/v_g)^2/\tau^2} e^{-r^2/r_0^2} \tag{4.4}$$

Where $k_0 = (\omega_0/c)(1 - \omega_p^2/\omega_0^2)^{1/2}$, $v_g = c(1 - \omega_p^2/\omega_0^2)$, ω_0 is laser frequency and ω_p is the electron plasma frequency. The laser electric field gives an oscillatory velocity to the plasma electrons, which reads as

$$v_0 = \frac{eE_0}{m\gamma_0\omega_0} \tag{4.5}$$

where $\gamma_0 = (1 + a_0^2/2)^{1/2}$ is the relativistic factor, $a_0 = e|E_0|/m\omega_0 c$ is the laser strength parameter, and e and m are the electronic charge and rest mass, respectively. Apart from giving an oscillatory motion of the plasma electrons, the laser pulse also exerts a ponderomotive force (as explained in the previous chapter) $F_p = e\nabla\phi_p$ on them, where

$$\phi_p = -(mc^2/e)[(1 + a_0^2)^{1/2} - 1] \tag{4.6}$$

This is known as ponderomotive potential. The ponderomotive potential depends on the laser pulse strength. The ponderomotive force drives a plasma wave of potential ϕ. In the limit when the density perturbation due to the plasma wave $n \ll n_0$, one may write the equations of motion and continuity in the linearization approximation as

$$\frac{\partial \mathbf{v}}{\partial t} = \frac{e}{m}\nabla(\phi + \phi_p) \tag{4.7}$$

$$\frac{\partial n}{\partial t} + n_0 \nabla \cdot \mathbf{v} = 0 \tag{4.8}$$

where v and n are the velocity and density perturbations, respectively. On differentiating Eq. (4.6) with respect to time, and employing Eq. (4.5) and the Poisson's equation, $\nabla^2\phi = 4\pi en$, one can obtain

$$\frac{\partial^2\phi}{\partial t^2} + \omega_p^2\phi = -\omega_p^2\phi_p \tag{4.9}$$

Introducing a new set of variables $\xi = t - z/v_g$ and $\eta = z$, Eq. (4.7) takes the form

$$\frac{\partial^2\phi}{\partial \xi^2} + \omega_p^2\phi = \frac{-\omega_p^2 eA_{00}^2}{2m\omega_0^2} e^{-\xi^2/\tau^2} e^{-r^2/r_0^2} \tag{4.10}$$

giving

$$\phi = \frac{\omega_p^2 eA_{00}^2 e^{-r^2/r_0^2}}{4i\omega_p m\omega_2^0} \left[e^{-i\omega_p\xi} \int_{-\infty}^{\infty} e^{i\omega_p\xi} e^{-\xi^2/\tau^2} d\xi - e^{i\omega_p\xi} \int_{-\infty}^{\infty} e^{-i\omega_p\xi} e^{-\xi^2/\tau^2} d\xi \right] \tag{4.11}$$

In the wake of the laser pulse, as $\xi \to \infty$ the plasma wave potential attains the value

$$\phi = \frac{\omega_p eA_{00}^2 e^{r^2/r_0^2}}{2m\omega_0^2} \tau\sqrt{\pi} e^{-\omega_p^2\tau^2/4} sin(\omega_p t - k_p z), \tag{4.12}$$

where $k_p = \omega_p/v_g \simeq \omega_p/c$. The amplitude of the plasma wave maximizes for $\tau = \sqrt{2}\omega_p^{-1}$;

$$|\phi|_{max} = \frac{eA_{00}^2\sqrt{\pi}}{2.3m\omega_0^2} e^{-r^2/r_0^2} \tag{4.13}$$

which is of the same order as the peak pulse of the ponderomotive potential. One can notice the dependence of the potential on laser vector potential. Thus, one can see that the laser pulse can excite an electron plasma wave at its wake whose potential and the corresponding electric field are comparable to that of the wave itself. The transverse electric field of the laser pulse is used to generated a plasma wave with a longitudinal electric field, which can potentially accelerate charged particles.

4.7 Electron beam generation: wave-breaking and maximum accelerating field

So far we have seen that the interaction of a high intensity laser pulse with an underdense plasma can efficiently create electron plasma waves. In principle, an electron beam provided by an external source can be injected into an electron plasma wave that can be further accelerated by these waves. This was the approach followed worldwide initially. However, in the self-modulated laser wakefield regime, the plasma waves are excited to such an extent that

they break and some electrons get separated from the main wave and get accelerated. This is called self-trapping of electrons by wave-breaking.

In the Sm-LWFA regime, once the amplitude of the plasma wave has exceeded a limiting value, wave-breaking takes place. This wave-breaking occurs when the amplitude of the electron oscillation becomes longer than the plasma wavelength. Some of the plasma electrons undergo such large oscillations that the returning force is no longer large enough to make them continue their longitudinal oscillations. Instead, the electrons can continue into the next wave bucket and in place of returning force they feel a continued acceleration, resulting in their trapping with the plasma wave. The trapped electrons continue to be accelerated until their velocity exceeds that of the plasma wave and it out-runs the wave and get dephased.

Following [71], let us derive a simple formula for wave-breaking and maximum electric field an electron plasma wave can sustain in a one dimension case. The relativistic one-dimensional equation for fluid velocity can be written as

$$\frac{\partial E}{\partial x} = 4\pi e(n_0 - n) \tag{4.14}$$

$$\frac{\partial n}{\partial t} + \frac{\partial}{\partial x} nu = 0 \tag{4.15}$$

$$\left(\frac{\partial}{\partial t} + u\frac{\partial}{\partial x}\right)(\gamma m u) = -eE \tag{4.16}$$

We look for solutions for $n(x,t), u(x,t)$ and $E(x,t)$ that depend on $\tau = \omega_p(t - \frac{x}{v_p})$ Since, $d/dt = \partial/\partial t + u\partial/\partial x$, one can write

$$\frac{d}{dt} = \frac{\partial}{\partial t} + u\frac{\partial}{\partial x} \tag{4.17}$$

$$= \frac{\partial \tau}{\partial t}\frac{\partial}{\partial \tau} + u\frac{\partial \tau}{\partial x}\frac{\partial}{\partial \tau} \tag{4.18}$$

$$= \omega_p \frac{\partial}{\partial \tau} - \omega_p \frac{u}{v_p}\frac{\partial}{\partial \tau} \tag{4.19}$$

This implies that

$$\frac{\partial}{\partial t} = \omega_p \frac{\partial}{\partial \tau} \tag{4.20}$$

$$\frac{\partial}{\partial x} = -\frac{\omega_p}{v_p}\frac{\partial}{\partial \tau} \tag{4.21}$$

Therefore, one can now write equation 4.15 as

$$\omega_p \frac{\partial n}{\partial \tau} - \frac{\omega_p}{v_p}\frac{\partial}{\partial \tau}(nu) = 0 \tag{4.22}$$

$$or, \qquad \frac{\partial n}{\partial \tau} - \frac{1}{v_p}\frac{\partial}{\partial \tau}(nu) = 0 \tag{4.23}$$

$$\Rightarrow \qquad n - \frac{1}{v_p} nu = n_0 \tag{4.24}$$

or,

$$n = \frac{n_0}{1 - \frac{\beta}{\beta_p}} \tag{4.25}$$

where, n_0 is the initial unperturbed density, $\beta = u/c$ and $\beta_p = v_p/c$. Thus, the above equation implies that the density becomes very large in a region where the fluid velocity approaches the phase velocity. When fluid velocity becomes equal to the phase velocity there exist a singularity and the density goes to infinity. This is the point where the wave no longer can grow and breaks down. This condition is called **wave-breaking**.

Further, one can write equation 4.16 as

$$\left(\omega_p \frac{\partial}{\partial \tau} - u\frac{\omega_p}{v_p}\frac{\partial}{\partial \tau}\right)(\gamma m u) = -eE \tag{4.26}$$

$$or, \qquad \omega_p m \left(\frac{\partial(\gamma u)}{\partial \tau} - \frac{1}{v_p} u \frac{\partial}{\partial \tau}(\gamma u)\right) = -eE \tag{4.27}$$

on further simplification, one can arrive at

$$\frac{1}{\left(1 - \frac{\beta}{\beta_p}\right)}\frac{\partial}{\partial \tau}(\gamma\beta) = -\hat{E} \tag{4.28}$$

where, $\hat{E} = \frac{eE}{m\omega_p c}$.

Now equation 4.14 can be written as

$$-\frac{\omega_p}{v_p}\frac{\partial}{\partial \tau}E = -4\pi e(n_0 - n) \tag{4.29}$$

$$or, \qquad \frac{\partial E}{\partial \tau} = \frac{4\pi}{\omega_p} v_p e(n_0 - n) \tag{4.30}$$

The above equation can be cast in a more compact way as follows,

$$\frac{\partial E}{\partial \tau} = \left(\frac{4\pi n_0 e^2}{m}\right)\left(\frac{v_p}{\omega_p}\right)\left(1 - \frac{n}{n_0}\right)\frac{m}{e} \tag{4.31}$$

$$= \frac{\omega_p m c}{e}\left(\frac{v_p}{c}\right)\left(1 - \frac{n}{n_0}\right) \tag{4.32}$$

From equation 4.32 and the definition of $\hat{E}$, one can arrive at

$$\frac{\partial \hat{E}}{\partial \tau} = \frac{\beta}{1 - \frac{\beta}{\beta_p}} \tag{4.33}$$

Now from equation 4.28 and 4.33, we have

$$\hat{E}\frac{\partial \hat{E}}{\partial \tau} = -\beta \frac{\partial(\gamma\beta)}{\partial \tau} \tag{4.34}$$

Since $\beta = u/c$ and $\gamma = 1/\sqrt{1-\beta^2}$, we can write

$$\frac{1}{2}\frac{\partial}{\partial \tau}(\hat{E}) = -\frac{\partial \gamma}{\partial \tau} \tag{4.35}$$

or,

$$\frac{\partial}{\partial \tau}\left(\frac{\hat{E}}{2} + \gamma\right) = 0 \tag{4.36}$$

$$or, \qquad \hat{E} = \sqrt{2\left(\gamma_m - \gamma\right)} \tag{4.37}$$

where γ_m is a constant and is equal to γ_p, the factor at which wave breaking takes place. On substituting the value of $\hat{E}$, we have

$$E = \frac{m\omega_p c}{e}\sqrt{2\left(\gamma_p - \gamma\right)} \tag{4.38}$$

When $E = E_{max}, \gamma = 1$ as $v \to 0$.

Thus, finally we have

$$E_{max} = \frac{m\omega_p c}{e}\sqrt{2\left(\gamma_p - 1\right)} \tag{4.39}$$

The above equation gives the maximum value of the electric field the wave can sustain before wave breaking.

4.8 Dephasing length and maximum energy gain

As discussed in earlier sections, an electron can gain energy as long as it is in phase with the plasma wave. Once the electron runs-out of phase it starts decelerating and loosing energy. The time during which the phase slippage takes place between electron and Langmuir wave is given by

$$\frac{T}{2} = \frac{L}{v_g} - \frac{L}{c} \tag{4.40}$$

where T is the period of the plasma wave, L is the acceleration distance, v_g is the group velocity of the laser pulse and c is the speed of light.

Using

$$v_g = c\left(1 - \frac{\omega_p^2}{\omega_2}\right) \qquad \text{and} \qquad T = \frac{2\pi}{\omega_p} \tag{4.41}$$

and solving the above equation, we have

$$L_{max} = \frac{2c\pi\omega^2}{\omega_p^3} \tag{4.42}$$

This gives the maximum acceleration length and is also known as the **dephasing length**.

Thus, the maximum energy gain by the electron is given as

$$\triangle w = eE_{max}L_{max} \tag{4.43}$$

4.9 Blow off acceleration regime

At high laser intensity, PIC simulations reveal the formation of an electron evacuated ion bubble at the rear of the laser pulse and generation of mono-energetic electrons. The electrons are seen to pile up at the bubble boundary and surge towards the stagnation point. It is a three dimensional phenomena where axial and radial ponderomotive force and the space charge field play key roles. However, significant insight can be gained by one dimensional model also.

4.9.1 Electron acceleration by the ion bubble

A nonlinear theory of relativistic plasma wake field in the blow off regime has been proposed by Lu et. al. [93]. In a frame moving with the laser pulse, the ion bubble is stationary. The plasma electrons far ahead of the laser pulse approach the laser with large axial velocity $-\hat{z}v_g$. As they are retarded by the axial ponderomotive force and pushed radially away by the radial ponderomotive force, their density increases at the bubble boundary and they surge towards the stagnation point from all transverse direction. Initially, the surging electrons cross the stagnation point with finite velocity (with respect to the moving frame). However, as the pile size grows, the velocity of surging electrons decreases. When the pile acquires a critical size, wave breaking injects electrons in pile into the ion bubble and the subsequent acceleration by plasma wave and the ion space charge field, produces mono-energetic electrons.

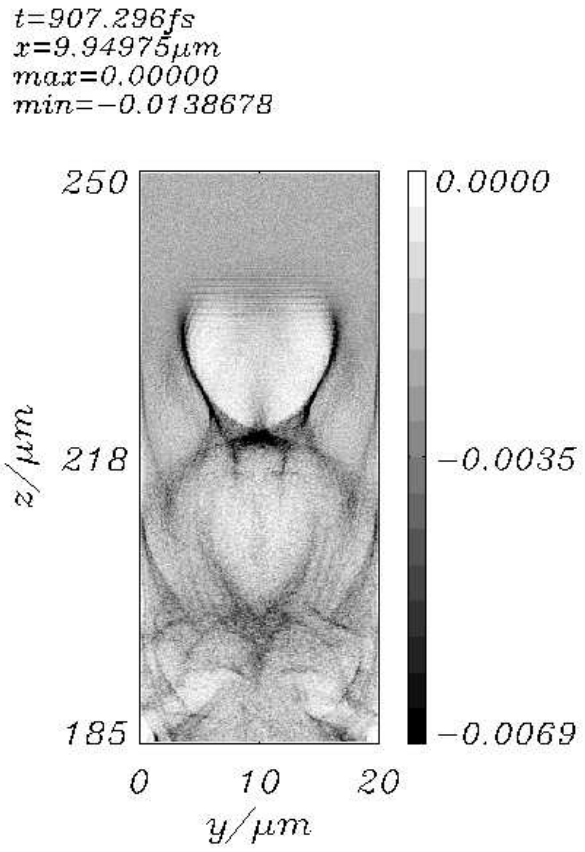

Figure 4.4: An example of the Particle-in-cell simulation showing the formation of an "ion-bubble". A laser pulse of energy 5 J, 30 fs is focused to a spot size of diameter 18 μm in a pre-formed plasma. After propagating nearly $250\mu m$ a region void of electrons is clearly visible in the figure. The side bar represent the electron density normalised by critical density. The result is obtained with PSC code.

An estimate of the ion bubble radius R can be obtained by equating the ponderomotive force to the space charge force at the bubble boundary (in the region where ion bubble and laser pulse overlap), one obtains

$$\frac{mc^2}{e}\left[\left(1+\frac{a^2}{2}\right)^{1/2}-1\right]=\frac{4\pi}{3}n_i e R^2 \tag{4.44}$$

giving

$$R=\sqrt{3}\left(\frac{c}{\omega_p}\right)\left[\left(1+\frac{a^2}{2}\right)^{1/2}-1\right] \tag{4.45}$$

At large intensities $a \gg 1$, R scales as $a^{1/2}$. For $a \simeq 6, R \simeq 3.3c/\omega_p$.

The critical size r_c of the electron pile at the stagnation point is the one for which the potential energy of electrons at the pile surface equals their initial kinetic energy (at the bubble boundary just after emerging from the laser pulse). Thus,

$$\frac{4\pi}{3} r_c^2 n_0 e^2 = mc^2(\gamma_{in} - 1), \tag{4.46}$$

or,

$$r_c \approx \left(\frac{c}{\omega_p}\right)\left(\frac{n_0}{n_c}\right)^{1/2} \tag{4.47}$$

where γ_{in} is the initial Lorentz factor.

The electrons reaching the stagnation point with zero speed are pulled axially by the bubble space charge. The electric field at distance z' from the center of the ion bubble is

$$\varepsilon' = \int_0^R eE_z dz' = \gamma_g \frac{mc^2}{6}\left(\frac{R\omega_p}{c}\right)^2 \tag{4.48}$$

where $\gamma_g = \left(1 - v_g^2/c^2\right)^{-1/2}$. In the laboratory frame the electron energy turns out to be

$$\varepsilon = \gamma mc^2 \tag{4.49}$$

where

$$\gamma = \gamma_g \left[1 + \frac{\gamma_g}{6}\left(\frac{R\omega_p}{c}\right)^2 + \frac{\gamma_g}{c}\sqrt{\left\{1 + \frac{\gamma_g}{6}\left(\frac{R\omega_p}{c}\right)^2\right\}^2 - 1}\right] \tag{4.50}$$

The acceleration energy is sensitive to the bubble radius. If one employs $R = 3.3c/\omega_p$ as estimated above for $a \approx 6$ and $\omega_p/\omega = 0.1$, one obtains $\varepsilon \simeq 180MeV$.

Part III

Ionization of gases with intense laser pulses

CHAPTER 5

Numerical modelling on ionization

5.1 Outline

This thesis is concerned to laser pulse propagation in underdense plasmas and its fundamental studies. The work in this direction was started with a numerical study of the ionization process. The process of ionization and plasma evolution is of significant importance not only from a theoretical but also from an experimental point of view. Laser pulses of intensities $\geq 10^{18} W cm^{-2}$ are now routinely available in laboratories. Such intensities can be achieved by spatially focusing high energy and temporally short light pulses. Consequently, the interaction of intense laser pulses with the target invariably experiences significant spatial and temporal variations in the laser intensity. Different intensity intervals occupy different volumes within the laser-target interaction zone, with lower intensity occupying much larger volume compared to the spatial region over which the peak intensity acts. Thus, ionization is a kind of integrated effect of local intensity and volume.

The response of individual atoms to intense short laser pulses is described in section 5.2. In Section 5.3 critical ionizing field and ionization probability is discussed. In section 5.4 the ionization model used in this thesis to determine the electron density distribution is described. Finally, in section 5.5 the pre-pulse effect on the ionization process in our experimental condition is discussed.

5.2 Atomic processes in intense laser fields

The interaction of electromagnetic waves with matter is one of the most attractive field of research. Before the invention of lasers, the intensity of the available light sources was weak enough so that the atomic binding potential almost remained undisturbed by the externally applied field and the perturbation theory was sufficient to describe its interaction with matter. Based on this theory, conventional spectroscopy has long been used to study the material structure because weak fields will drive the transitions between atomic/molecular states without much distortion of the material itself. The well known photoelectric effect is observed only if the photon energy is above the ionization threshold, and the effect is independent of light intensity. However, after the invention of lasers it was possible to achieve higher intensity. Non-linear optical effects were discovered so that electrons can absorb more than one photon during the transition. New phenomena such as second harmonic generation emerged and found very important applications. An important milestone in atomic physics was reached with the development of solid state lasers delivering very short pulses and the application of the chirped-pulse amplification technique to these short pulses. When these short and intense laser pulses interact with matter many new phenomena appeared. It become possible to ionize the matter, even with photon energy much smaller than the ionization energy, by absorption of a large number of photons. Another example is higher harmonic generation, the emission of photons observed at frequencies that are multiple of laser frequencies. As the pulse length gets shorter, the motion of the electrons is not due to the accumulation of many cycles of the electric field but is controlled by few cycle of oscillations. At these high external fields an important question arises: *How the potential well looks like to an electron under the action of an intense laser field* ? Figure 5.1 illustrates the physical appearance of the atomic potential depending on the strength of the applied field. To understand well the interaction of an atom with an externally applied field, one needs to know the atomic properties and how the atom responds to these applied fields.

The atom has a structure with well defined characteristic properties. These properties can serve as a baseline to understand what happens when an atom comes under the influence of an electromagnetic wave with a given field amplitude. The size of an atom is of the order of the Bohr radius (a_0) and the classical orbiting angular frequency of the electron can be defined as $\omega_{at} = \frac{I_p}{\hbar}$, where I_p is the ionization potential. The atomic electric field can read as $E_{at} = \frac{e}{4\pi\epsilon_0}\frac{1}{a^2}$, with the corresponding field intensity $I_{at} = \frac{1}{2}c\epsilon_0 E_{at}^2$. For the hydrogen

atom the electron will go around the core 3×10^{15} times in one second. E_{at} is equal to $5.4 \times 10^{9} V/cm$ and I_{at} is $3.5 \times 10^{16} W cm^{-2}$. For the present days solid-state laser pulses in the infra-red region the wavelength is about 800 nm. The pulse length can be so short that it only contains a few cycles of the electric field oscillations. The intensity of the laser pulse can be so high that at the peak of the laser pulse, the electric field strength is comparable to the atomic electric field strength. A thumb-rule in this context is

$$E(V cm^{-1}) \sim 27.4\sqrt{I(W cm^{-2})} \tag{5.1}$$

where E is the electric field of the laser and I is the corresponding intensity. At an intensity of $10^{15} W cm^{-2}$, the electric field is comparable to the atomic field and the electron will be easily set free and then driven by the electric field. In fact, it is just not the intensity or peak electric field which drives the mechanism of ionization but the pulse frequency and duration are also very important parameters. The dynamics of the electron could be very complicated and it is important to understand how the atom get ionized.

Conventionally, ionization can be classified into two regimes: tunnelling and multi-photon ionization [94]. If the photon energy is much smaller than the ionization potential and the peak electric field strength of the laser approaches the atomic electric field strength then the electron will have significant probability of tunnelling through the potential barrier. Keldysh defined a parameter [95] to characterize this region as the ratio of laser frequency ω_L to the tunnelling frequency ω_t:

$$\gamma = \frac{\omega_L}{\omega_t} = \omega_L \frac{\sqrt{2I_p}}{E_0} \tag{5.2}$$

where $\omega_t = \frac{E_0}{\sqrt{2I_p}}$, I_p is the ionization potential and E_0 is the maximum electric field of the laser; ω_t^{-1} is the tunneling time, i.e., the time the electron spends under the barrier. We see from above formula that the requirement that the Keldysh parameter be small is fulfilled when the intensity is high and the frequency is low, precisely the parameter range of present day laser systems. The Keldysh parameter, γ, can also be defined as

$$\gamma = \sqrt{\frac{I_p}{2U_p}} \tag{5.3}$$

where $U_p = \frac{e^2 E_0^2}{4 m_e \omega_L^2}$ is the ponderomotive potential as described in previous chapters. When γ is significantly less than unity then the ionization is mainly due to tunnelling. This tunnelling ionization is based on a static point of view of the system. In this case the energy of the

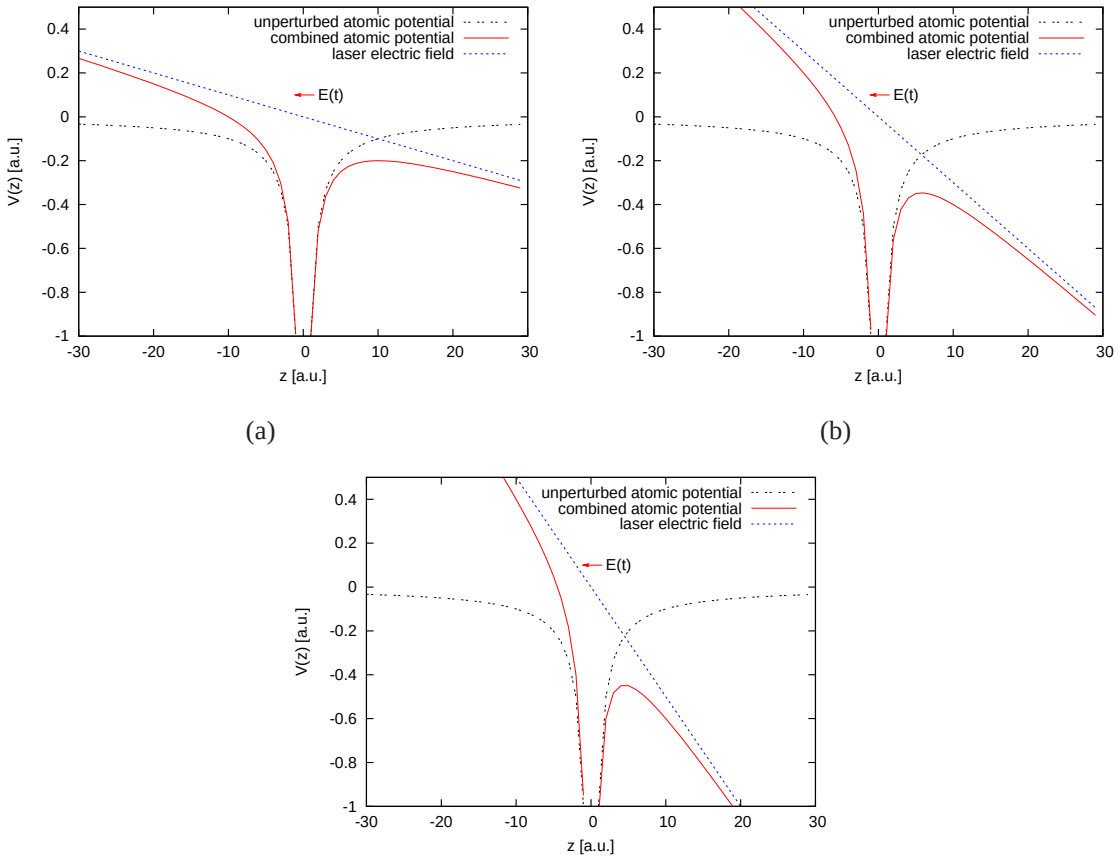

Figure 5.1: Schematic representation of the atomic potential in different intensity regimes. Fig.(a) shows the multi-photon ionization corresponding to an intensity regime of $10^{13} - 10^{14} Wcm^{-2}$, fig.(b) shows tunneling ionization corresponding to an intensity regime of $10^{14} - 10^{17} Wcm^{-2}$ and fig.(c) shows over-the-barrier ionization corresponding to an intensity regime of $\geq 10^{17} Wcm^{-2}$.

electron does not change significantly from the ground state energy but the energy level is broadened, so that the electron has a finite probability to tunnel through the potential barrier set up by the Coulomb potential and the electric field of the laser. One can better understand this point in simple words that the requirement for the validity of the tunneling model for an oscillating field is that the width of the barrier does not change during the time the electron spends traversing it, i.e., the electron adiabatically follows the changes in the external field. After tunnelling the electron will appear in the continuum with zero kinetic energy and thereafter oscillates in the electric field of the laser. When Keldysh parameter is greater than one and the laser frequency is comparable to the electron orbiting frequency the ionization is due to multi-photon absorption. Since the light frequency is now comparable

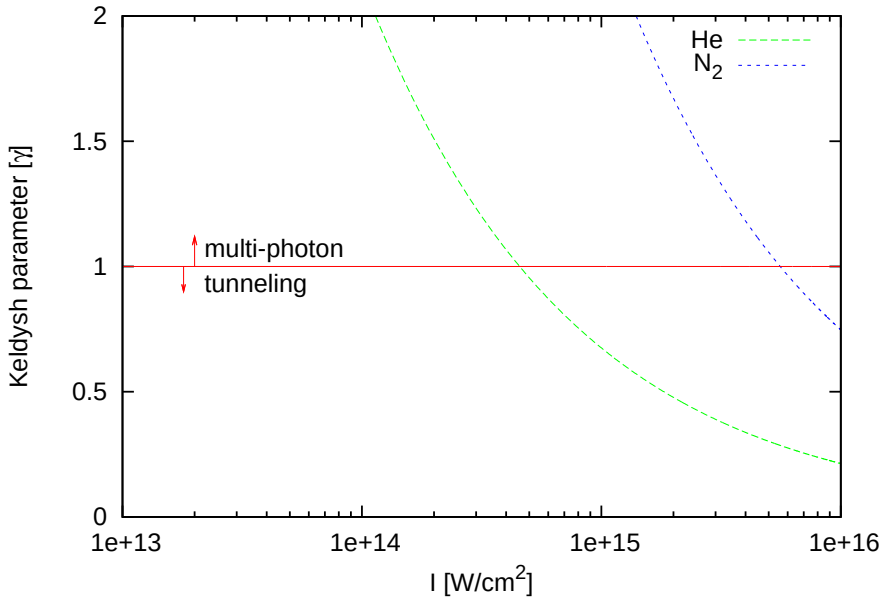

Figure 5.2: Keldysh parameter as a function of the laser intensity for He and N_2 atoms. Depending on the atomic species and intensity, either multi-photon or tunneling ionization occurs.

to the electrons orbiting frequency, as soon as the electron tries to escape from the distorted atomic potential the polarity of the oscillating field gets changed and once again the potential raises at that side. But the high photon flux density makes multi-photon ionization possible.

In multi-photon ionization, the ionization process is induced if many photons are absorbed simultaneously. This ionization process indeed is based on the existence of short living virtual electronic states having life time of the order given by time-energy uncertainty principle, $\Delta E \cdot \Delta t \geq \hbar$, where $\Delta E = \hbar\omega$ is the energy spacing between the two virtual levels and Δt is the life time of these levels. An electron which is excited to such a virtual state by absorbing a photon, has to absorb the next photon within a time of the order of the life-time of the virtual states. That is why the radiation field must be associated with a large photon density to ensure a non-zero probability of multi-photon ionization.

At very high intensities, ionization has been further classified and it is said that at intensities higher than the tunnel ionization intensity threshold, over the barrier ionization mechanism dominates [96, 97]. In such high fields, the barrier can be suppressed so drastically that the electron no longer finds any potential to overcome and escapes from the atomic field. This is shown in Fig.5.1(c). This process is called over-the-barrier ionization. It is important to note that this process can take place only if the laser pulse is short enough,

otherwise the atom will get ionized by multiphoton or tunnelling process on the rising edge of the laser pulse before the field becomes strong enough for over-the-barrier ionization.

5.3 Critical field and ionization probability

A simple classical picture of ionization of an atom under an intense field was given in 1977 by Bethe and Saltpeter [98], in which the Coulomb potential is modified by a stationary, homogeneous external electric field as

$$v(x) = -\frac{Ze^2}{x} - eE_{ext}x \tag{5.4}$$

where eE_{ext} is the force due to the external applied field. One can see that the Coulomb barrier is now suppressed and for $x \gg x_{max}$, where x_{max} is the position of the barrier after which the electron can tunnel through the potential well, is lower than the binding energy of the electron. The field at which the Coulomb barrier coincides with the energy level occupied by the electron under consideration is known as **critical field**. Neglecting the Stark effects, the critical field can be calculated as follows. The position of the barrier can be found by differentiating equation (5.4) w.r.t x and equating to zero.

$$\frac{\partial v(x)}{\partial x} = 0 \tag{5.5}$$

$$\frac{Ze^2}{x^2} - eE_{ext} = 0 \tag{5.6}$$

$$\Rightarrow \quad x_{max} = \sqrt{\frac{Ze}{E_{ext}}} \tag{5.7}$$

substituting $v(x_{max}) = E_{ion}$, one can obtain the threshold field strength at which ionization occurs as

$$E_c = \frac{E_{ion}^2}{4Ze^3} \tag{5.8}$$

and the corresponding critical intensity reads as

$$I_c = \frac{c\varepsilon_0}{2}E_c^2 = \frac{c\varepsilon_0 E_{ion}^4}{32Z^2e^6} \tag{5.9}$$

or, in a more convenient form

$$I_c = 4 \times 10^9 \left(\frac{E_{ion}}{eV}\right)^4 Z^{-2} W cm^{-2} \tag{5.10}$$

As a simplest example, for the hydrogen atom (Z = 1)

$$E_{ionH} = 13.6eV \tag{5.11}$$

where, a_B is the Bohr radius. Thus, the critical electric field is

$$E_c = \frac{E_{ionH}^2}{4e^3} = \frac{e}{16\pi\epsilon_0 a_B^2} \tag{5.12}$$

and hence, the critical intensity for ionization is $\simeq 1.4\times10^{14}Wcm^{-2}$. This simple analytical model by Bethe serves as a thumb rule to predict when a target will start to ionize. Once the critical field is reached, the ionization probability is very close to unity.

If the external applied electric field is less than the critical field (E_c) for ionization of an atom, ionization occurs via tunneling through the barrier formed by the atomic potential and by the maximum instantaneous field, provided that the time taken for the electron to pass through the barrier (tunneling time) is short compared to the cycle time. In this situation the oscillating field is effectively a static field of strength E while tunneling occurs. One should take care of the fact that tunneling time is not the ionization time. Indeed, if E is well below E_c the probability for tunneling during one cycle is exponentially small and although the photoelectron tunnels out at a particular phase of the cycle, the ionization time is very much longer than the tunneling time [99]. A prominent expression for calculating the ionization rate (i.e. tunneling probability per unit time) in a static electric field E is given by Landau and Lifschitz as

$$W_{QS}(t) = 4\frac{(2I_p)^{5/2}}{E(t)}exp\left(-\frac{2\,(2I_p)^{3/2}}{3E(t)}\right) \tag{5.13}$$

where I_p is the ionization potential of the atom, $E(t)$ is the laser electric field and suffix QS stands for quasi-static. The ionization rate has a highly non-linear dependence on the instantaneous value of the electric field. At the zero-crossing of the oscillating laser field, no potential barrier is created, hence the ionization is zero.

The other important ionization rate is the Ammosov-Delone-Krainov (ADK) rate, applicable to tunneling ionization in complex atoms. The initial state is characterized by the quantum numbers n^*, l^* and m. The ADK ionization rate is given as

$$W_{ADK} = I_p C_{n^*l^*} f(l,m) exp\left(-\frac{2(2I_p)^{3/2}}{3E_0}\right)\left(\frac{2(2I_p)^{3/2}}{E_0}\right)^{2n^*-|m|-1}\left(\frac{3E_0}{\pi(2I_p)^{3/2}}\right)^{1/2} \tag{5.14}$$

where

$$C_{n^*l^*} = \frac{2^{2n^*}}{n^*\Gamma(n^*+l^*+1)\Gamma(n^*-l^*)} \tag{5.15}$$

and

$$f(l,m) = \frac{(2l+1)(l+|m|)!}{2^{|m|}|m|!(l-|m|)!} \tag{5.16}$$

$n^* = \frac{Z}{\sqrt{2E_b}}$ and $l^* = n^* - 1$ are the effective principal and angular quantum numbers respectively and m is the magnetic quantum number. The factor $\left(\frac{3E_0}{\pi(2E_b)^{3/2}}\right)^{1/2}$ appears from averaging over a period of the field, while $\left(\frac{2(2E_b)^{3/2}}{E_0}\right)^{2n^*-|m|-1}$ takes into account the corrections for the Coulomb potential. In the derivation of ADK rate, a time average over one laser cycle is performed. However, in strong and rapidly rising laser pulses the absolute phase become important. A more accurate approach where the absolute time dependence was kept during the entire derivation of the ionization rate was proposed by Yudin and Ivanov [100]. They proposed an analytical expression for instantaneous ionization rates for arbitrary γ. Their analysis allows to explicitly distinguish between tunneling and multi-photon contribution to the total ionization probability. In the tunneling limit $(\gamma < 1)$ the ionization reproduces the quasi-static limit, while in the multi-photon limit $(\gamma > 1)$ the ionization probability no longer depends on the instantaneous value of the electric field. In particular, non-zero ionization probability is predicted even at the zero-crossing of the laser field. However, any tunneling ionization theory fails at higher intensities, simply because electron has no longer any barrier to overcome. Different approaches are then necessary to calculate the ionization rate, the most fundamental being numerical integration of the time-dependent Schrodinger equation.

5.4 Ionization model

Present days investigation of intense laser-plasma interaction studies rely extensively on numerical calculations due to the non-linearities and geometries involved in the problems. In this thesis a quantitaive evaluation of the degree of ionization for atomic species has been carried out using a numerical simulation based on a tunnel ionization model proposed by Yudin and Ivanov [100]. According to this model the rate of ionization of an atomic species is given as follows:

$$\Gamma = N(t) exp\left[-\left(\frac{E_0^2 f^2(t)}{\omega_L^3}\phi(\gamma,\theta)\right)\right] \tag{5.17}$$

where E_0 is the laser electric field amplitude, $f(t)$ is the pulse envolope and ω_L is the laser angular frequency and

$$\phi(\gamma,\theta) = \left(\gamma^2 + \sin^2\theta + \frac{1}{2}\right)\ln c - \frac{3\sqrt{b-a}}{2\sqrt{2}}\sin|\theta| - \frac{\sqrt{b+a}}{2\sqrt{2}}\gamma \tag{5.18}$$

where

$$\begin{aligned} a &= 1+\gamma^2-\sin^2\theta \\ b &= \sqrt{a^2+4\gamma^2\sin^2\theta} \\ c &= \sqrt{\left(\sqrt{\frac{b+a}{2}}+\gamma\right)^2+\left(\sqrt{\frac{b-a}{2}}+\sin|\theta|\right)^2} \\ \theta &= \omega_L t \\ \gamma &= \sqrt{\frac{I_p}{2U_p}} \\ U_p &= \frac{e^2E_0^2}{4m_e\omega_L^2} \end{aligned} \tag{5.19}$$

γ is the Keldysh parameter, I_p is ionization potential, U_p is average energy of electron oscillations in the laser field and θ is the phase of the laser field. The pre-exponential factor N(t) reads as

$$N(t) = A_{n^*,l^*}B_{l,|m|}\left(\frac{3\kappa}{\gamma^3}\right)^{\frac{1}{2}} CI_p\left(\frac{2(2I_p)^{\frac{3}{2}}}{Ef(t)}\right)^{2n^*-|m|-1} \tag{5.20}$$

where, A and B are depends on quantum numbers in exactly the same way as C and f depends in the case of ADK formula, and

$$\begin{aligned} \kappa &= \ln\left(\gamma+\sqrt{\gamma^2+1}\right) - \frac{\gamma}{\sqrt{\gamma^2+1}} \\ C &= \left(1+\gamma^2\right)\frac{|m|}{2} + \frac{3}{4}A_m(\omega_L,\gamma) \end{aligned}$$

for $\gamma \ll 1, C = 1$. For $\gamma \gg 1$ and m = 0, one has $A_0 \approx \frac{1.2}{\gamma^2}$ and $C \approx \frac{1.2}{\gamma}$. The ionization rate has a non-linear dependence on the instantaneous electric field. The exponential factor gives the strongest dependence on the electric field while the pre-exponential factor includes dependence on the initial state which is defined by its quantum numbers.

The numerical approach in the code, developed during this work, is based on a finite difference scheme. The code starts with setting up of laser and gas parameters, conversion into atomic units and proper initialization. In the code, a laser pulse of guassian profile in

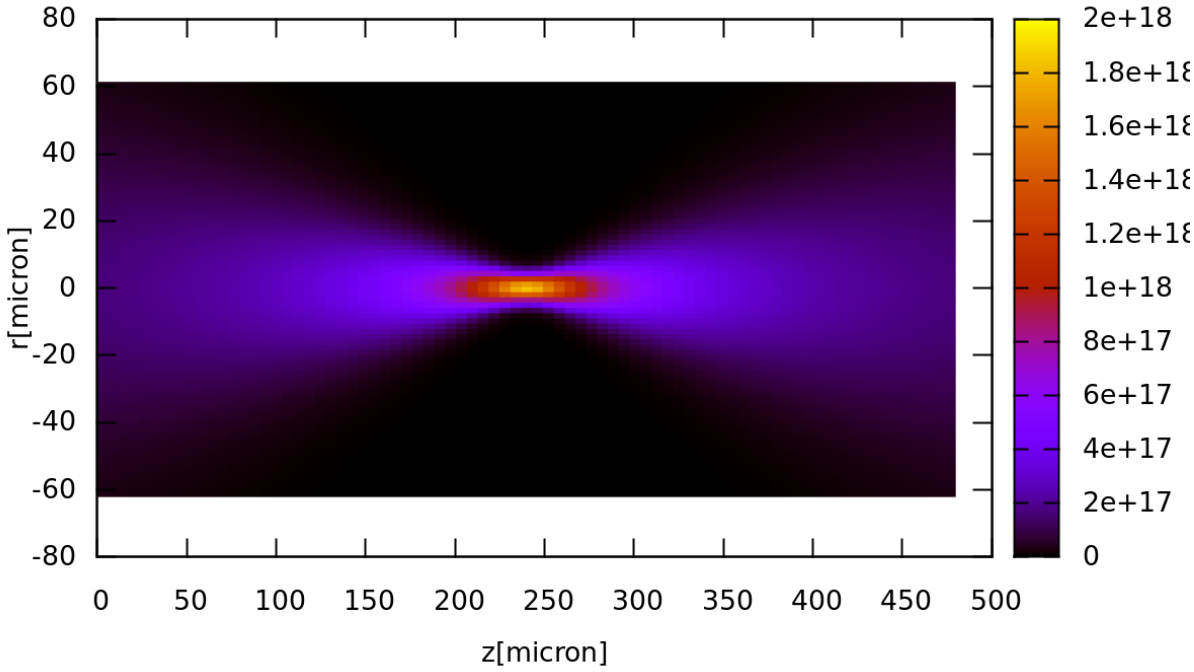

Figure 5.3: Intensity distribution of the Gaussian pulse used in the simulation. The side bar represents the intensity in Wcm^{-2}.

time and space was focused at the center of a step like uniform density profile of neutral gas medium. A co-moving time window is activated so that the gaseous medium appears to move to the left, while the laser pulse appears stationary. Since, the work done in this thesis is concerned with experiments in femtosecond time domain, any kind of recombination (which develops in the time of the order of ps) is not taken into account in the numerical calculations. The intensity profile of the guassian beam is given as

$$I = I_0 \left(\frac{w_0^2}{w(z)^2}\right) \exp\left[-2\left(\frac{r^2}{w(z)^2} + \frac{t^2}{\sigma^2}\right)\right] \tag{5.21}$$

In three dimensional space, for such a Gaussian laser pulse the iso-intensity shells will be pea-nut shaped. For convenience Fig.5.3 shows the spatial distribution of the intensity of the laser pulse with parameters given in table 5.1.

Simulations were performed for helium and nitrogen gases. The input laser parameters in the code are described in table 5.1.The population of electrons can be computed from rate equation. If any kind of recombination between electrons and ions is ignored the rate equation is given by:

$$\frac{dn_i}{dt} = \Gamma_i n_{i-1} - \Gamma_{i+1} n_i \tag{5.22}$$

Laser Pulse Parameter	**Value**
Type	Ti:Sapphire
Wavelength	800 nm
Pulse duration	65 fs
Pulse energy	$<$ 120 mJ
Max. power	up to 2 TW
Spot size radius	$5\mu m$
Pulse intensity	$1.95 \times 10^{18}\mathrm{Wcm}^{-2}$
a_0	0.95
M^2 parameter	2.5
Rayleigh length	$43.6\mu m$

Table 5.1: Input laser parameters for numerical calculations

The first term represents creation of ions with charge state Z from ions with charge Z-1; the second term depletion of the same ion due to further ionization. The rates Γ_i for each ion can be calculated from equation 5.17. For instance in case of helium, numerically this is done by solving two coupled equations:

$$\begin{aligned} \frac{dn_1}{dt} &= \Gamma_1 n_0 - \Gamma_2 n_1 \\ \frac{dn_2}{dt} &= \Gamma_2 n_1 \end{aligned} \tag{5.23}$$

Where n_0, n_1 and n_2 represents neutral He gas, He^+ ions and He^{2+} ions respectively. If ρ_0 is the total amount of the gas present before ionization, then

$$n_0 + n_1 + n_2 = \rho_0 \tag{5.24}$$

The difference equation corresponding to equation 5.23 is simply:

$$\begin{aligned} n_1^{i+1} &= n_1^i + \Delta t(n_0^i \Gamma^i - n_1^i \Gamma^{i+1}) \\ n_2^{i+1} &= n_2^i + \Delta t n_1^i \Gamma^{i+1} \end{aligned} \tag{5.25}$$

Finally, the total number of electrons is give by:

$$n_e = n_1 + 2n_2 \tag{5.26}$$

Atom	+1	+2	+3	+4	+5	+6	+7
N_2	14.53 eV	29.60 eV	47.45 eV	77.48 eV	97.89 eV	552.1 eV	667.1 eV
He	24.59 eV	54.42 eV	–	–	–	–	–

Table 5.2: Ionization potential of helium and nitrogen

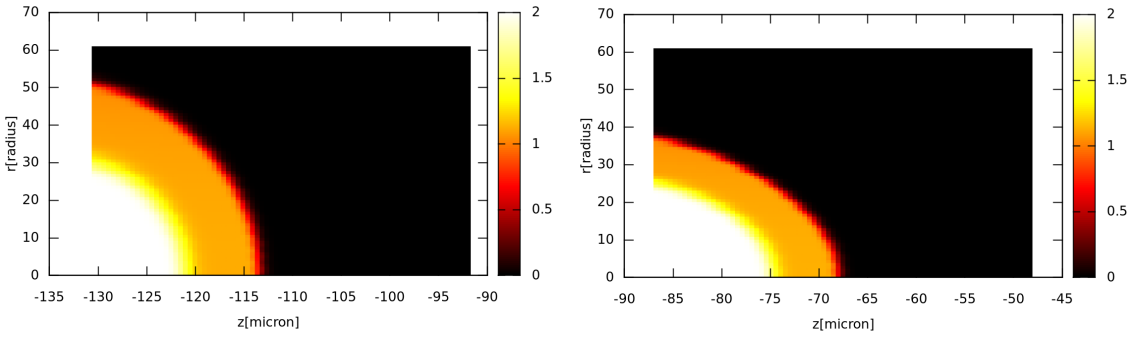

(a) (b)

Figure 5.4: Ionization map of Helium at different positions with respect to the best focus (zero position on the horizontal scale). (a) Ionization map at three Rayleigh lengths before the best focus. (b) Ionization map at two Rayleigh lengths before the best focus. The pulse is propagating from left to right. The side bar represents degree of ionization.

Equation 5.23 can be generalized for higher atomic number elements to calculate the electron density from individual ionization state in an iterative manner. Finally, total electron density was computed by properly summing up contribution from each ionized states. Suitable numerical check has been introduced in between the code to avoid any kind of abnormal divergence in the numerical results.

The ionization profiles are calculated for different positions of the laser pulse with respect to the beam waist. The degree of ionization is calculated for the front of the laser pulse. Figure 5.4 and 5.5 show the ionization profile in the case of helium gas, for four different positions relative to the beam waist. The pulse propagates from left to right. Figure 5.4(a) shows the ionization profile when the pulse is located at three Rayleigh lengths before the beam waist. Figure 5.4(b) shows the ionization profile when the pulse is at two Rayleigh lengths before the beam waist. Figure 5.5(a) shows the ionization profile when the pulse is at one Rayleigh length before the waist and finally Figure 5.5(b) shows the ionization profile at the beam waist. The graph shows that full ionization in case of helium gas occurs well before the pulse enters the best focal region. Full ionization remains confined to a small

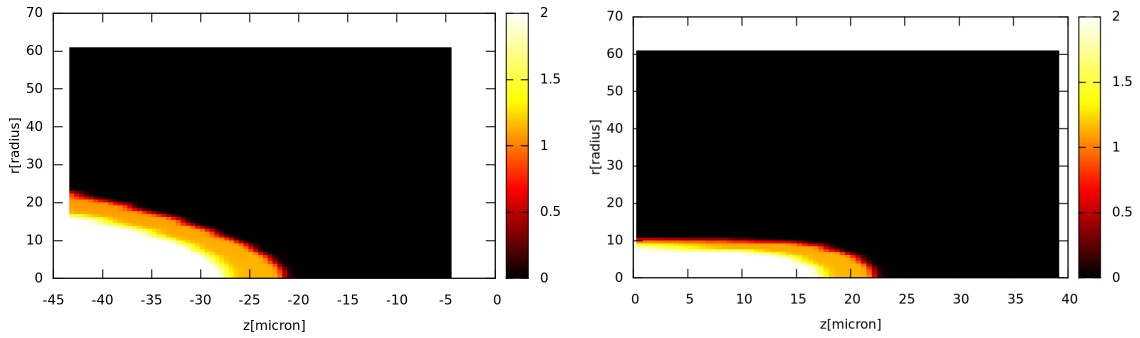

(a) (b)

Figure 5.5: Ionization map of Helium at different positions with respect to the best focus (zero position on the horizontal scale). (a) Ionization map at one Rayleigh length before the best focus. (b) Ionization map at the best focus. The pulse is propagating from left to right. The side bar represents degree of ionization.

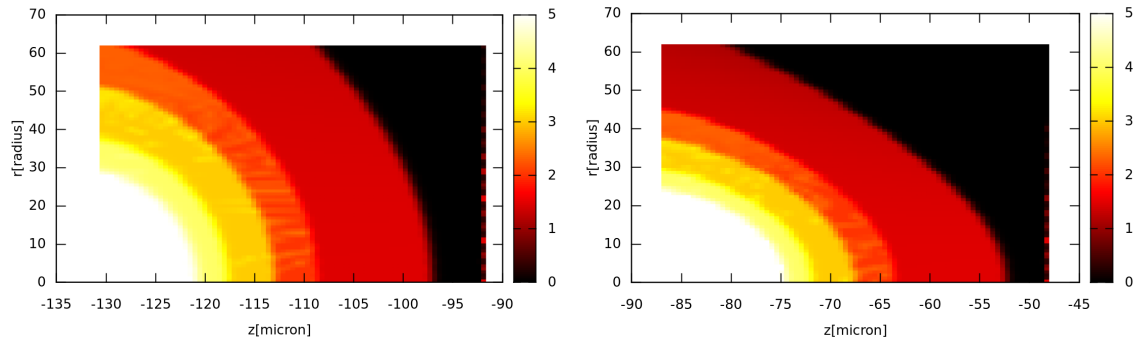

(a) (b)

Figure 5.6: Ionization map of Nitrogen at different positions with respect to the best focus (zero position on the horizontal scale). (a) Ionization map at three Rayleigh lengths before the best focus. (b) Ionization map at two Rayleigh lengths before the best focus. The pulse is propagating from left to right. The side bar represents degree of ionization.

volume and most of the available volume is mainly accompanied by partial ionization of the medium. Similarly, the degree of ionization is calculated for nitrogen gas. Figure 5.6 and 5.7 show the ionization profile in case of nitrogen gas at different position with respect to the beam waist. Figure 5.6(a) shows the ionization profile when the pulse is located at three Rayleigh lengths before the best focus. Figure 5.6(b) shows the ionization profile when the pulse is at two Rayleigh lengths before the the beam waist. Figure 5.7(a) shows the ionization profile when the pulse is at one Rayleigh length before the beam waist and finally

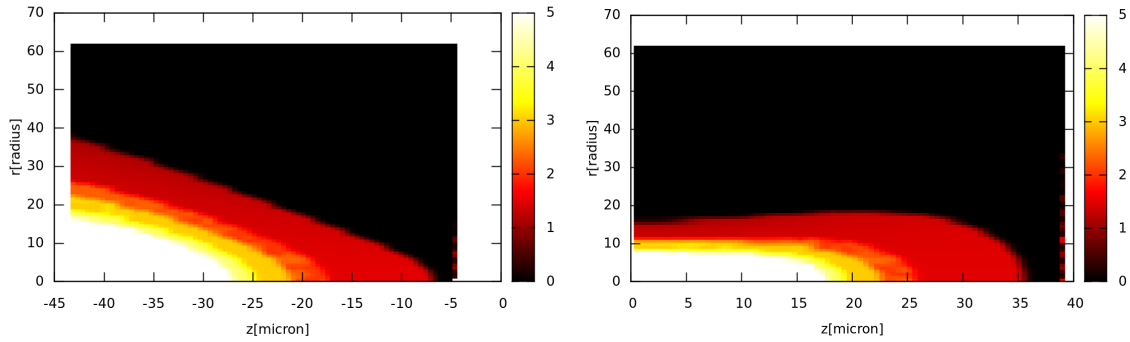

(a) (b)

Figure 5.7: Ionization map of Nitrogen at different positions with respect to the best focus (zero position on the horizontal scale). (a) Ionization map at one Rayleigh lengths before the best focus. (b) Ionization map at the best focus. The pulse is propagating from left to right. The side bar represents degree of ionization.

Figure 5.7(b) shows the ionization profile at the beam waist. These calculations show that ionization of nitrogen is very much different from that occurring in helium, where full ionization is easily achieved even before the best focus position. Ionization potential of helium and nitrogen gas are summarized in table 5.2. In our experimental conditions 6^{th} and 7^{th} ionization state of nitrogen gas is difficult to achieve. However, if the interaction process enter a non-linear self-focusing regime further ionization of the nitrogen gas is possible. To investigate this behaviour self-consistent electromagnetic wave propagation code including ionization of the medium is essential. Such codes are highly specialised and need massive computing facility. This is beyond the scope of the present work.

5.5 Prepulse effect on laser pulse propagation in gases

The propagation of an ultrashort laser pulse in the plasma can be affected by the light reaching the target before the main pulse. The ultrashort pulses are generally amplified by the chirped pulse amplification (CPA) technique. At the output of the CPA laser, the main intense femtosecond pulse is accompanied by a nanosecond pedestal due to amplified spontaneous emission and a picosecond pedestal due to the unavoidable limit in the compression of the chirped pulse. They create a low density plasma before the arrival of the main pulse. It is therefore important to evaluate the effect of this precursor pulse on the gas in the focal region.

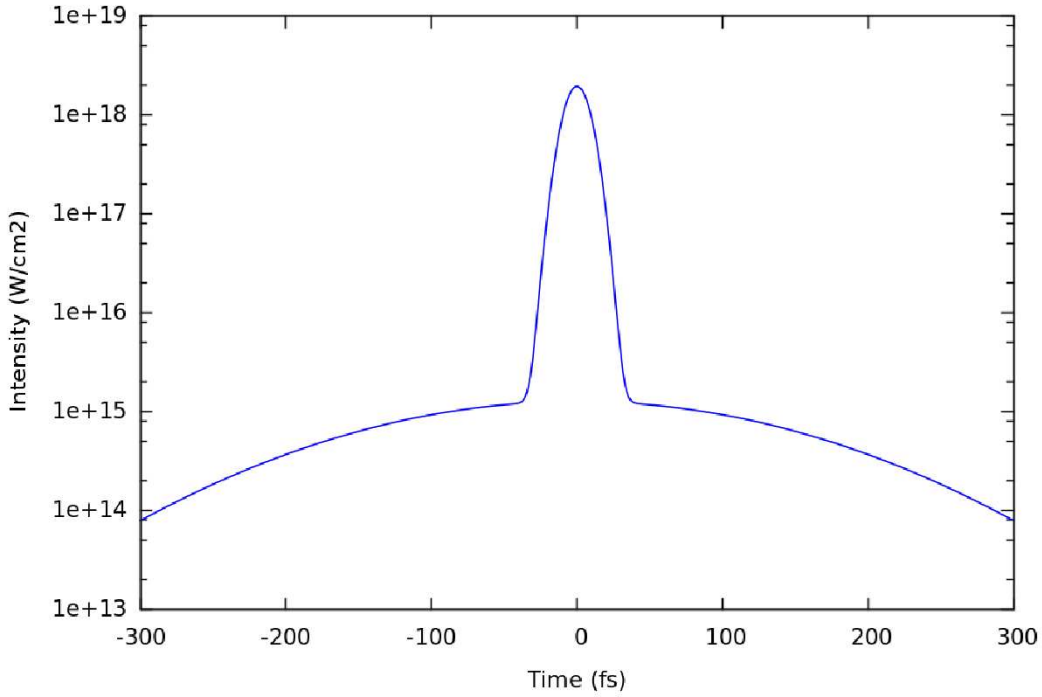

Figure 5.8: Intensity profile of the main pulse associating a low contrast ps pedestal.

There are several issues connected with the pre-plasma formation by the pre-pulse. Relevant aspects of ultrashort intense laser pulse propagation include early breakdown of the gas due to precursors of the main laser pulse [101] and ionization dominated regime of interaction [102] suitable for stable propagation. Normally, many picosecond before the main pulse the intensity contrast between the main and pre laser pulse is very high and the plasma formed by the pre pulse is negligible. On the other hand, for the time less than few tens of picosecond the contrast level is not high enough to prevent premature plasma formation and it is therefore important to know the effect of the pedestal pulse on the gas medium. We modelled this case for Helium gas, taking a simplified laser intensity profile as plotted in Figure 5.8. The numerical calculation were performed for three different contrast levels of picosecond pedestal. Figure 5.9 shows the result of the calculation. In Figure 5.9(a) it is observed that for a contrast level of 1.5×10^3 early breakdown of the gas medium starts by the picosecond pedestal at the best focal spot before the arrival of the main laser pulse. A narrow channel of partial ionization along the axis of the propagation of the laser pulse is formed. For a contrast level of 3.1×10^3 a small volume of the medium is ionized by the pre-pulse around the best focal position. Whereas, for picosecond pedestal contrast of $1.5 \times 10^4 W cm^{-2}$, Figure 5.9(b) shows that there is no pre-formed plasma and the interaction

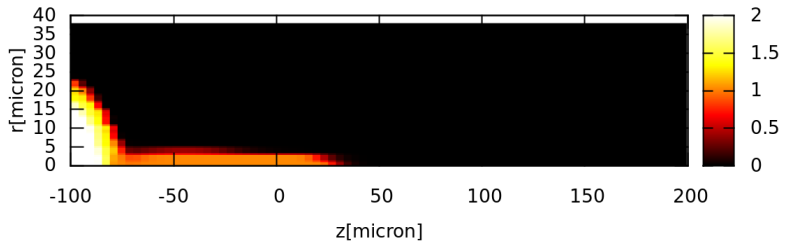

(a)

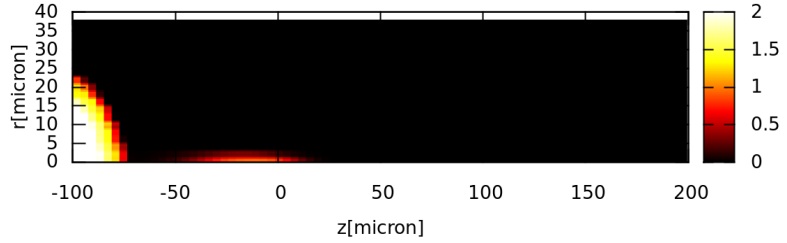

(b)

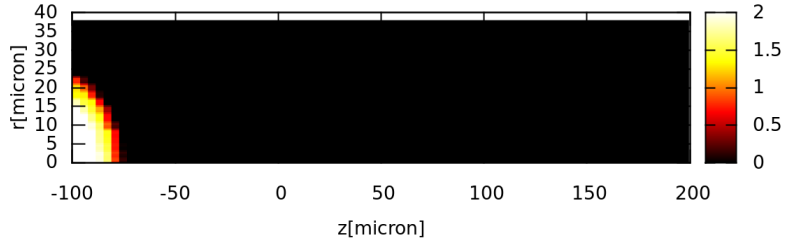

(c)

Figure 5.9: Propagation of a femtosecond laser pulse, accompanied by a picosecond (ps) pedestal, in Helium gas. Figure shows the ionization induced by the pre-pulse before the arrival of main laser pulse. (a) The contrast level between the main and ps pedestal is 1.5×10^3. (b) The contrast level between the main and ps pedestal is 3.1×10^3. (c) The contrast level between the main and ps pedestal is 1.5×10^4. No pre plasma formed for contrast ratio $\geq 1.5 \times 10^4$. The pulse is propagating from left to right. The side bar represents degree of ionization.

can be characterized as a clean interaction of the main laser pulse with neutral gas medium.

5.6 Conclusion

In this chapter numerical work concerning the ionization of the neutral gas medium by the incident laser pulse is presented. The distribution of electron density within different volume interval and at different positions before the pulse could reach the best focus is

estimated quantitatively. The effect of the pre-pulse at different levels of contrast ratio is calculated. The knowledge of the plasma formation by the pre-pulse is very useful from an experimental point of view. If controlled in a proper way, pre-plasma may help the stable propagation of the main laser pulse by forming a channel or cavity. This may also act as a spatial filter for the main pulse as demonstrated experimentally by Giulietti et al. [101]. Hosokai et al. [103] studied experimentally the effect of the laser pre-pulse on the injection and acceleration process showing that the acceleration depends strongly on the laser pre-pulse parameters. It has also been observed that the magnetized pre-plasma can potentially affect the emittance and total charge of the accelerated electron bunch [104]. Generally, the effect of the pre-pulse is more significant with very high power laser system where the intensity at the focus exceeds $10^{18} W cm^{-2}$ value. The pre-pulse can spoil or enhance the propagation of the main pulse depending on the nature and time scale of the contrast level. The ionization dynamics is partially responsible for the scattering of electromagnetic waves in plasmas. In view of all the above mentioned physical processes it is useful to have a knowledge of the ionization of the medium under the influence of incident laser fields.

Part IV

Experimental description and discussion: Part I

CHAPTER 6

Electron acceleration with a moderate power laser system

6.1 Outline

This chapter describes the initial experiment on electron acceleration using the 2 TW Ti:Sapphire laser system at ILIL laboratory in National Institute of Optics (INO), CNR, Pisa. A complete description of the experimental set-up and diagnostics is given. The main objective of the experiment was to study the propagation of the laser pulse in different gases in order to search for suitable conditions for electron acceleration. For this purpose time resolved interferometry was used to study and control the evolution of the electron density. Thomson scattering and γ-ray detection were used to optimize the laser gas interaction conditions and magnetic spectrometer was used to characterize the energy spectrum of the electron bunches that were finally generated in laser plasma interaction.

In Section 6.2 a brief description of the laser system used in the experiment is given. Section 6.3 gives an overview of the experimental set-up. In Section 6.4 all the diagnostics used in the experiment are described. In section 6.5 experimental results are presented and discussed. Finally, in section 6.6 Particle-In-Cell simulations used as a tool to analyse the laser-plasma interaction are discussed.

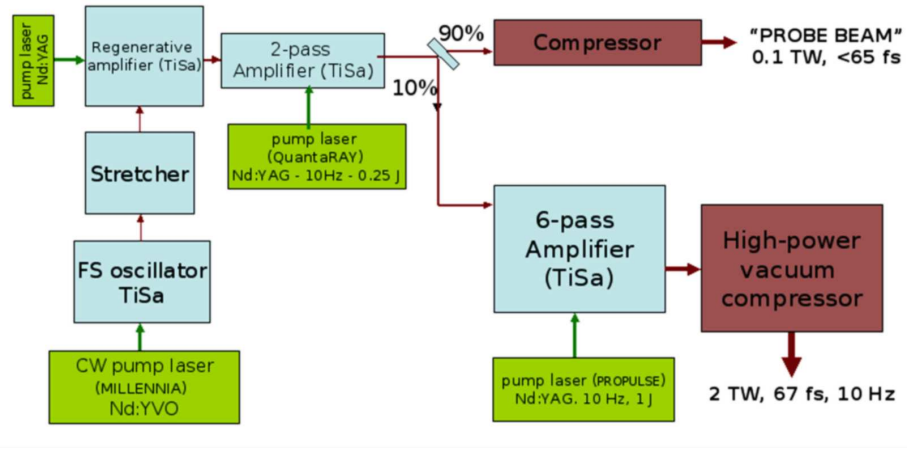

Figure 6.1: Schematic of the CPA system at the Intense Laser Irradiation Laboratory.

6.2 The Ti:Sapphire laser system at Intense Laser Irradiation Laboratory

For our experiment, we have used a Ti:Sapphire laser system designed to deliver ultra short pulses with a 10 Hz repetition rate. It is based on the ”Chirped Pulse Amplification” scheme and consists of an oscillator, pulse stretcher, a regenerative amplifier pumped by a frequency doubled Nd:YAG laser, a multi-pass pre-amplifier, another multi-pass amplifier and a pulse compressor. To amplify ultra-short pulses at 800 nm, titanium-sapphire crystals are used. Such crystals absorb energy from a pump laser emitting at 532 nm (green emission) and emit broad band spectrum from 750 to 850 nm. A schematic view of the entire system is shown in figure 6.1.

A femtosecond oscillator (Spectra Physics, Tsunami), generates fs pulses at a very high repetition rate (82 MHz). The pulses produced in such an oscillator have only a few nanojoule of energy per pulse. In order to amplify the laser pulses up to hundreds of mJ level, chirped pulse amplification technique is used to ramp up the energy without damaging the optical components. Chirping refers to the temporal stretching of the laser pulses. This stretching is achieved by use of diffraction gratings. A simple grating stretcher introduces a positive chrip i.e. the components with lower frequencies leave the stretcher earlier than the high-frequency components. The following is a basic outline of the amplification process employed:

1. Pulses are generated in the oscillator with energy greater than 4 nJ, at a frequency of

82 MHz, and pulse duration less than 50 fs.

2. Diffraction gratings are used to temporally stretch each pulse up to more than 200 ps. This step decreases the beam intensity ensuring that no optical damage occurs during amplification.

3. From the train of stretched pulses, a pulse selector (utilizing a Pockel cell) selects a single pulse and send it in the regenerative amplifier. This increases the beam energy up to 3 mJ level.

4. The stretched pulses are further amplified by a two-pass amplifier pumped by another, frequency doubled, Nd:YAG laser.

5. The output pulse, containing an energy of amproximately 15 mJ, is then split in two pulses containing 90% and 10% of the initial energy respectively.

6. The 90 percent pulse is expanded to a 7 mm diameter and compressed using a single grating (folded) compressor to obtain a final pulse duration of less than 65 fs.

7. The remaining 10 percent pulse is further amplified by a 6-pass bow-tie type amplifier (pumped by a frequency doubled Nd:YAG laser delivering 1 J pulses at 532 nm). This amplification stage uses a 2 cm diameter Ti:Sa crystal bringing the final energy up to 120 mJ.

8. The laser pulses are expanded spatially to a 33 mm diameter beam and compressed in time by a two grating placed under vacuum. The pulses with a final pulse duration of 65 fs and are then transported under vacuum into the target chamber via two beam steering, motorised turning mirrors, placed in two separate small vacuum chambers. The final power of the pulse at the target is about 2 TW.

6.3 Experimental set-up

The experiment was carried out at the ILIL laboratory using the 2 TW Ti:Sapphire laser system. In the experiment, a small part of the main pulse is split, doubled in frequency (using a BBO crystal) and used as a probe pulse for interferometry. The main laser pulse was

Parameters	Value
Type	Ti:Sapphire
Wavelength	800 nm
Pulse Duration	$\sim$ 65 fs
Max. Energy	$<$ 120 mJ
Max. Power	up to 2 TW
Focusing Optics	F/6 OAP

Table 6.1: Summary of laser system at ILIL

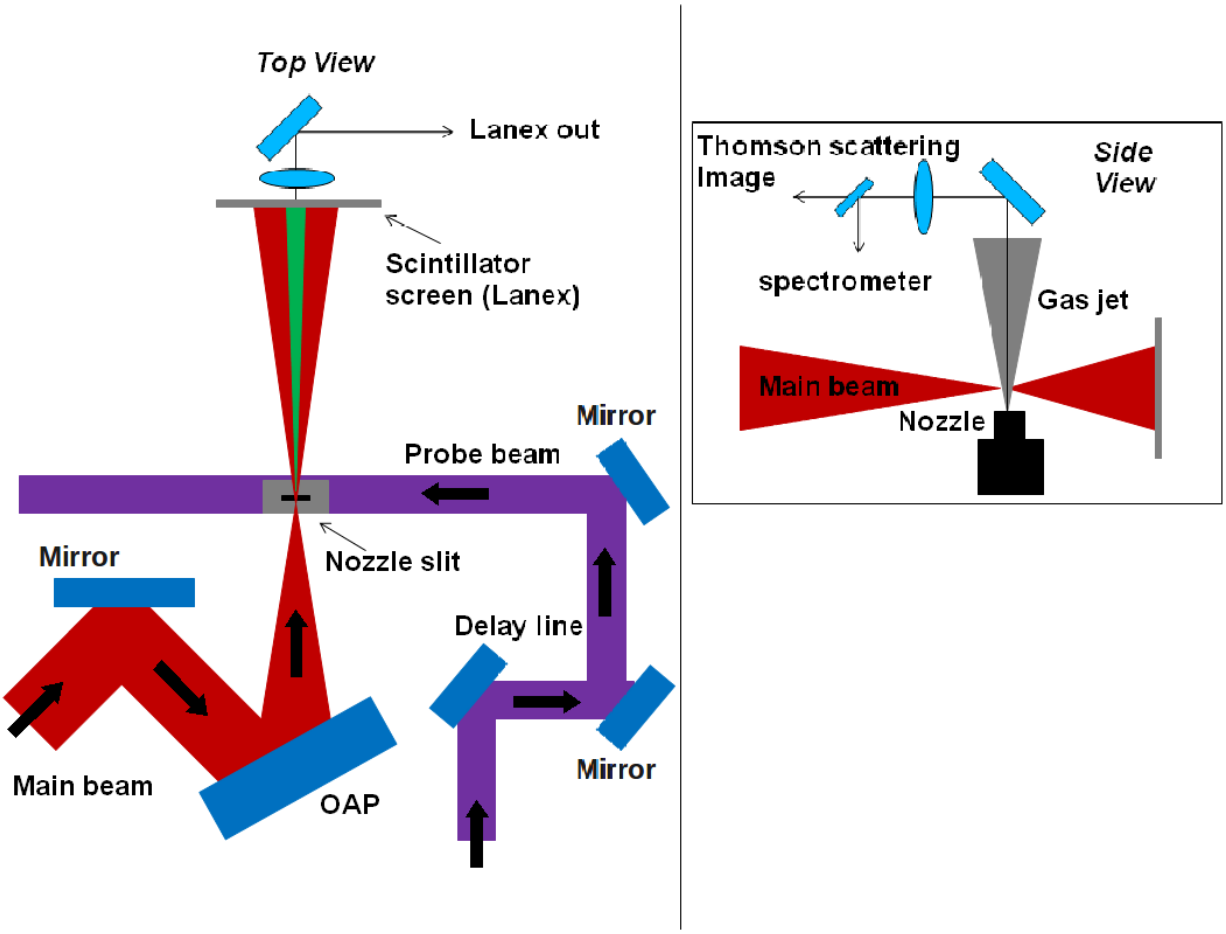

Figure 6.2: Experimental set up scheme. Left side: The main laser beam, probe line and the diagnostics arrangement is shown. Right side: Schematic of Thomson Scattering diagnostic.

focused down to a 10μm spot diameter using an F/6 off axis parabolic mirror. The experimental set up is illustrated in Figure 6.2. The experiment was mainly devoted to optimise

conditions for electron acceleration by varying the gas density and laser pulse duration. The gas density was controlled by changing the backing pressure of the nozzle of the gas jet, while the pulse duration required a tuning of the gratings. By scanning the position of the best focus into the gas-jet the optimal conditions for electron acceleration are found. The probe laser pulse was used for Nomarsky modified interferomentry [105], to obtain electron density evolution. Thomson scattering diagnostic, consisting of an imaging system for the scattering region and a spectrometer, was set to retrieve information on the laser propagation. A phosphor screen (LANEX), placed along the laser propagation axis, was used to detect the accelerated electron bunch. The detailed description of all the diagnostics will be presented in subsequent sections.

6.4 Diagnostics

In our experiment four main diagnostics were employed to monitor the laser-gas interaction. These include Thomson scattering, interferometry, scintillators coupled to photomultipliers and phosphor screen. Thomson scattering diagnostic is useful to investigate laser pulse propagation in plasma and interferometry gives the time evolution of the plasma density. A set of scintillators was used to detect the γ-ray production, which is strictly linked to electron generation. The phosphor screen (Lanex) was used to detect the electron signals. It also gives the spatial profile of the electron bunch. Finally, the electron bunch energy spectrum was measured using a magnetic spectrometer.

6.4.1 Gas-jet target

Generally, pulsed gas targets are used for laser plasma acceleration experiments. In our experiment a commercially available supersonic, laminar gas-jet target was used. The gas jet target consists of a reservoir of gas under high pressure, an electrically controlled valve and a nozzle (Fig.6.3). When the valve is activated gas flows out of the nozzle. The gas flow is driven by the backing pressure. The maximum opening time of the gas jet is 3 ms. As soon as a steady state flow has developed the laser is fired into the gas jet which exits from the slit and expands into the vacuum. The dimension of the exit slit of the nozzle is $1.2\mathrm{mm} \times 4\mathrm{mm}$. Supersonic gas jets are preferred as they produce a sharp interface between vacuum and neutral gas density. In fact smooth gradient between vacuum

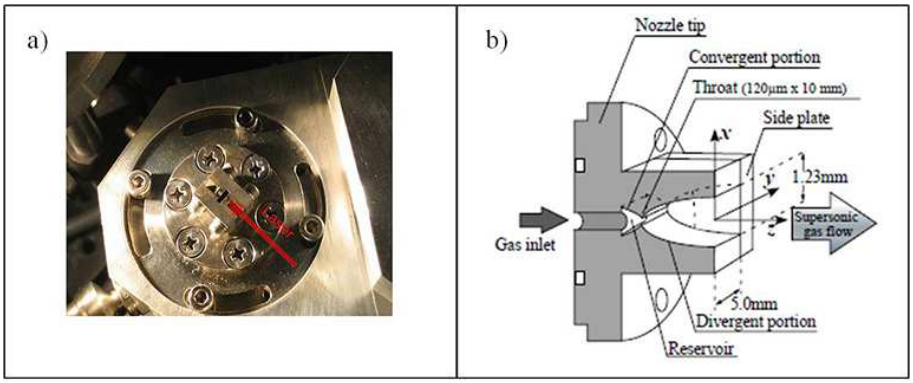

Figure 6.3: (a) Top view of the supersonic gas-jet used in the experiment. Arrow indicate the direction of laser propagation. (b) Internal shape of the gas-jet. Courtesy Prof. T. Hosokai.

and neutral gas density introduce inhomogeneity in the gas density profile. Smooth density profiles are not good as they can cause ionization induced defocusing of the laser pulse and limit the focusability of the pulse. An ideal supersonic gas-jet is the one which produce step like interface between the vacuum and neutral gas density with a flat top profile. This corresponds to a homogeneous neutral gas density profile. Homogeneity implies that stable or steady state gas flow has developed before the arrival of the main laser pulse.

6.4.2 Thomson scattering

In order to study the propagation of the laser pulse in plasma we detected Thomson scattered light at 90 degree to the laser propagation direction. Thomson scattering is a process by which the energy of an electromagnetic wave is partly scattered in various directions by free electrons. The electric field of the incident wave puts an electron into oscillatory motion and the electron emits a fraction of the incident laser energy as a dipole radiator. The properties of this scattered radiation are thus related to the properties of the medium. This fact has been investigated in this thesis and will be discussed later (in chapter 7). Thomson scattering diagnostic provides a useful support for monitoring the laser pulse propagation during its interaction with the gas medium. It gives an on-line information of the interaction length between the laser pulse and plasma and thus can be used to optimize the best conditions for electron acceleration.

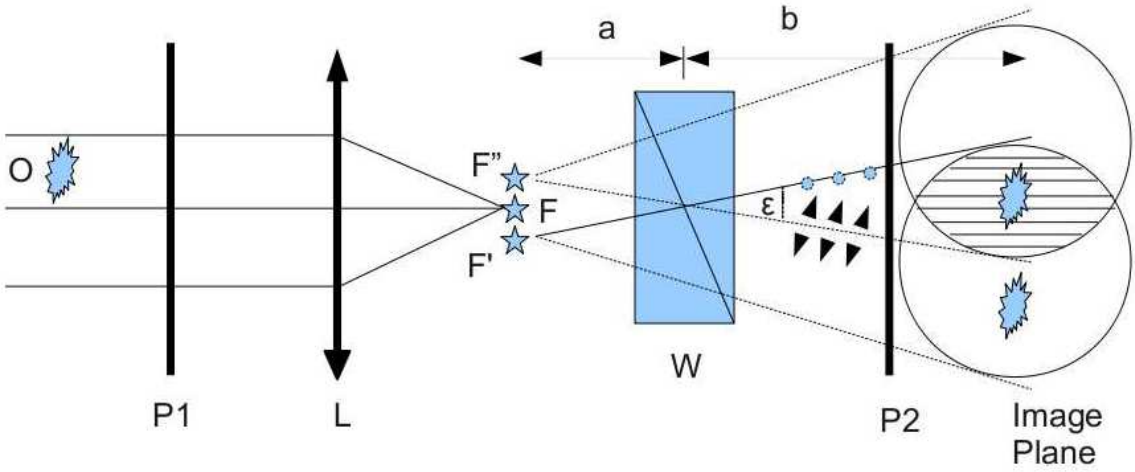

Figure 6.4: Set up of the Nomarsky interferometry.

6.4.3 Optical probing of plasma

In our experiment Nomarsky interferometry is used as an optical probing of the plasma generated by the main laser pulse [105]. The peculiarity of this interferometric technique is that the reference beam is extracted from the same probe beam by splitting the orthogonal components of the electromagnetic wave polarization vectors using a birefringent Wollaston prism. Using a Wollaston prism as a beam splitter, the main advantages are its relative simple set-up, the absence of alignment and stability problems.

The working principle of the interferometry is as follows. Let us assume the probe laser is polarized at 45 degree to the vertical direction. A lens is used in the interferometer after the target (plasma). After passing through the lens, the beam converges to a focus and diverges in a spherical wavefront. As the diverging beam passes through the Wollaston prism it is split into two beams (one with vertical and the other with horizontal polarization) with an angular separation. The diverging beams in the two polarizations can be projected backwards to two apparent foci, which are the centres of the two spherical wavefronts for the interferometer. A polarizer, oriented parallel or perpendicular to the 45 degree incident polarization, is placed in between the Wollaston prism and detector so that the transmission is the same for both polarizations and the two beams will interfere at the detector plane.

A typical set up for the Nomarsky interferometer for plasma density measurement is reported in Fig.6.4. The interferometer ensures equal optical path length between ordinary and

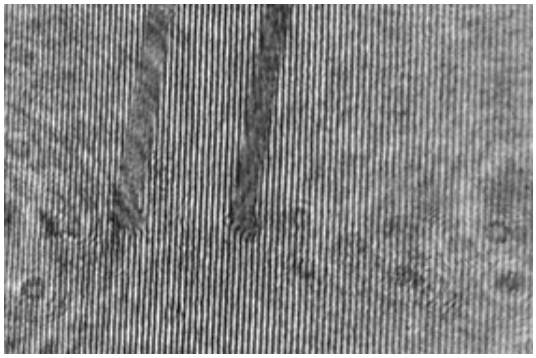

Figure 6.5: Imaging of a $60\mu\mathrm{m}$ wire for calibration. Two non-overlapped images formed on the screen. The calibration gives a relation between the pixel size and practical units and minimum resolution obtained.

extraordinary rays. It is therefore ideally suited for illumination with very short pulses with their inherently low temporal coherence. The spatial resolution of the system is determined only by the quality of the imaging lens and can therefore reach high values. The fringe separation can be adjusted by the spacing between imaging lens and Wollaston prism. The Nomarsky interferometer produces two partially overlapped images of the region of interest, so two images of the targets are visible in the detector plane.

In Figure 6.4, the object 'O'(i.e. the plasma) is imaged by a lens 'L' onto the image plane. The Wollaston prism 'W' splits the probe into two orthogonally polarized beams, that appear to be coming from two virtual foci F' and F". As a result, two orthogonally polarized images are created. Interference between the two beams in their overlapping regions is achieved by the polarizer 'P2'. The contrast of the fringes with the background depends on the orientation of the polarizer P2. The fringe separation δ in a Nomarsky interferometer is given by

$$\delta = \frac{\lambda b}{\varepsilon a} \tag{6.1}$$

where ε is the angle between the orthogonal polarized beams created by the Wollaston prism, λ is the probe wavelength, a is the separation distance between prism and focusing lens and b is the separation between the prism and the detector plane. So the separation between the fringes can be easily varied by changing the distance between the focus of the lens and the Wollaston prism. The fringe orientation can also be varied by a rotation of the Wollaston prism.

The timing between the main and the probe (interferometry) pulses was performed by first anticipating the probe beam and then starting delaying it until a fringe shift was ob-

served in the interferogram, produced by a small plasma formation just before the arrival of the probe beam. Finally, the spatial calibration of the interferogram is essential to know the extent of propagation of the laser pulse. This is done by imaging a wire of known radial dimension. The imaging system described in fig.6.4 produces two non-overlapped images of the wire. This is shown in fig.6.5. The dimension of the wire in the image can be calculated in terms of pixel. This gives a relation between the number of pixels and the radial dimension of the wire. In our case this turns out to be $1\text{pixel} = 0.3\mu\text{m}$. The minimum resolution can be known by observing how many fringes are overlapped completely by the wire. For example, if 3 fringes are completely overlapped by the wire of radial dimension $60\mu\text{m}$ than the minimum resolution of $20\mu\text{m}$ can be achieved. The two images of the wire are separated by a distance $\approx 300\mu\text{m}$. Hence, for plasmas extending more than this separation, overlapping of the two images occurs, and it is not possible to make a correct analysis of the interferogram.

6.4.4 Electron beam characterization

In technological applications electron beam quality is of utmost importance. It is, therefore, necessary to employ reliable characterization methods for electron beam monitoring. These characterization methods can be grouped as: detection, imaging, energy analysis and stability.

Primary signature of the electron generation is monitored with scintillators. The electrons collide with the walls of the chamber and generate γ-rays, which are detected with scintillators and measured directly on oscilloscope. The signal obtained with scintillators enable us to monitor the best conditions for electron acceleration in terms of reproducibility of the signal.

Imaging of the transverse pattern of the electron bunch is performed using a scintillating material, a Kodak LANEX screen, which is placed at a short distance behind a magnet. An imaging camera is positioned at a view port near the LANEX but not in the beam path (energetic electrons would saturate the camera and cause burn damage). The camera, thus placed, provides a real time image of the electron beam position, shape, and intensity. The spatial extent and divergence of the electron beam from laser axis are measured from LANEX screen data.

The energy spectrum of the electrons accelerated along the axis of laser propagation was measured using a magnetic spectrometer. At the entrance to the spectrometer there

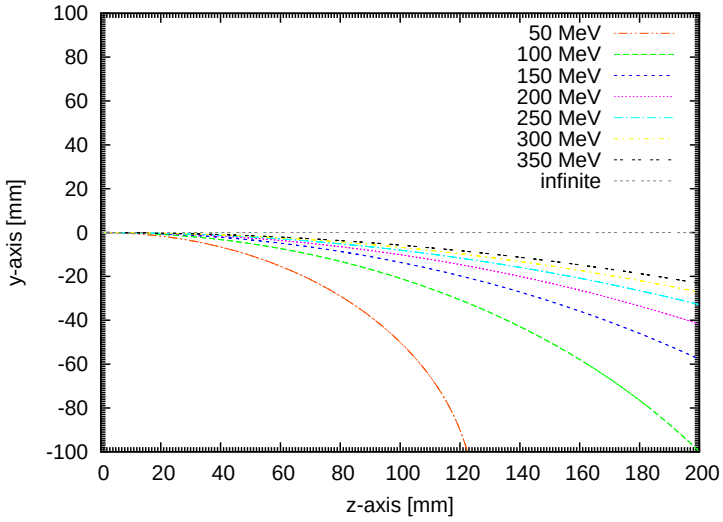

Figure 6.6: Trajectory of electrons entering in a magnetic field with different initial energies. Depending on their initial energy, electrons are dispersed and follow different Larmor radius. The ability of magnetic field to disperse the electrons depending on their initial energy make it a suitable device for energy spectrum measurement.

is a 0.5 mm hole to collimate the electron beam. This reduces the level of background signal from low energy x-rays and electrons. The magnetic field region between the poles was mapped using a Hall probe and is very uniform except near the edges of the poles. The correspondence between electron energy and deflection from the axis is found using a numerical algorithm (cf. Fig 6.6).

In the following discussion we will derive a mathematical relationship between the radius of curvature of the circular trajectory, followed by the electron in the magnetic field, and its energy. We assume that the electrons are entering the magnetic field in the z direction, and the magnetic field is along the x direction. Fig.6.7 indicates the electron trajectory and the magnetic field direction. The path of the electrons within the magnetic field is the Larmor orbit in the y-z plane whose radius is given by:

$$\begin{aligned} evB &= \frac{\gamma m v^2}{R} \\ R &= \frac{\gamma m v}{eB} = \frac{p}{eB} \end{aligned} \tag{6.2}$$

where, R is the radius of curvature of the electron circular trajectory and p is the relativistic momentum of the electron. The energy-momentum relation for a relativistic particle is

$$E^2 = (pc)^2 + (mc^2)^2 \tag{6.3}$$

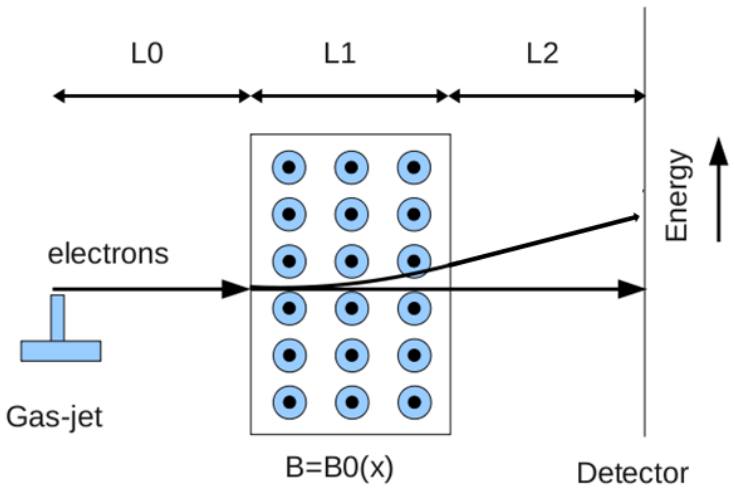

Figure 6.7: The lay out of the electron trajectory from its generation up to detection. Electron after generating from the gas jet target, which is at a distance L0 from the entrance of the magnetic field, entered into magnetic spectrograph of length L1. Depending on its initial energy the electrons get dispersed by the magnetic field and hit the detector plane, which is at a distance L2 from the exit of the magnetic field, at different positions.

where, E is the total energy of the charged particle. Substituting for pc from equation 6.2 into equation 6.3, we have

$$R = \frac{mc}{eB}\sqrt{\gamma^2 - 1} \tag{6.4}$$

Thus, the electron will follow a circular path whose radius is governed by the energy of the electron entering in the magnetic field region. Knowing the relativistic Larmor radius, the electron trajectory can be defined.

To find a complete relation between the electron energy and its position on the detector plane, one needs to consider the coordinates of the entrance point (P1) of the electron in the magnetic field, the magnetic field extension (L1) and radius of electron trajectory in the magnetic field as shown in Fig.6.8. With these informations, the coordinates of the exit point (P2) of the electron from the magnetic field can be calculated. The trajectory of the exiting electron is given by the slope of the line followed by the electron after exiting out from the magnetic field. Fig.6.9 shows the position of such an electron beam on the detector screen as a function of its initial energy.

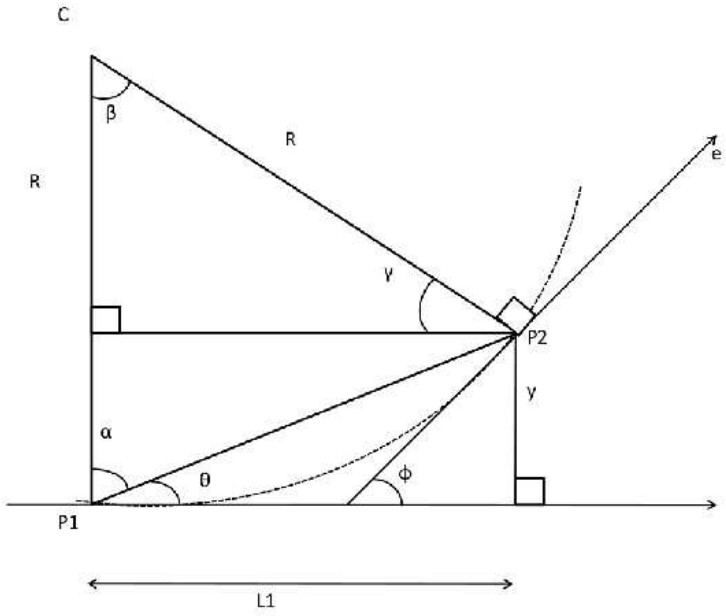

Figure 6.8: Trajectory of an electron passing through a magnetic spectrograph. The dotted curve represents the Larmor orbit of the electron in the magnetic field.

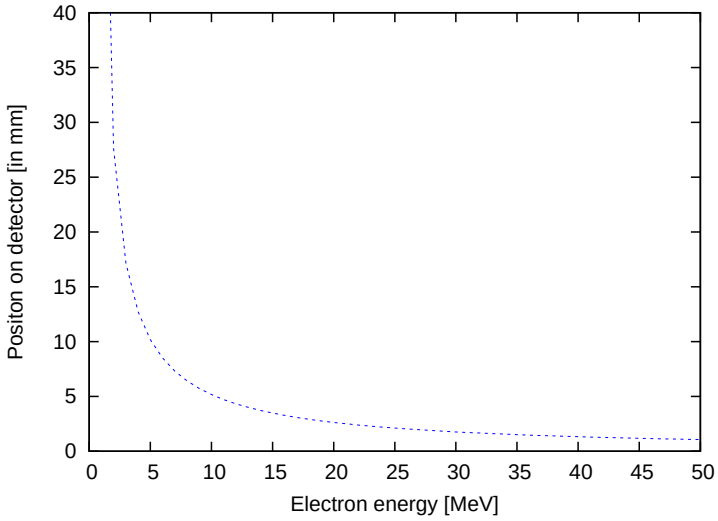

Figure 6.9: Electron position on the detector plane as a function of its initial energy .

6.5 Experimental results and discussion

In this section we will discuss the experimental results obtained with different diagnostics used in the experiment.

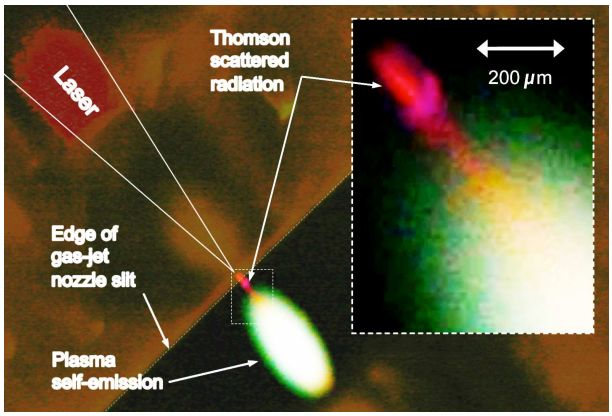

Figure 6.10: Image of the gas-jet nozzle obtained from the Thomson scattering diagnostic. The laser pulse is focused on the edge of the gas jet. Thomson scattering radiation can be seen clearly (red in colour). Beyond that point, the laser pulse expands and the emission visible in the image is dominated by white light generated by plasma emission. Inset: The magnified region of the interaction.

Thomson scattering

To monitor the propagation of the laser pulse in a plasma the Thomson scattering diagnostic was used. The imaging of the interaction region was performed with a magnification of 10 using an achromatic doublet lens and imaging camera. The spatial resolution of the imaging system was limited by the pixel size of the camera. Fig.6.10 shows the imaging of the scattering zone when the backing pressure of the gas jet was 30 bar. The laser was focused at the entrance of the gas jet. One can notice the Thomson scattered light (red in colour). The length of the scattered region is around twice the Rayleigh length $(\approx 100\mu\mathrm{m})$, indicating possible self-focusing of the laser pulse in plasmas. Beyond that point, the laser beam expands and the emission is dominated by the plasma self-emission.

Interferometry

In the experiment the electron density evolution was studied with optical interferometry. The interferogram of Fig.6.11 was taken at 2 ps after the arrival of the main pulse. The backing pressure of the gas jet (nitrgoen) was 35 bar. The focus position of the laser pulse was $50\mu\mathrm{m}$ inside from the entrance edge and $400\mu\mathrm{m}$ above the gas jet.

The interferograms have been deconvolved with a fringe-analysis technique that makes use of a continuous-wavelet-transform ridge-extraction algorithm to extract the phase-difference map, evidencing local phase variations with a higher degree of accuracy than other FFT-

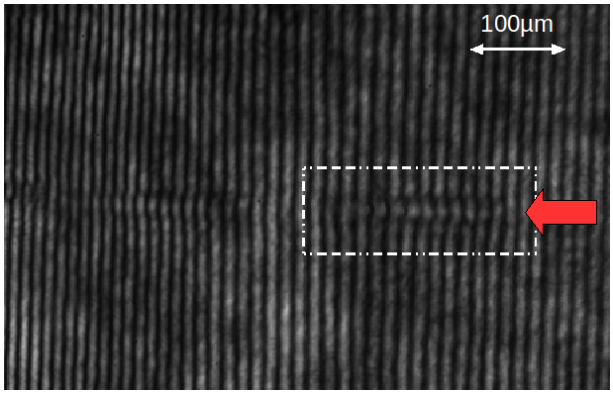

Figure 6.11: Interferogram representing the fringe shift. The interferogram is recorded 2 ps after the arrival of the main pulse. The backing pressure of the gas jet was 35 bar. The arrow indicates the direction of the laser pulse propagation.

based techniques [106]. Electron-density distributions are thus retrieved with higher accuracy and with low noise. Interferometric patterns have been analyzed with particular attention to some artifacts in phase-difference maps reconstruction that can be connected with the transit time of the probe through the plasma [107, 108]. The interferometry gave us a real-time diagnostic in order to search for the best conditions to achieve efficient electron acceleration, by allowing us to control the plasma-electron-density distribution.

Figure 6.12(a) shows the electron density map and Fig. 6.12(b) shows the three-dimensional plot of the electron density obtained for the fringe pattern shown in Fig. 6.11. The electron density is of the order of $10^{19}\mathrm{cm}^{-3}$. The maximum electron density obtained in the experiment was measured around $\sim 7 \times 10^{19}\mathrm{cm}^{-3}$. The electron density has a maximum along the longitudinal axis, since at this time the shock wave that is hydro-dynamically set-on by the laser-energy deposition in the focal region has not yet developed enough to deplete the on-axis region and form a hollow channel [109].

Electron bunch profile and energy spectrum

The single shot experiments are very statistical in nature due to the fact that laser and gas jet parameters vary from shot to shot and therefore it is hard to have a fine control on the interaction conditions. However, in the experiment the best conditions for acceleration are found by scanning the focal position of the laser with respect to the gas jet and monitoring the scattered signal from Thomson diagnostic and γ ray signal by scintillators. Fig.6.13

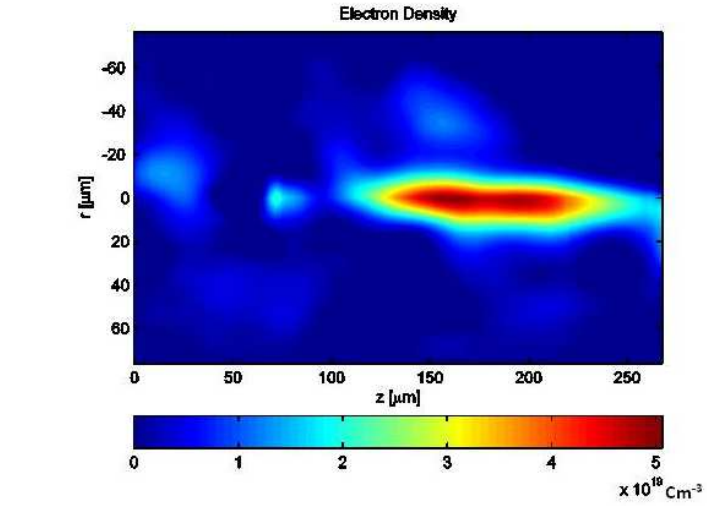

(a)

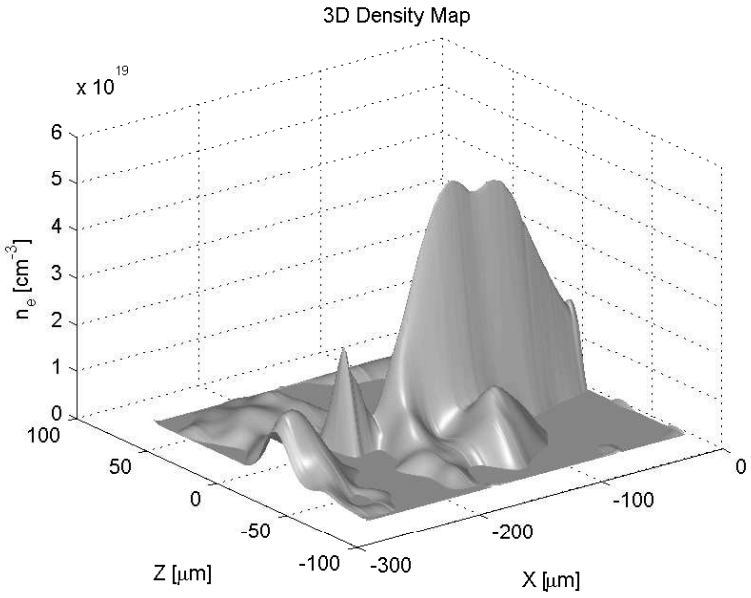

(b)

Figure 6.12: (a) The map (in false color) of the electron density obtained from the interferogram of Fig.6.11 and (b) the related 3D electron density profile.

shows a set of results performed with Helium gas target. These results indicate a direct correlation between the Thomson scattered light and electron signal on the detector. One can observe that the divergence of the electron bunch decreases as the length of the Thomson

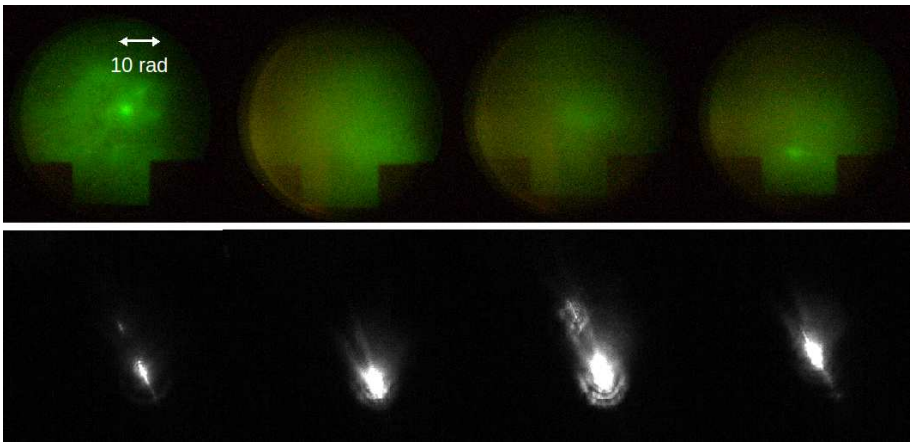

(a)

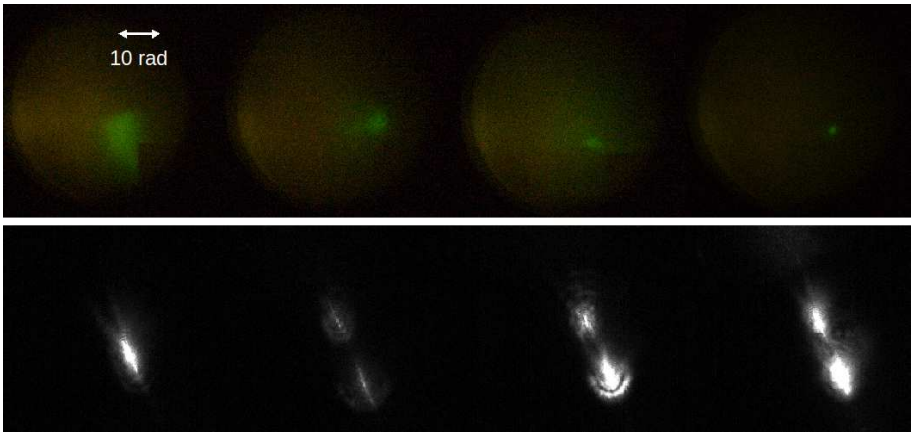

(b)

Figure 6.13: The typical spatial profile of the electron bunch [upper figures in (a) and (b)] and their corresponding Thomson scattering (TS) images [lower figures in (a) and (b)]. TS diagnostic monitors the propagation of the laser pulse in the plasmas. One can notice the correlation between the length and the intensity of the Thomson scattered light and electron bunch divergence. Portion of the gas jet nozzle is visible in the figure. The backing pressure of the helium gas-jet was 35 bar and the waist position is in the vicinity of the entrance edge of the gas-jet.

scattering region increases. In addition, reduced radial extent of the scattering region corresponds to less diverging electron bunch. This suggests that longer and confined propagation of the laser pulse is essential for low divergence of the electron bunches. Fig.6.14 shows the typical behaviour of the electron bunch size versus length of the scattering region. These features were reproducible during the experiment and attributed to longer interaction time (or length) between the accelerated electrons and plasma waves. Apart from providing large acceleration gradient, the plasma waves can also cause focusing effect on the electron bunch.

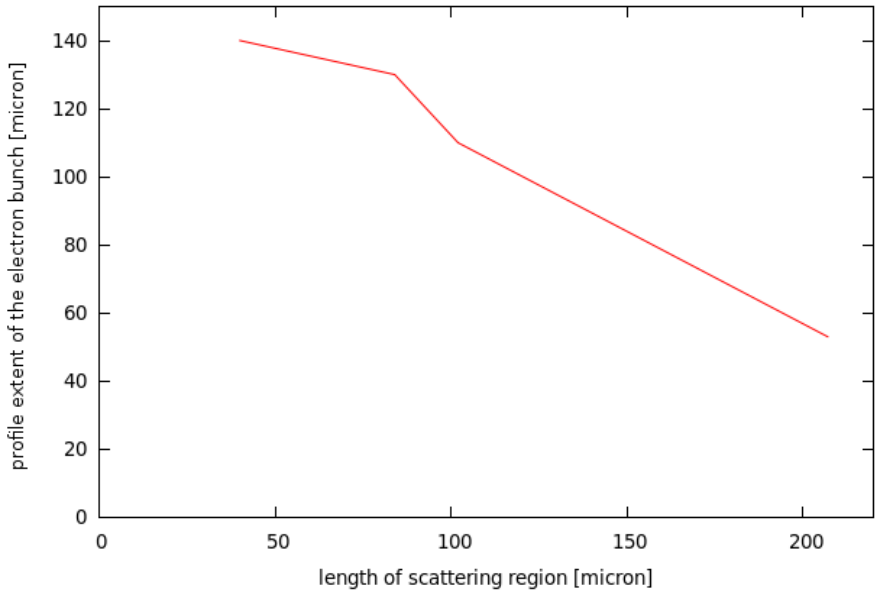

Figure 6.14: The typical trend of the electron bunch profile as a function of length of the scattering region, monitored by Thomson scattering diagnostic. Bunch divergence exhibits an inverse relation with the propagation length of the laser pulse.

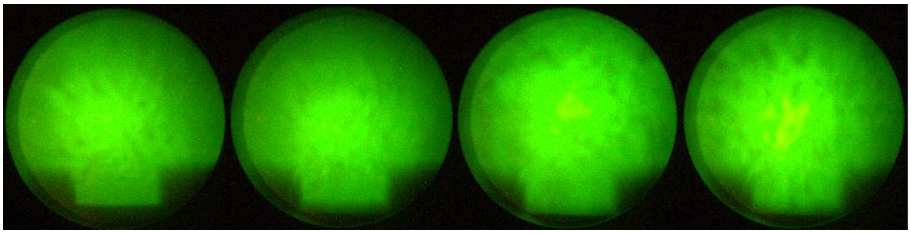

Figure 6.15: Electron signal on Lanex obtained from Nitrogen gas target.

Sometimes there is a hot-spot region observed along with the large diverging electron bunch (as seen in first case of figure 6.13(a)). Whereas, with nitrogen gas target most of the time large electron signal covering the whole Lanex screen was detected (cf. fig.6.15).

Figure 6.16 shows electron signal obtained during the experiment with helium gas target. Quasi-collimated bunch of electrons with moderate spread in energy of the bunch obtained with helium gas, indicating the possibility of generating quasi-monochromatic bunches of electrons with moderated power laser systems. Fig.6.17 shows the electron signal obtained with nitrogen gas target. Almost 100% energy spread has been recorded during most of the time with nitrogen gas target. Within our experimental conditions electron signals are detected only at high gas pressure $(\geq 30\mathrm{bar})$. The difference between the electron bunch

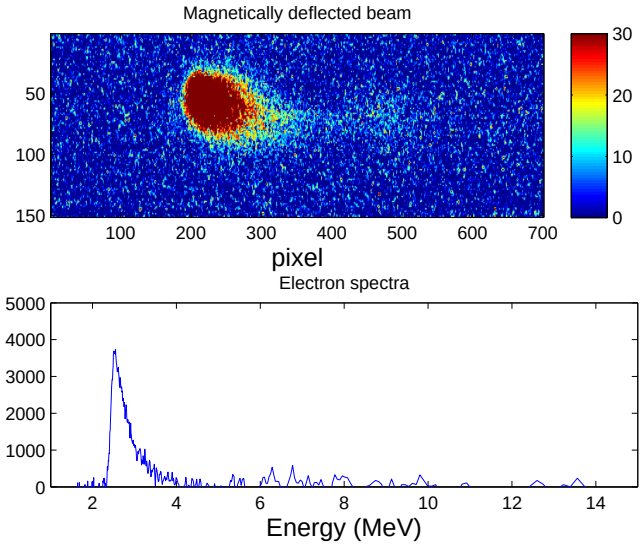

(a)

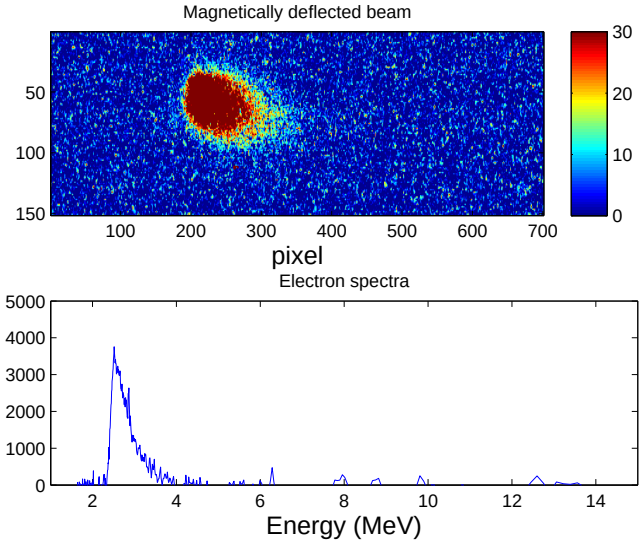

(b)

Figure 6.16: Energy spectrum of the electron bunch generated with Helium gas target. (a) Shot no.7084 (b) Shot no.7223. Quasi mono-energetic electron bunches are generated by optimizing the laser and gas jet parameters in case of Helium gas.

size in helium and nitrogen gas target can be attributed to their atomic structure and the way the laser pulse propagates in these targets.

One can notice that the intensity required to ionize helium gas completely is close to the intensity required to ionize nitrogen gas up to 5^{th} level. Moreover, nitrogen is a diatomic

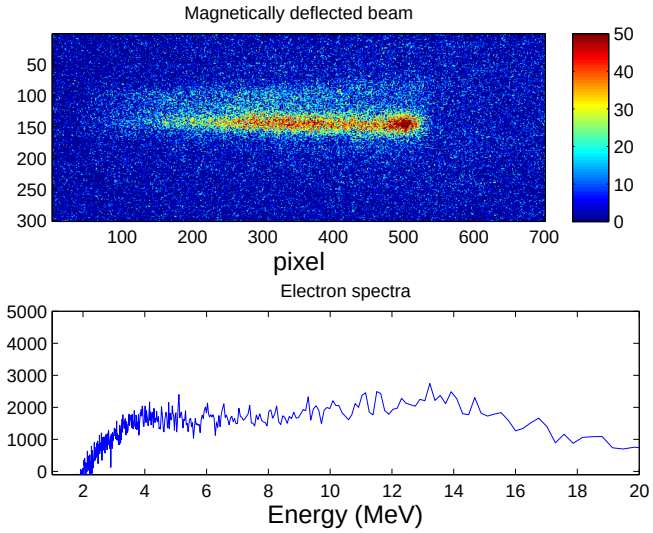

(a)

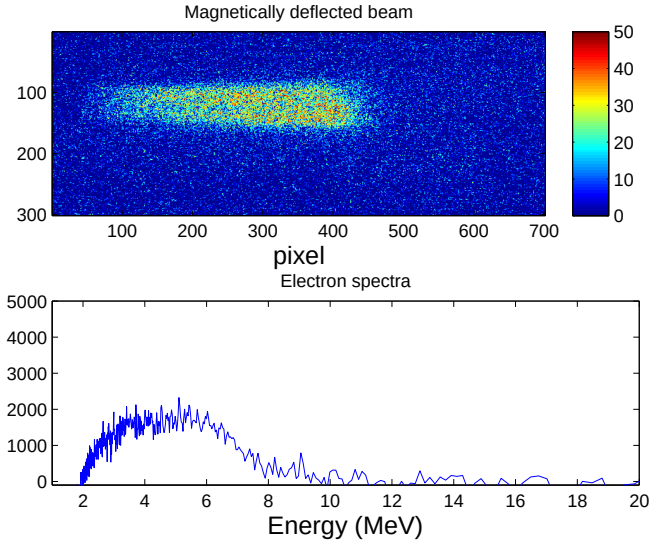

(b)

Figure 6.17: Energy spectrum of the electron bunch generated with Nitrogen gas target. (a) Shot no.9791 (b) Shot no.9804. The spectra shows large energy spread in electron bunches.

specie in nature. Thus, with nitrogen gas much large electron density can be obtained relative to helium gas. At this point it is essential to note that the wave-breaking condition, which is responsible for self-injection, is proportional to the square root of the electron density whereas, the acceleration length is in inverse proportion to electron density. It could be possible that due to low electron density, in case of helium gas target, the wave-breaking

condition is not achieved most of the time. This might be the reason for low reproducibility of electron signal with helium gas target. Difficulty in self-injection could also prevent in helium multiple injection of electrons in Wakefield. This could explain why a collimated electron bunch is generated with helium gas. However, low electron density provides large acceleration length. But diffraction effect dominates and the acceleration length remains equal to Rayleigh length. Thus, in our experimental conditions collimated but low energetic electron bunch is generated with helium gas target.

On the other hand, due to relatively large electron density, in case of nitrogen gas target, the wave-breaking condition could be satisfied quite often. This explains high reproducibility in electron signal with nitrogen gas target. In absence of any guiding mechanism the laser pulse diffracted and the process ends up with large diverging electron bunch generation. However, large electron density reduces the critical power required for self-focusing of the laser pulse. This might be the case with nitrogen gas target. This is also observed in simulations (discussed in chapter 7). This could explain relatively large electron energy from nitrogen gas target.

To summarize, experiments were performed with helium and nitrogen gas targets. It was observed that with helium gas more collimated electron bunches were produced but the reproducibility was poor. On the other hand, non-collimated electron bunches with large charge and good reproducibility were obtained with nitrogen gas. The maximum cut-off energy in case of helium and nitrogen gas target was 3 MeV and 20 MeV respectively.

6.6 Particle-In-Cell numerical simulation

The numerical study of the propagation of laser pulse in underdense plasmas and electron density evolution was performed with a relativistic Particle-In-Cell (PIC) code, PSC [111]. The PSC code is a three-dimensional cartesian code based on the Monte-Carlo-Particle-In-Cell (MCPIC) method. The code solves relativistic Vlasov-Boltzmann equations coupled to the Maxwell equations. The code starts with solving the Maxwell equations on each cell of the grid. The space charges and currents are obtained from the distribution and velocities of the quasi-particles [1]. The fields at the positions of the particles are obtained

[1] Plasma consists of a large number of particles. Computationally it is not possible to track individual particle in the simulation. Each quasi-particle represents collection of large number of real particles in the system. The charge to mass-ratio of the quasi-particle is similar to an individual particle.

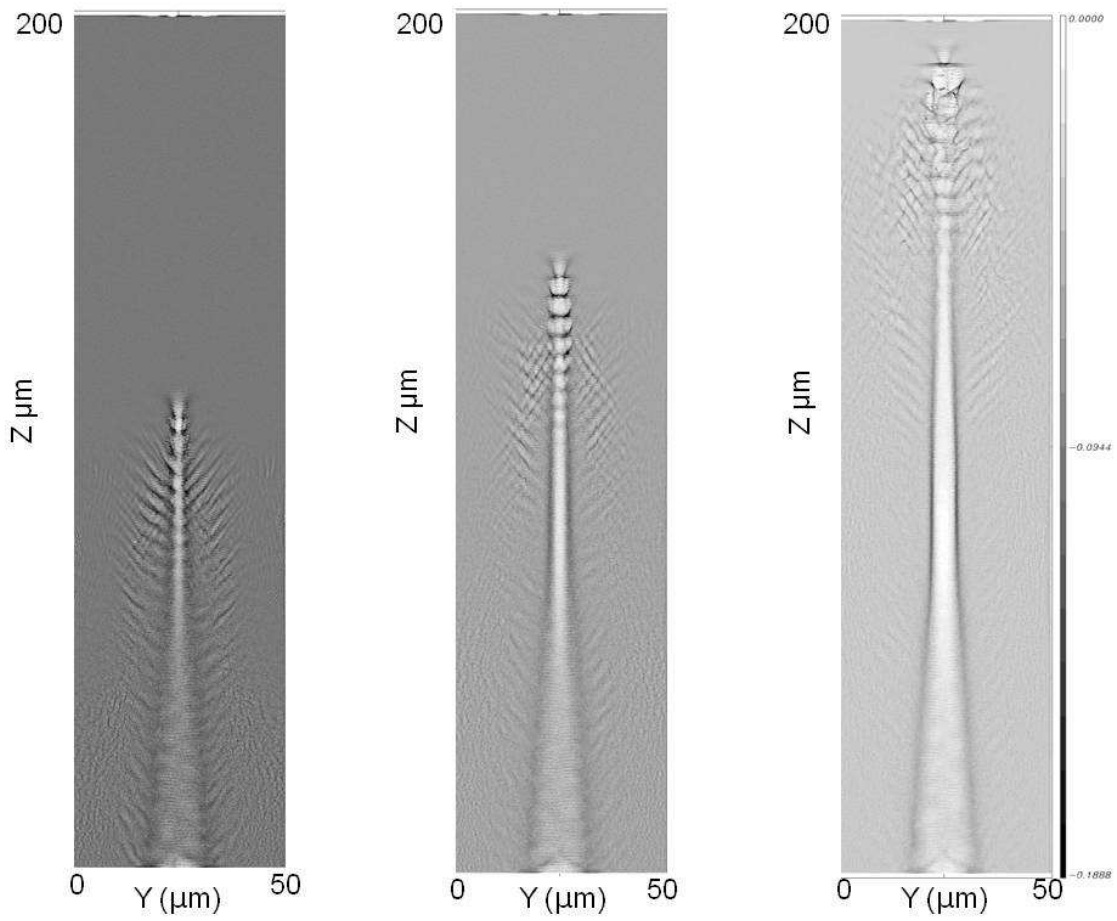

Figure 6.18: Electron density distribution in 2D. The laser is p-polarized and propagates along z-axis. A wake like structure is formed behind the laser pulse. The side bar represent the electron density normalised by critical density. These snapshots are recorded after 426 fs, 576 fs and 747 fs.

by interpolation. The new positions and velocities obtained after a time step dt are used to update the space charges and currents to be inserted in Maxwell's equation. In general, a collision-less plasma is assumed in a standard PIC-code, i.e. collective effects dominate over small-scale collisions. Binary collisions have to be included separately (if required). The time step of the iteration, however, has to be small enough to resolve the frequencies that occur in the problem (e.g. the external electric laser field and the electron plasma frequency). Also the spatial grid size has to be adapted to the problem accordingly to resolve typical scale length (such as the Debye length). We used the PSC code in 2-D geometry.

To simulate the pulse propagation, a simulation box of dimension $50\mu\mathrm{m} \times 200\mu\mathrm{m}$ was defined in y and z direction, respectively. The number of grid points kept along y axis are 500

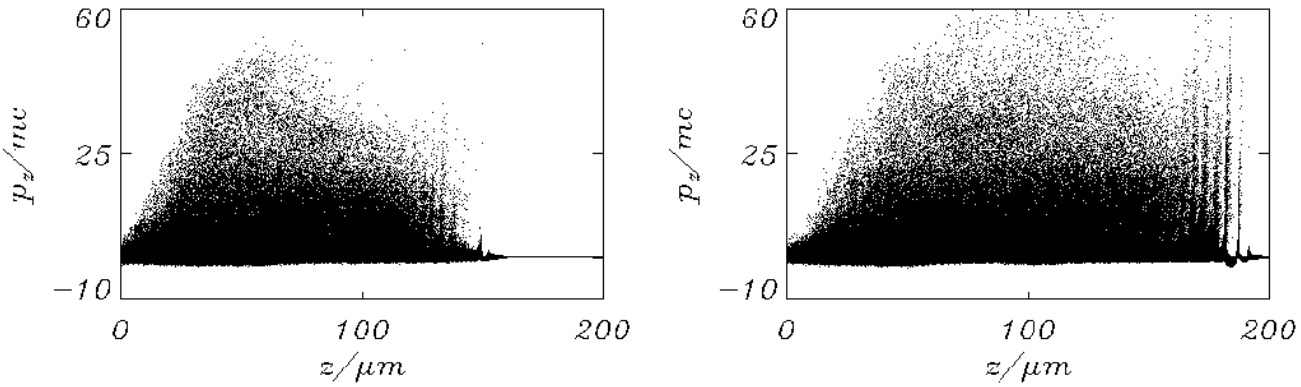

Figure 6.19: Phase Space of the electrons in 2D. The figure shows the zp_z-projections of the electron phase space. Strong plasma wave oscillations can be seen from the figures. There is no clear evidence of injection of the particles up to $200\mu m$.

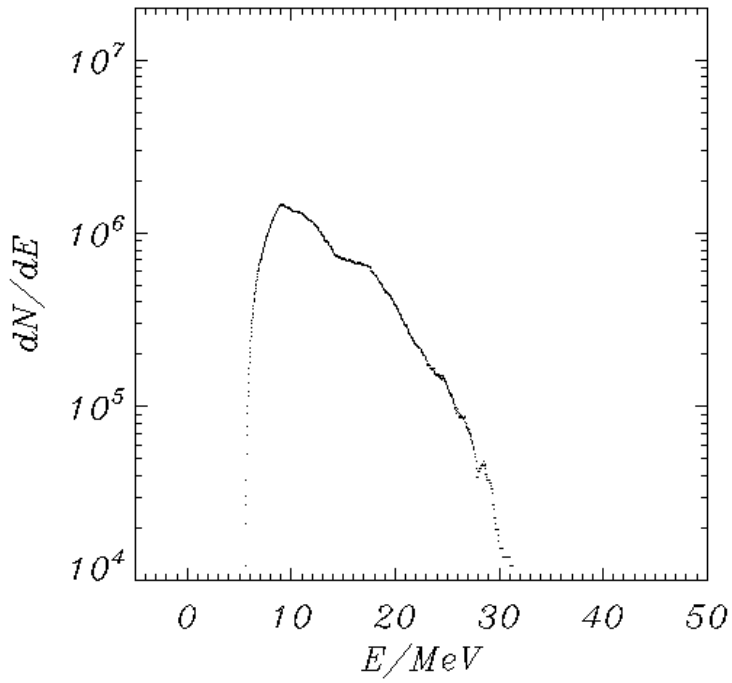

Figure 6.20: The energy spectrum of the electrons accelerated in the simulation.

and along z axis are 2000. This corresponds to 10 grid points per micron. The simulation was run with 25 particles per-cell. A P-polarized pulse was used in the simulation which propagates along z-axis and the electric field oscillations were along y-axis. The boundary conditions for the particle and fields are either periodic or reflecting ones. The simulation

box was uniformly filled with pre-formed plasma with a peak density of $5 \times 10^{19}\mathrm{cm}^{-3}$. The simulation was run on a single computer having a quad-core Intel processor with 8 GB of RAM. Due to the limited configuration of the computer the run time of the simulation was one week. Figure 6.18 shows the electron density evolution as the pulse propagates in a pre-formed underdense plasma. A cavity like structure develops behind the pulse as it propagates around $100\mu\mathrm{m}$. This is the signature of wakefield excitation by the laser pulse. As the pulse propagates further, the wakefield or cavity like structure is more clear. Due to lack of absorbing boundary conditions in the code some reflection can be seen from the side walls at the end of the simulation. This affects the visualization of the snap shots. Figure 6.19 shows the phase-space plot of the electrons ($\mathrm{zp_z}$ projection) . Up to the $200\mu\mathrm{m}$ propagation length there is no exact indication of generation of collimated electron bunches. However, plasma wave excitation and wakefield generation is clear from simulation. Figure 6.20 shows the electron energy spectrum obtained from the simulation. This is similar to the energy spectrum obtained from nitrogen gas target. The simulation evidences the generation of Maxwellian electrons in our case. This is also seen in experiments with nitrogen gas target.

6.7 Conclusion

During the first phase of the experiment carried out with moderate power laser system at Pisa laboratory, suitable conditions for electron acceleration have been found. Quasi collimated electron bunches with few MeV energy was observed with Helium gas target, while thermal electrons with energy exceeding 15 MeV was observed with Nitrogen gas target. Numerical simulation supports wakefield excitation behind the laser pulse which can be capable of accelerating electrons up to few MeV energy in a length of few microns. These kind of electron bunches are suitable for a small all-optical laser-driven accelerator able to efficiently generate γ-rays (via bremsstrahlung). Within this limit, most of the requirements on the electron bunches, like mono-chromaticity, small divergence etc., are required at a moderate level [112]. The laser system at Pisa laboratory is under up-grading to have more shorter pulse length of around 40 fs with energy content of approximately 120 mJ at the focused spot. The next phase of the electron acceleration experiment, including the γ-ray source generation and biomedical application, with the upgraded system at ILIL laboratory is expected to start in the near future.

CHAPTER 7

Frequency up-shift and super-continuum generation in laser-plasma interaction

7.1 Outline

Frequency shift is one of the most important phenomena in laser-plasma interaction studies as it reflects the coupling process of the electromagnetic waves in plasmas. The incident electromagnetic wave can couple in the plasma with an electron plasma / ion-acoustic wave so producing scattered electromagnetic waves or two plasmon decay process [As described in previous chapters]. These phenomena are relevant to laser fusion applications, since they can either decrease the amount of energy absorbed by the pellet or reduce the implosion symmetry [113]. Generally, when one of these instabilities occurs, the electromagnetic frequency down-shift can be observed because the laser gives part of its energy to the plasma waves [114]. However, frequency up-shift has also been observed in the laser-plasma interaction [115, 116]. Since the frequency up-shift phenomena have the potential to develop compact tunable radiation sources based on laser plasma interaction, a growing interest is emerging in this field.

In this chapter we will discuss the propagation of the laser pulses in neutral gas medium and the effect of plasma formation on the laser pulse *frequency up-shift*. An introduction to the basic principle of frequency up-shift process is given in Section 7.2. In Section 7.3 experimental results on frequency up-shift are presented. Section 7.4 is concerned with the propagation of the laser pulse in different atomic species. Finally, in Section 7.5 a possible physical mechanism behind the observed frequency up-shift process is discussed.

7.2 Frequency shift: An introduction

An electromagnetic wave propagating from a medium to another medium experiences change in its wave vector because the properties of the medium varies in space. This variation gives rise to refraction phenomena of the light when it crosses the boundary between the two media. Similarly, when an electromagnetic wave propagates in a medium whose properties changes very fast with time it experiences change in its frequency components. This later phenomena is known as frequency shift of the incident light pulse [117] and in optical physics is more popularly known as ***supercontinuum generation***. The supercontinuum is the generation of white light pulses spanning from the ultraviolet to the near infrared that arises from the nonlinear interaction and propagation of ultrafast pulses focused in a material. The supercontinuum can be generated in different states of matter - condensed media (solids and liquids) and gases.

In principle, various processes are involved in supercontinuum generation. A fundamental role in this phenomena is played by ionization of the medium. When an intense ultrashort laser pulse propagates through a medium, it changes the refractive index from the distortion of the atomic or molecular neutral configuration, which in turn changes the phase and amplitude of the incident pulse [118]. The phase and amplitude change can cause a frequency sweep of the incident pulse and can alter the envelope and spatial profile (self-focusing) of the pulse. Thus, the self-phase modulation is the fundamental physical mechanism responsible for the spectral and spatial modification of the incident laser pulses in plasmas.

The main physical parameter responsible for the SPM is the intensity and the shortness of the laser pulse. The spatial variation of laser intensity leads to SPM in space. Since a laser beam has a finite cross section, and hence a transverse intensity profile, SPM on the beam should have a transverse spatial dependence, equivalent to a distortion of the wave front. Consequently, SPM in space is responsible for focusing or defocusing of the laser pulse. In the case of a pulsed laser input, the temporal variation of the laser intensity leads to an SPM in time. Since the time derivative of the phase of a wave is simply the angular frequency of the wave $[\omega(\mathrm{t}) = -\partial(\phi)/\partial \mathrm{t}]$ [1], SPM also appears as a frequency modulation. Thus, the output beam appears with a self-induced spectral broadening. For large spectral broadening, a strong SPM in time is required, i.e., a large time derivative in the phase change.

[1] $\phi = kx - \omega_0 t$ and $k = k_0\eta$ where k_0 and ω_0 are wave vector and angular frequency in vacuum, respectively and η is the refractive index of the medium. Thus, $\omega = -\frac{\partial\phi}{\partial t}$=-$[k_0 x\frac{\partial\eta}{\partial t} - \omega_0]$. This implies $\omega - \omega_0 = k_0 x\frac{\partial\eta}{\partial t}$.

In intense laser-matter interaction, a change in the refractive index is induced by ionization of the neutral medium. Ionization gives rise to phase modulation of the incident laser pulse and hence new frequency component generation. An electromagnetic wave propagating in a neutral gas medium ionizes the medium and forms a plasma. The refractive index of the plasma is given as

$$\eta = \sqrt{1 - \frac{\omega_p^2(t)}{\omega^2}} \tag{7.1}$$

where, ω_p is plasma frequency and ω is the laser frequency. Thus, during the transition from the gas to the plasma state, the electromagnetic wave experiences reduction of the refractive index. In this way a negative time derivative of the refractive index produces up-shift of the laser frequency. At high intensities ($\geq 10^{18}\mathrm{Wcm}^{-2}$) the relativistic effects become significant and the plasma refractive index formula modifies to

$$\eta = \sqrt{1 - \frac{\omega_p^2(t)}{\gamma\omega^2}} \tag{7.2}$$

Thus, along with the fast evolution of electron density due to ionization, relativistic correction in electron mass also modifies the refractive index in case of relativistic laser-plasma interaction.

For a laser pulse of Gaussian intensity profile, ionization results in an uneven distribution of electron density, maximum along the axis and gradually decreasing along the transverse direction of the pulse propagation. This produces a refractive index minimum along the axis and maximum along the wings of the laser pulse. Consequently, the ionized medium behaves like a diverging lens, causing defocusing of the laser pulse. However, if defocusing effects can be circumvented by some non-linear focusing effects the laser pulse can propagate for longer distances partially compensating the defocusing action of the diffraction. The electron density evolution at any time, t, depends on the intensity of the laser pulse at preceding times at that position. Thus, the rate of defocusing is stronger at the trailing portion of the pulse. The relativistic mass non-linearity, in contrast, is local in time and producing an increase of the refractive index induces the self-focusing of the laser pulse. For a fast rising laser pulse, as the refractive index changes rapidly with time, the phase of the laser is modulated causing shifting of the frequency of the laser pulse.

Inoization induced spectral blue-shift has been widely investigated experimentally [119, 120, 121, 122], theoretically [123, 124, 125, 126, 127, 128] and numerically [129, 130, 131]. However, a number of competitive effects, including intensity decrease due to either

defocusing or energy depletion of the laser pulse, have limited so far the observed blue shift to a few tens of nanometers [132, 133]. Apart from ionization induced frequency up-shift there are other physical mechanisms, like frequency shift by plasma wakefield (commonly known as photon acceleration by plasma wakefield) [134, 135], which may also contribute to the frequency up-conversion during laser plasma interaction. For wakefield induced photon acceleration, the required condition is that the spatial extent of the laser pulse should be shorter than the plasma wavelength. So that the pulse can be trapped by the accelerating structure of the plasma wave in a similar way as it trapped electrons in the case of wakefield acceleration. The most dominant mechanism depends on the physical conditions of the experiment and strongly related with the atomic specie properties as well.

7.3 Experimental results on frequency up-shift

Laser pulse propagation in plasmas and its spectral modification have been extensively studied in last three decades. Usually the spectral analysis of the transmitted laser pulse was performed by sending it into a spectrometer. This provides space and time integrated information on the transmitted pulse spectrum. Important information regarding laser-matter interaction is encoded in the pulse spectrum, without any time resolution when the laser pulse lasts only a few tens of femtoseconds.

In the experiment [2] we tried to understand how the spectral envelope of the pulse changes during its interaction and propagation through the gaseous medium. For this purpose, Thomson scattered light was used as a diagnostic. The Thomson scattering (TS) diagnostic is generally used to monitor the propagation of the laser pulse. We used also a spectrometer to analyse TS radiation. The detection range of the spectrometer was from 200 to 850 nm. An unprecedented broadening of the incident laser pulse towards the blue region, exceeding 300 nm in wavelength, has been recorded. The images of the propagation region displayed multi-coloured light generation during interaction and propagation of the laser pulse through gaseous medium. Figure 7.1 shows the Thomson scattering image and the corresponding spectrum obtained in the case of nitrogen gas target. The noteworthy features in the Thomson scattering image are the structured periodicity of the emitted region, progressive frequency shift and guiding of the laser pulse. Similarly, the notable features in the corresponding spectrum are the extent and behaviour of frequency shift. The up-shift in

[2] The experiment was carried out with the laser system described in chapter 6.

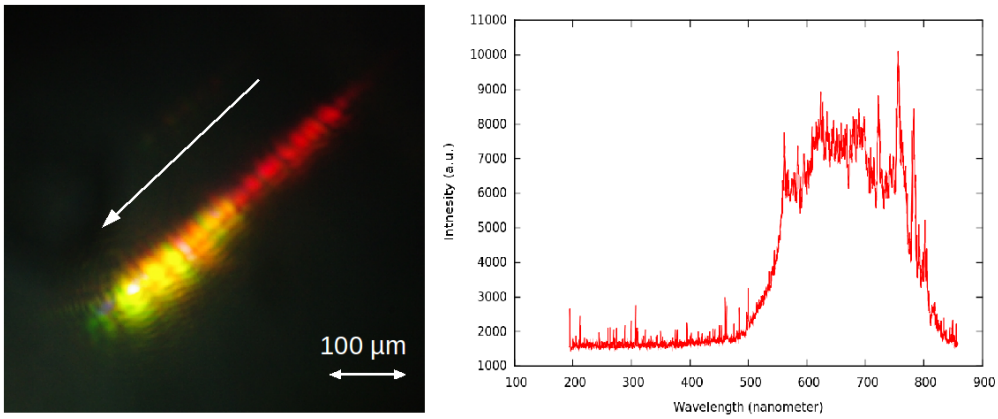

Figure 7.1: (a) Thomson scattering image and (b) the corresponding spectrum obtained during the experiment With nitrogen gas target. The arrow in the figure indicates the direction of propagation of the laser pulse.

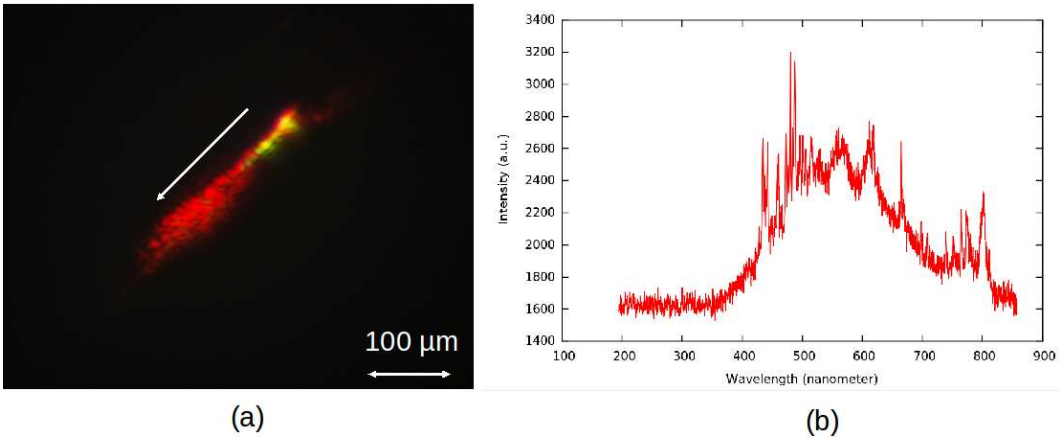

Figure 7.2: (a) Thomson scattering image and (b) the corresponding spectrum obtained during the experiment with argon gas target. The arrow in the figure indicates the direction of propagation of the laser pulse.

frequency is almost continuous from the fundamental 800 nm to 550 nm wavelength. No filter has been used during the recording of these images and spectra. As far as we know, such variations in the frequency of the incident laser pulse during the interaction with gas targets has been never reported before in literature. These observations can stimulate future research on understanding the physics behind the propagation and intensity evolution of the laser pulse.

These observations of supercontinuum generation from gas targets are encouraging re-

sults for *tunable frequency radiation sources*. Since ionization induced frequency shift strictly depends on the electron density and its evolution with time, tunability of radiation could be achieved by varying the electron density and pulse duration of the laser pulse. However, during the experiment it was observed that some effect on extent of frequency shift can be obtained by using different gas targets. With argon gas, the extent of frequency up-shift was large in comparison to the shift observed with nitrogen gas. Figure 7.2 shows the Thomson scattering images and its corresponding spectrum obtained from argon gas. The Thomson images from argon gas target exhibits the similar behaviour of spatially progressive up-shift in frequency. The spectrum of the scattered radiation also displayed the similar large up-shift in frequency.

One can notice different features in Thomson emission for the two gases:

1. The change of frequency occurs in the later part of the propagation in case of nitrogen gas target, whereas, the change of frequency occurs at the initial part of the propagation in case of argon gas target.

2. The scattered radiation from nitrogen gas is intense and bright (especially the region of frequency up-shift), whereas, the scattered radiation from argon gas is weak in intensity.

3. In the case of nitrogen gas the shift is almost continuous and starts from 800 nm wavelength, whereas, in case of argon gas the fundamental 800 nm wavelength is clearly distinguished and visible separately from rest of the shifted spectrum. There is an initial dip in the frequency shifted spectrum around 750 nm and then the frequency shift is progressive up to 450 nm.

4. The extent of up-shift is larger in case of argon gas as compared to the nitrogen gas target.

This different features of the Thomson emission for the two gases could be due to their different atomic structure which produces different behaviour of the ionization dynamics.

The physical explanation of such a large frequency up-shift requires a complete wave-propagation model taking into account ionization of the medium. Following Rae et al. [131], for a homogeneous plasma and an electron density much less than the critical density, the time dependent spectral shift from plasma formation can be roughly estimated as

$$\Delta\lambda = -\frac{e^2 N_0 L \lambda_0^3}{8\pi^2 \epsilon_0 m_e c^3} \frac{dZ}{dt} \tag{7.3}$$

where e is the electronic charge, N_0 is the atom density, Z is the degree of ionization, λ_0 is the fundamental laser wavelength, L is the interaction length, m_e is the electron mass and c is the velocity of light in vacuum. $\frac{dZ}{dt}$ strongly depends on laser intensity and on the time needed to ionize a considerable fraction of neutral atoms. According to this formula, large frequency shift can be obtained either by increasing the interaction length (L) or the electron density. To achieve high intensity normally tight focusing optics is used in experiments, this limits the interaction length due to diffraction effects. Also, the spatial variation of the refractive index of the plasma due to ionization further limits the interaction length by defocusing the laser beam. Using equation 7.3, for a fundamental wavelength of 800 nm, an interaction length of $200\mu\mathrm{m}$, electron density of $2.5 \times 10^{19}\mathrm{cm}^{-3}$, maximum ionization state of 5 (for nitrogen gas) and ionization time of 60 fs, the shift in the wavelength is found to be $\approx 320\mathrm{nm}$, which is in fair agreement with the shift observed experimentally in case of nitrogen gas. For an electron density of $4 \times 10^{19}\mathrm{cm}^{-3}$ and maximum ionization state of 8 (for argon gas) in 80 fs [3], the shift is $\approx 300\mathrm{nm}$, which is around 100 nm less than the shift recorded experimentally in case of argon gas. Nevertheless, above formula gives a rough estimation of the frequency up-shift.

For the Thomson scattering radiations we rely on scattering centres (plasma electron), which scatter incident laser light in different directions. In this way we have a two step process: (1) interaction of light with gaseous medium and its ionization, and (2) scattering of the incident laser pulse by ionized electrons. Moreover, as the images and spectrum are recorded at 90^0 to the laser propagation direction, the contribution of Doppler shift can not be ruled out in frequency up-shifting process. Thus, we believe that **a physical model that includes the ionization process and Thomson scattering configuration can give an actual estimation of the frequency shift that can take place during the interaction process**.

The exact reason for such a huge up-shift in frequency can be due to many non-linear physical processes and phenomena involved during laser gas interaction. In the next section, we will try to give some physical reasons behind the observed frequency up-shift by analysing the propagation of the laser pulse in nitrogen and argon gas medium.

[3] The different time scales for degree of ionization in case of nitrogen and argon gas is due to the fact that the rate of ionization depends on both, the laser and the atomic specie properties.

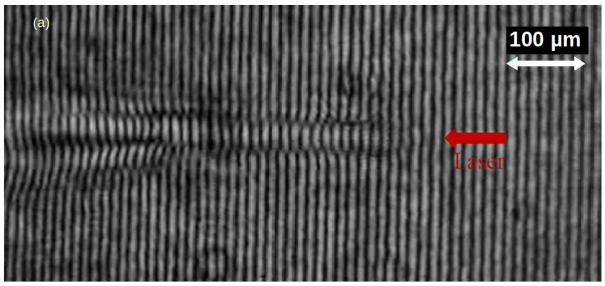

Figure 7.3: Interferogram obtained in case of Nitrogen gas at 35 bar. The interferogram is taken at $\geq$ 5ps after the arrival of the main laser pulse. The interferogram shows a collimated propagation of the laser pulse over few hundreds μm indicating a competitive process against optical diffraction. Arrow in the figure indicates the direction of laser pulse propagation.

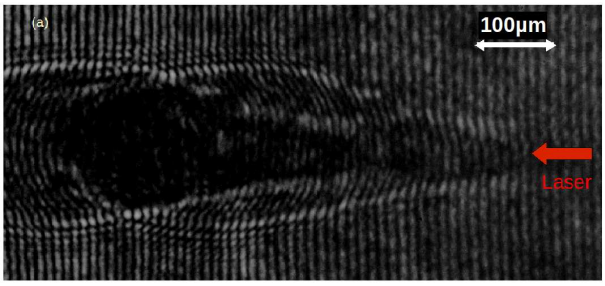

Figure 7.4: Interferogram obtained in case of Argon gas at 35 bar. The interferogram is taken at $\geq$ 5ps after the arrival of main laser pulse. The interferogram shows the diffraction of the laser pulse. Arrow in the figure indicates the direction of laser pulse propagation.

7.4 Propagation of laser pulse in different gases

Interaction of laser pulses with gaseous medium initiates with the ionization process. For a Gaussian laser pulse the ionization process produces an electron density maximum at the center and minimum towards the wings of the pulse. This uneven distribution of the electron density behaves as a diverging lens and tends to defocus the pulse. This is known as ionization induced defocusing. For a modest intensity pulse, ionization induced defocusing potentially affects the propagation of the laser pulse. This is the reason why most of the early experiments were done with low atomic number gases, usually hydrogen and helium. However, there are atomic species in which the ionization potentials of the successive ionization states needs very high intensities. Nitrogen is very attractive atomic species from this point of view. The first five ionization states for nitrogen gas need almost same intensity as that required to fully ionize helium gas. But the remaining 2 states $(6^{th}$

and7^{th}) need very high intensity (more than three orders in magnitude compared to lower ionization states). Another advantage with nitrogen gas is its diatomic nature. Consequently, for same intensity nitrogen gas will produce larger electron density than hydrogen or helium gases. For a short pulse $(< 100fs)$ this ionization state can be attained in very early time of interaction. If the intensity of the pulse is well below the 6^{th} and7^{th} ionization threshold of nitrogen, no further ionization will take place (until self-focusing effect increases the intensity of the pulse required to ionize 6^{th} and7^{th} levels) and the ionization will be quasi-saturated in the early time of interaction. In such a case, most part of the pulse propagates as if it is propagating through a pre-formed plasma. Consequently, the pulse will be least affected by ionization induced refractive defocusing and a stable condition for the pulse propagation could be reached.

We studied this phenomena experimentally with the 2 TW laser pulses. The results show a quasi stable propagation of the pulse with nitrogen gas as a target. Time resolved interferometry and Thomson scattering images provided a useful support to gain information about the pulse propagation. Figure 7.3 shows an interferogram recorded using nitrogen gas target. It is observed that the laser pulse propagates without any early diffraction, maintaining its radial extent and a long channel-like longitudinal propagation. The laser pulse envelope was quasi Gaussian. The Rayleigh length of the pulse was around $60\mu\mathrm{m}$. However, the length of the scattering region is greater than $300\mu\mathrm{m}$, which is more than five times the Rayleigh length. A bright scattered region maintained over propagation length was also seen in the Thomson scattered image recorded in case of nitrogen gas (cf. fig.7.1). Figure 7.4 shows an interferogram recorded using argon gas target. Unlike the case of nitrogen gas, divergence of the pulse is clearly apparent from interferogram. A gradual decrease in the intensity of the scattered radiation with the propagation of the pulse can also be seen in the Thomson image (cf. fig.7.2). These behaviours of laser pulse propagation in these two different gases were reproducible during the experiment.

As the light emitted from Thomson scattering is the product of local laser intensity and electron density it gives a combined information on laser intensity and electron density evolution during the propagation of the pulse. Electron density evolution can be estimated with optical interferometry and thus, Thomson scattering may give some information about intensity evolution of the laser pulse. Such a method to characterize the ultraintense and ultrashort laser fields and to study the ultrafast dynamics of the electrons was proposed by Gao [136, 137]. In the present work, the propagation issue of the laser pulse in nitrogen and

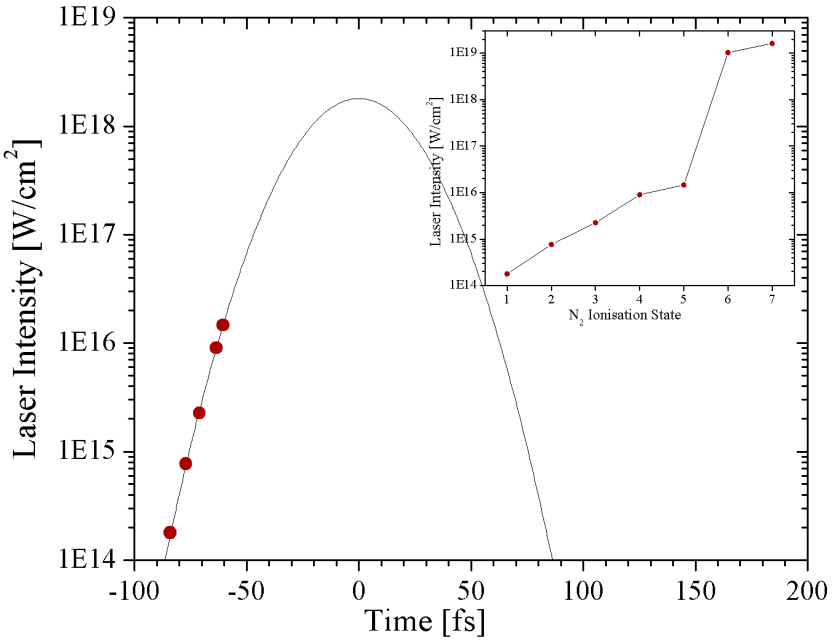

(a)

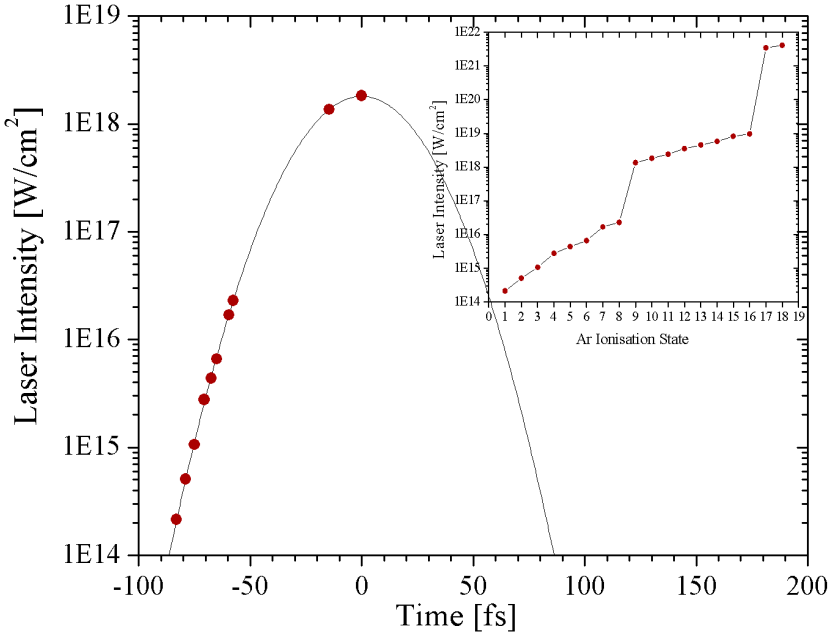

(b)

Figure 7.5: (a) Represents the temporal intensity profile of the laser pulse. Red dots on the curve represent different ionization levels for N_2 gas. Inset: Intensity vs ionization state for N_2 gas. (b) Represents the temporal intensity profile of the laser pulse. Red dots on the curve represent different ionization levels for Ar gas. Inset: Intensity vs ionization state for Ar gas.

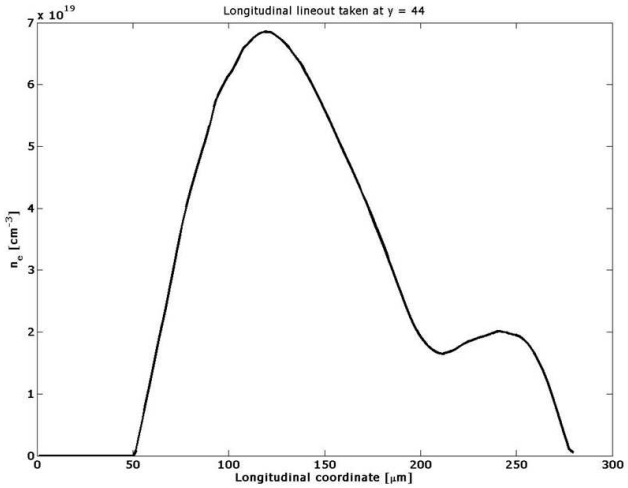

Figure 7.6: Electron density evolution obtained from interferogram in case of nitrogen gas.

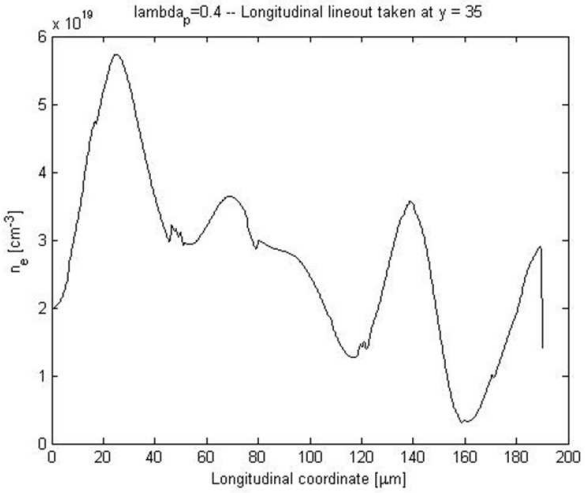

Figure 7.7: Electron density evolution obtained from interferogram in case of argon gas. Due to not good quality of interferogram and overlapping of the two images in Nomarsky interferometery, analysis of the interferogram is quantitative.

argon gases has been studied.

The different behaviours in the propagation of the laser pulses in these two gases can be understood from their ionization potentials. Figures 7.5(a) and 7.5(b) illustrate the temporal profile of the laser pulse and ionization threshold [4] [inset] for nitrogen and argon gases,

[4]The intensity required to ionize an atomic specie up to n^{th} state can be obtained from equation 5.10 in

respectively. At the intensity and time scale of the currently available CPA laser pulses, the laser pulse can fully or partially ionize the gas in a time shorter than a single wave period. During the ionization process, the transverse electron density distribution could defocus the laser pulse. However, if the critical power threshold could be reached the pulse could undergo self-focusing. Moreover, at intensities $\geq 10^{18}\mathrm{Wcm}^{-2}$ relativistic effects become significant, which modulates the refractive index of the plasma in a way exactly opposite to ionization process and causes the laser pulse to focus.

It is apparent from figure 7.5(a) that in the case of nitrogen gas the rising edge of the laser pulse ionizes the medium up to the 5^{th} level in the early time of interaction and most of the pulse propagates without further ionization. Within the intensity level of the focused pulse, during their interaction with laser electric field, the ionized electrons could acquire relativistic quiver velocity, and give rise to an increasing γ factor in eq.(7.2). In this condition, a competition between optical diffraction and relativistic self-focusing takes place and leads to a collimated propagation of the laser beam. This process becomes weak when the laser energy depletes significantly or when non-linear effects saturate. Instead, if the pulse peak intensity is comparable to the value suitable for partial ionization of the gas, as shown in figure 7.5(b), ionization severely affects the pulse propagation. The laser pulse energy was mainly exhausted in ionizing the neutral gas medium and might not have reached a condition suitable for relativistic self-focusing. In such a case, ionization induced refractive effects remained strong enough to defocus the pulse and resulted in an unstable propagation.

The above argument is also supported by deconvolution of electron density from interferograms, which shows similar plasma density in both the gases. In spite of this fact, a quasi-stable propagation was observed in nitrogen gas, while, defocussing effects remained dominant in argon gas. Figures 7.6 and 7.7 show the electron density distribution obtained from the interferogram recorded in the case of nitrogen and argon gases, respectively. Due to poor quality and overlapping of the two images in the interferogram, analysis was a little difficult and qualitative. In the next section we will try to explain the frequency up-shift phenomena with the help of pulse propagation behaviour in the two gases.

chapter 5.

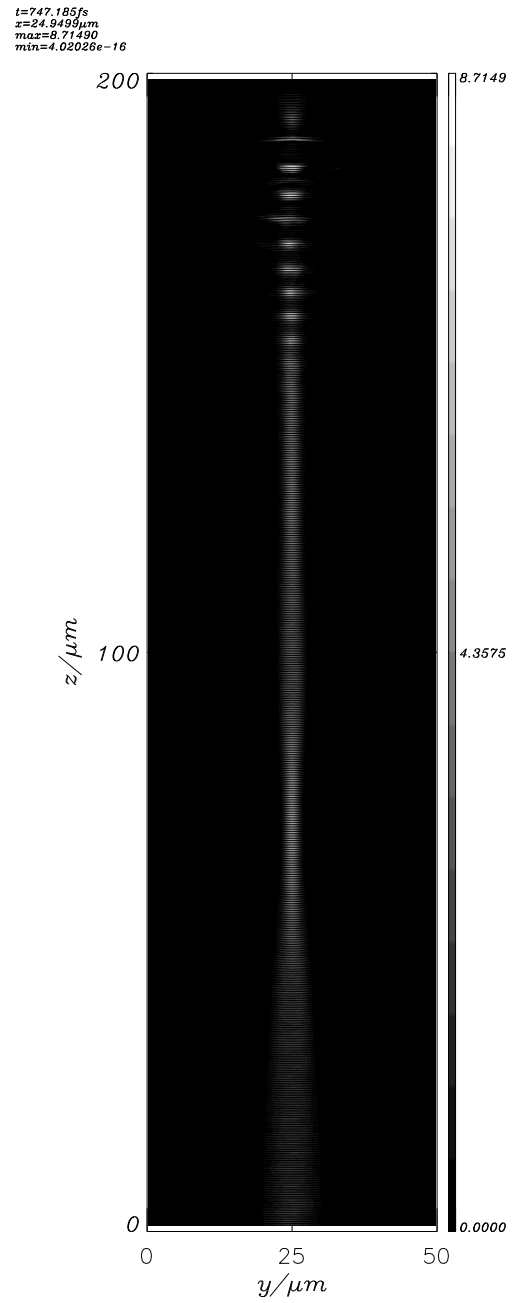

Figure 7.8: Numerical calculation of laser pulse propagation in underdense plasmas. The figure shows the intensity evolution of the laser pulse propagating in pre-formed plasma. The sidebar represents the normalised intensity values.

7.5 Discussion and explanation for frequency up-shift process

In the case of nitrogen gas it is evident from Fig. 7.5(a) that the incident laser pulse ionizes the medium up to 5^{th} state in very early time of interaction. The remaining part of the laser pulse propagates as it is propagating through a pre-ionized plasma. Under such conditions the pulse received minimum return effect from ionized electrons in terms of refraction process. This can be seen from the interferogram and Thomson scattering image from nitrogen gas. This implies that after the initial interaction, the energy content of the pulse is decreased only marginally. There after, in the case there is no self-focusing of the laser pulse takes place, the pulse should propagate smoothly up to the Rayleigh length and later on follow optical diffraction. In contrast, the interferogram recorded in case of nitrogen gas target displayed a completely different behaviour. The pulse propagates up to several hundred microns without any optical or ionization induced diffraction, suggesting self-trapping of the laser pulse. The critical power required to reach the self-focusing threshold is given as

$$P_c = 17 \left(\frac{n_c}{n_e} \right) GW \tag{7.4}$$

where, n_c is the critical density and n_e is the local electron density. Thus, the higher the electron density the lower will be the power required for self-trapping of the laser pulse. The electron density measured from interferogram (taken for nitrogen gas target) was in the range $2 - 7 \times 10^{19} \mathrm{cm}^{-3}$. Thus, the critical power required for self focusing of the laser pulse in our case is $1.44 - 0.41$TW, which is lower than the power (2 TW) available with our laser system. Hence, one can expect the self-focusing of the laser pulse during its propagation in nitrogen gas target. Due to self-focusing the local intensity of the light increases and will further enhance the efficiency of self-focusing phenomena. Due to self-focusing the pulse intensity increases up to a level where 6^{th} and even 7^{th} ionization states of nitrogen could be reached. The further ionization induces self-phase-modulation of the laser pulse and hence, frequency up-shift. The frequency up-shift process produces the energy depletion of the laser pulse so affecting the self-focusing phenomena. In addition to this, further increment of electron density on the path of laser pulse makes it difficult for the pulse to maintain its stable propagation. This physical behaviour is displayed by the Thomson scattering image in case of nitrogen gas.

However, as we have seen from figure 7.5(b), in case of argon gas ionization process

remain effective through-out the pulse envelope. ***Unlike nitrogen, there is no intermediate partial saturation of ionization process in case of argon gas***. The propagating pulse keeps on delivering its energy in ionizing the medium and as a result brisk ionization takes place during the early part of propagation. The ionized electron density is strong enough to modulate the laser phase and cause frequency up-shift. Besides ionization, laser pulse starts loosing its energy due to frequency up-shift process also. The gradually decreasing energy (due to ionization and frequency up-shift) and continuously increasing electron density makes difficult for the laser pulse to continue its propagation in the highly dense medium. The pulse soon loses all its energy and gradually become invisible before it could find a proper condition to maintain its propagation. This physical behaviour is again very well displayed by the Thomson images in argon gas target.

The propagation of the laser pulse in the underdense plasma is analysed numerically with PSC code. The code assumes fully ionized medium. The pre-plasma assumption was partially valid for nitrogen gas where rapid ionization took place in the early stage of its interaction with laser pulse. The pre-plasma density was set close to the maximum electron density that could be reached with nitrogen gas. Figure 7.8 shows the pulse propagation through the pre-formed underdense plasma. The code reproduced similar features as seen in the Thomson image obtained from nitrogen gas. As the pulse propagates, its transverse extent decreases indicating self-focusing of the pulse. Thus, intensity of the pulse increases as it propagates through the plasma. As the pulse propagates further, the intensity distribution shows oscillating behaviour. This may be due to an interplay or competition between non-linear focusing effects and defocusing effects. The oscillating focusing can be correlated with the quasi-periodic structure present in the Thomson images. Thus, simulations supports the self-focusing of the laser pulse under our experimental conditions. The absence of any such focusing behaviour of laser pulse in case of argon gas implied that ionization induced defocussing effect prevented the stable propagation of the pulse.

Regarding to the assumption of pre-formed plasma in the code, the effect of ionization on intensity distribution during propagation of the pulse was not considered. However, it was obvious that when pulse was involved in ionizing the medium, energy depletion would become more significant. This might prevent the pulse to reach the critical power threshold for self-focusing. In addition, the continuous ionization of the medium, as in the case of argon gas, would further affect the spot size of the pulse due to refraction induced defocussing. In such a case, both power and intensity might significantly be reduced and would

result in non-stable propagation of the laser pulse.

7.6 Conclusion

In this chapter we discussed the frequency up-shift phenomena observed during the laser gas interaction. Preliminary study on propagation of the laser pulse and Thomson scattering images suggest that the spectrum may be shifted due to ionization induced self-phase modulation of the laser pulse. Supercontinuum generation was observed from nitrogen and argon gases and found to be strictly related with the properties of the atomic species. High electron density target are essential for producing such effects. Another important observation was made on stable propagation of laser pulses with nitrogen gas target. Due to its unique atomic properties and diatomic nature nitrogen is emerging as an attractive target to be used for different application based on laser matter interaction. Numerical study of the propagation of the laser pulse was done with Particle-In-Cell code. Pre-plasma assumption prevented in our case to simulate the effect of ionization on intensity distribution during propagation of the pulse. However, it still provides some insight of the physical mechanism. It may be quite possible that in addition to ionization induced self-phase modulation, some other mechanisms responsible for such a huge frequency up-shift are also involved.

Part V

Experimental description and discussion: Part II

CHAPTER 8

Self-injection test experiment with sub-PW FLAME laser facility

8.1 Outline

The table-top terawatt laser systems has revolutionized the field of laser plasma interaction studies. These paves path for the development of high power laser systems that can be built at small scale laboratories and results in exponential growth in laser matter interaction studies. Particle acceleration, X-ray generation, inertial confinement fusion and many other strategic experiments have reached a new milestone. However, many challenges and constraints are due to the requirement of high power and intensities needed to practically realise these novel scientific applications.

This chapter is concerned with the experiment on electrons acceleration with a sub-petawatt laser facility at National Laboratory of Frascati. This experiment is an advance phase of the pilot experiment discussed in chapter 6. In Section 8.2 basic specification of the newly built FLAME laser system are described. In Section 8.3 the configuration and first experimental results on self-injection test experiment (SITE) with FLAME laser will be discussed.

8.2 FLAME: A sub-peta watt laser facility

A new era of laser based plasma accelerators is emerging following the commissioning of many high power laser facilities around the world. Extremely short laser pulses with very high intensities will be available with these newly built facilities and it will become possible to study the extreme conditions of light matter interaction within a small scale laser laboratories. The commissioning of the FLAME laser facility is a step to an integrated approach towards this goal in the framework of PLASMON-X project. Plamson-X is an acronym for plasma acceleration and monochromatic x-ray generation. The FLAME laser is capable of producing some of the most intense light conditions for laser matter interaction. The FLAME laser system is a 300 TW Ti:Sapphire laser capable of accelerating electrons to energies of several hundred-million electron volts in a distance of about few millimetres [139]. The key to FLAME extreme power is its ultra-short pulse duration, 23 femtosecond. High power can be achieved with a moderate amount of energy content in such a short pulse.

FLAME stands for **F**rascati **L**aser for **A**cceleration and **M**ulti-disciplinary **E**xperiments. At present the FLAME laser is in commissioning stage and will be operational with its full power by the end of this year. The main objective of the experiment is to achieve GeV class electron acceleration. In parallel to the commissioning phase, experiment on particle acceleration has been started to test the laser performance and to explore the optimal conditions required for self-injection and acceleration of the particles to few hundreds of MeV in a controlled manner.

8.2.1 Basic specifications

The custom made FLAME Amplitude laser is based on CPA scheme that delivers in about 20 fs, up to 6 J laser pulse at 800 nm with a 10 Hz repetition rate. The system includes a front-end with pulse contrast enhancement (booster), bandwidth control and regenerative amplifier and yield pulses with 0.7 mJ in 80 nm bandwidth. These pulses are then further amplified by the first amplifier up to the 25 mJ level while the second amplifier brings the energy up to the 600 mJ level. The third cryogenic amplifier is based on Ti:Sapphire crystal pumped by 10 frequency doubled Nd:YAG laser pulses for a total of up to 20 J of energy per pulse. The Ti:Sapphire crystal absorbs energy from a pump laser emitting at 532 nm and has a large bandwidth gain profile centered about 815 nm. The extraction energy is as high as 35 %, leading to a final energy in the stretched pulses in excess of 7 J. Pulses are then

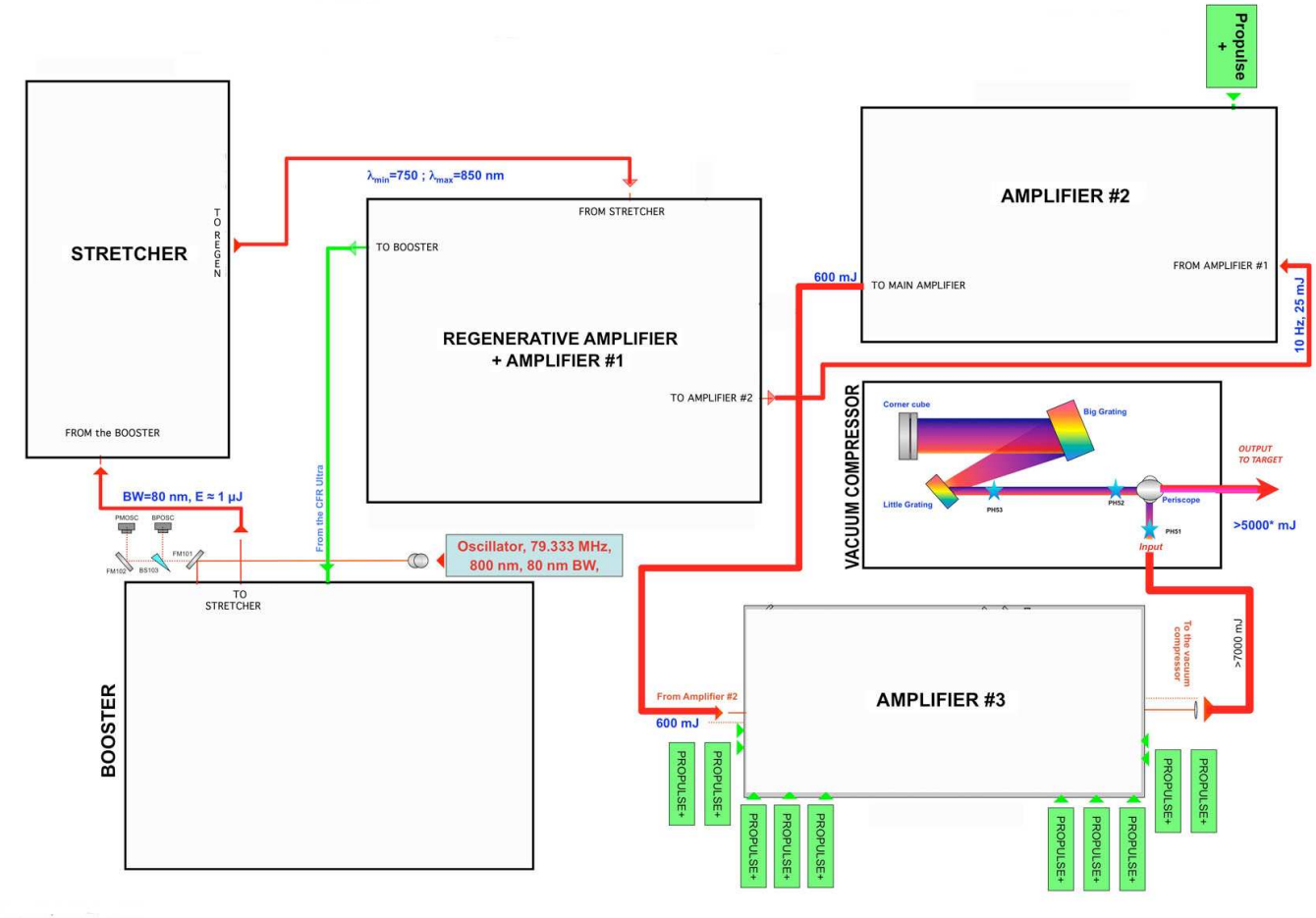

Figure 8.1: Schematic of optical layout of the Flame laser system.

transported in air to the vacuum compressor placed in the underground target area. Once compressed, the pulse is transported under vacuum to the target chamber through remotely controlled beam steering mirrors. The optical layout of the Flame laser system is illustrated in Fig. 8.1. The specifications of the system is given in table 8.1.

Figure 8.2 shows the temporal behaviour of the FLAME laser pulse showing the level of amplified spontaneous emission (ASE) just above 10^{-9} of the peak intensity. At full power the laser pulse can be focused to provide intensities exceeding $10^{20}\mathrm{Wcm}^{-2}$ which, with our ASE contrast, gives a precursor laser intensity on target below $10^{11}\mathrm{Wcm}^{-2}$. In the case of interaction with gases with pressures ranging from 1 to 10 bar, this laser intensity is below the plasma formation threshold for laser pulses of sub-nanosecond duration which is the typical duration of ASE pulses. Therefore we can reasonably assume that in our experimental conditions, no premature plasma formation occurs and the CPA pulse can be

Parameters	Value
Type	Ti:Sapphire
Wavelength	800 nm
Bandwidth	80 nm
Pulse Duration	$\geq$ 23 fs
Max. Energy	$<$ 7 J
Max. Power	up to 300 TW
Pre-pulse Contrast Ratio	10^{10} (at ns scale)
Focusing Optics	F/10 OAP
Target	Supersonic laminar gas jet

Table 8.1: Summary of Flame laser parameters

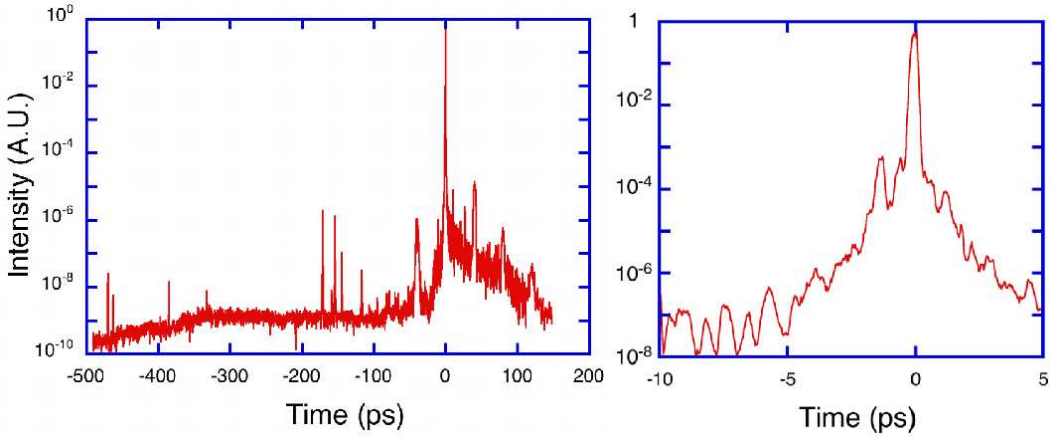

Figure 8.2: Cross-correlation curve (left) showing the detailed temporal structure of the laser pulse in the 500 ps window before the main pulse. The plot on the left shows that intensity of the amplified spontaneous emission is just above 10^{-9} of the peak intensity. The plot on the right shows the detail of the curve in the ps domain, just before the peak intensity.

focused directly in the gas. However, according to the curve of Fig.8.2 some precursor radiation may be present on the ps time scale before the pulse reaches the peak intensity. This radiation may give rise to premature ionization of the gas.

Another salient feature of the FLAME laser system is its high pointing stability. Pointing stability refers to the consistency of the laser beam position from shot to shot. Usually, the laser pointing varies from shot to shot and thus affects the nature of the interaction in terms of reproducibility. The success of any experiment partially depends on the control of the

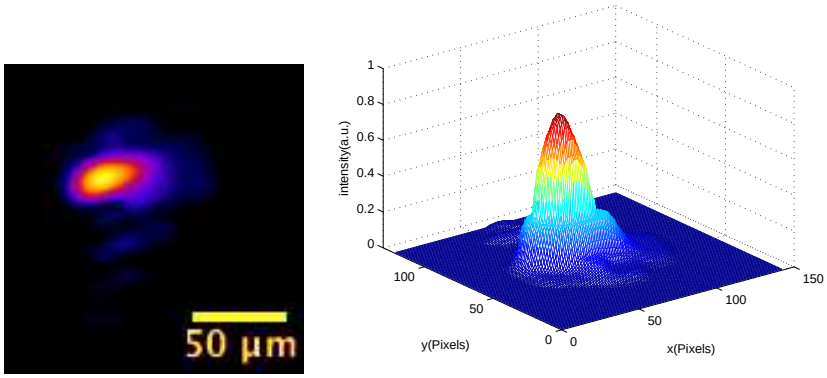

(a) (b)

Figure 8.3: Measured focal spot of the laser pulse. (a) Spatial profile of the focused spot (b) and its corresponding intensity distribution.

laser beam pointing. This depends on both intrinsic properties of the laser system as well as issues arising from the optical components that enable transport of the laser pulses from the laser system to the final optics. In the case of FLAME, due to the complex set up of the installation, it is important to measure the pointing stability of the laser pulse. The beam pointing stability is monitored by measuring the performance of the focal spot of the laser pulse. The focal spot is imaged by an objective to a standard CCD. As a final result, a measurement of the position of the focal spot with a micrometer-scale resolution can be achieved to reach $\mu\mathrm{rad}$ resolution in the beam pointing evaluation. Figure 8.3(a) shows the measured focal spot of laser pulse. The off-axis parabolic mirror (OAP) focused the beam to a spot of around 30 $\mu\mathrm{m}$ FWHM. The beam intensity distribution profile [Fig.8.2(b)] is quasi-Gaussian in shape. The on-line continuous monitoring of this spot showed that the FLAME laser system exhibits good pointing stability (cf.fig.8.4).

The energy stability of the of the pulse is also good. Fig. 8.5 shows the energy curve as a function of time. The energy remains stable for several hours of the measurement. Thus, the key parameters (pointing stability, energy content of the pulse and pulse duration) of the FLAME has shown exceptionally good stability during a long test operation.

8.3 Experimental set-up and preliminary results of SITE

The experiment was carried out at FLAME laser lab at National Laboratory of Frascati. The schematic of the experimental set-up is shown in Fig. 8.6. The amplified stretched pulse

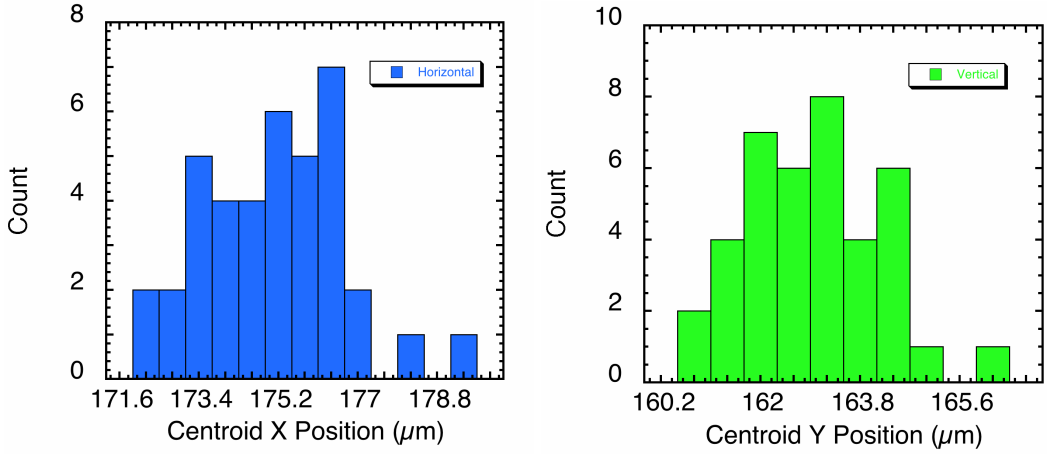

(a) (b)

Figure 8.4: Pointing stability measurements of the focal spot. (a) Pointing stability along X-direction (b) Pointing stability along Y-direction.

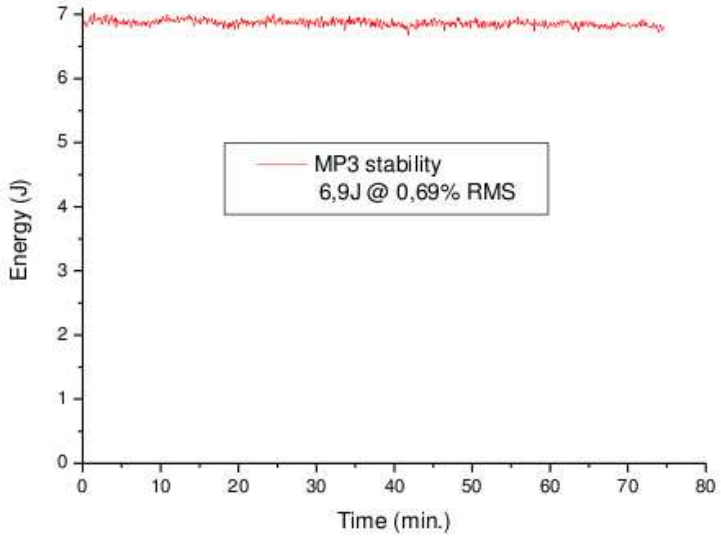

Figure 8.5: Energy stability curve for Flame laser system.

is transported in air from clean room up to the compressor in the target area inside the bunker. Inside the compressor the pulse is compressed back to near its original duration and sent to the interaction chamber through a transport line under vacuum. For the proper alignment of the laser pulse two additional mirrors are placed before the OAP. The laser pulse is focused by the F/10 OAP on a supersonic, laminar gas jet of dimension $4\mathrm{mm} \times 10\mathrm{mm}$. The gas-jet is mounted on a micrometric motorized support that allows the interaction point to be

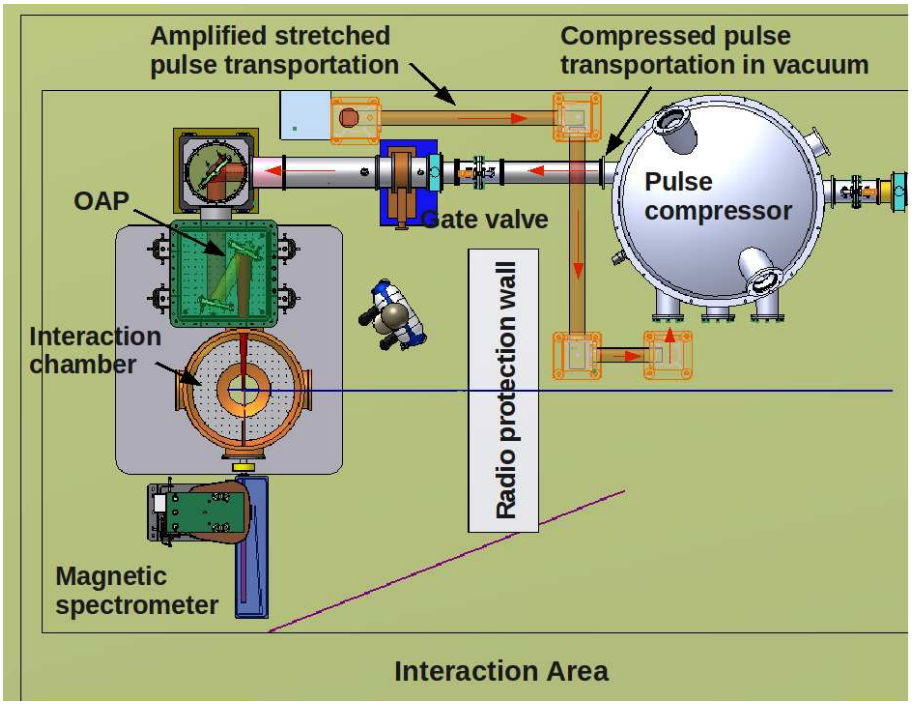

Figure 8.6: Top view of the experimental set-up for the self-injection test experiment with FLAME laser facility.

moved along the three cartesian axes (position scan). Vacuum in the chamber before the shot is maintained at a pressure below $\sim 10^{-5}$ Torr by a turbo-molecular pump connected to the chamber by a gate-valve. Several diagnostics were employed to monitor the interaction point and electron signal [as described in chapter 6]. One of the special feature for the SITE experiment is the newly built fibre optics based magnetic spectrometer. The spectrometer is capable of measuring the enrgy of the particles in the range of $10\mathrm{MeV}$ to $\approx 1\mathrm{GeV}$ [138].

During the first phase of the experiment the main aim was to find minimum threshold conditions for electron acceleration by optimizing the gas and laser parameters. This was done by scanning the laser focus point with respect to the gas jet and monitoring the plasma length through Thomson scattering diagnostic and γ-rays signal from scintillators. The generated electrons were detected on Lanex screen placed at 10 cm behind the gas jet. Nitrogen gas was used in the experiment. After a long scanning process a suitable condition for electron acceleration was found in a pressure regime between 7 to 12 bar. The energy of the laser pulse was between 500 to 600 mJ and the pulse duration was between 30 to 35 fs. The spot size of the focused pulse was around $24\mu\mathrm{m}$ in diameter. The intensity that can be achieved in the preliminary experiment was $< 4 \times 10^{18}\mathrm{Wcm}^{-2}$ [considering the efficiency

Parameters	Value
Pulse duration	30-35 fs
Laser energy	600-800 mJ
Pressure	7-12 bar
Intensity	$< 4 \times 10^{18} \mathrm{Wcm}^{-2}$

Table 8.2: Optimum conditions for electron acceleration in the experiment

of the grating and intensity distribution in the focal spot].

A highly collimated and reproducible electron bunch generation were observed within the mentioned physical conditions. More than 30% electron signals were along the direction of laser propagation and are highly collimated as shown in the figure 8.7. Highly collimated electron bunches were obtained when the pulse was focused in the vicinity of the entrance edge of the gas jet. Some times the electron bunch moved randomly but still remaining close to the laser propagation axis as shown in figure 8.8. This can be correlated with the pointing stability of the laser pulse. Sometimes double peak electron bunches, as shown in figure 8.9, were also observed. The exact reason for this double peaked behaviour is not clear but can be related to the non-uniformity of the intensity distribution in the focused laser spot. Double filament propagation of the laser pulse was observed by Thomson scattering diagnostic.

For a qualitative understanding of the correlation between the interaction conditions, pulse propagation and electron signal generation, forward emitted light was monitored directly on a screen (normal white paper) placed behind the gas jet. The purpose was to observe how the laser pulse gets modified in different conditions of electron generation. Figure 8.10 illustrates how the variation in the spectrum of the forward emitted light and laser pulse propagation (monitored by TS diagnostic) relates with the spatial profile of the electron bunch. The laser was focused near the entrance edge of the gas jet. Initially, when the electron bunch was spread all over the Lanex screen there was hardly any change in the laser pulse colour. As the laser pulse starts propagating in a quasi-stable and self-confined way, the spatial profile of the electron bunch starts reducing and the laser pulse displays some additional colours in its profile. When highly collimated electron bunches are generated the laser pulse displayed a supercontinuum feature in the forward emitted light. These feature were repeatable during the experiment but not very strictly linked with the electron

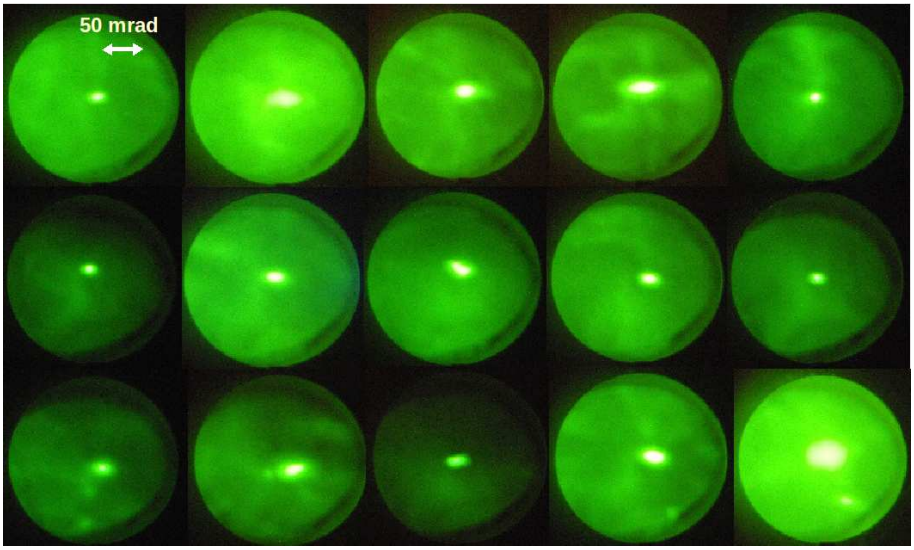

Figure 8.7: A set of electron signal obtained during the experiment in the absence of magnetic spectrometer. A highly collimated electron bunch along the direction of laser propagation were generated with high reproducibility. The shots are not consecutive.

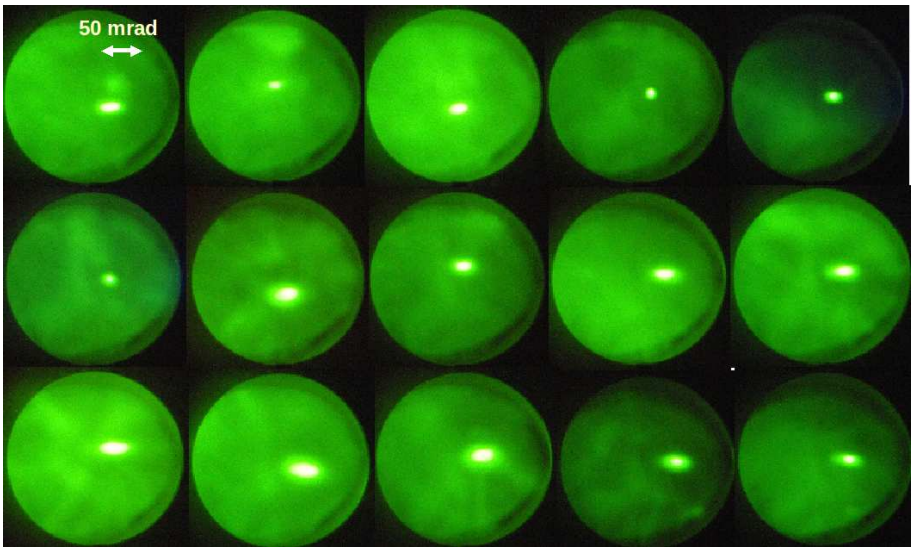

Figure 8.8: Consequence of pointing stability: Less directional electron bunches.

bunch profile. However, the change in colour of the transmitted pulse provided clear evidence for the strong and weak interaction of the laser pulse with the medium. It is consistent with the modulation of the pulse profile due to ionization inducing self-phase modulation.

A permanent magnet spectrometer was used to measure the electron energy spectrum. The strength of the magnetic field was 0.9 Tesla. The magnet was placed 10 cm behind the

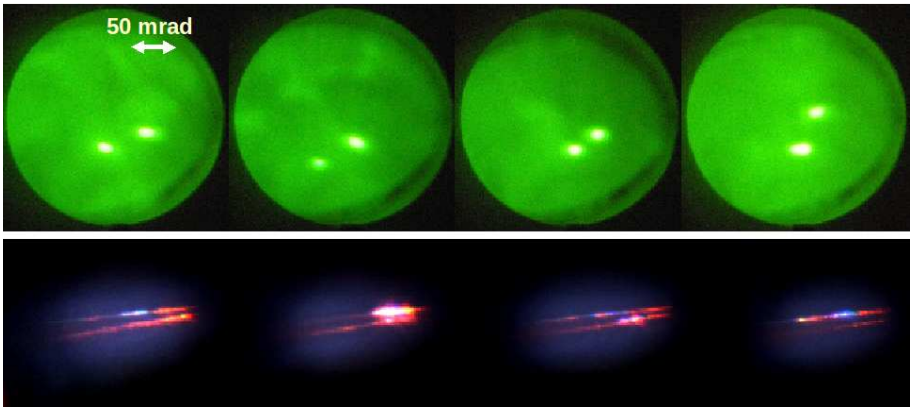

Figure 8.9: Double peaked electron signals and their corresponding Thomson scattering images. Due to non-uniform intensity distribution in the laser beam occasionally the pulse breaks up into two components so producing multiple electron bunches.

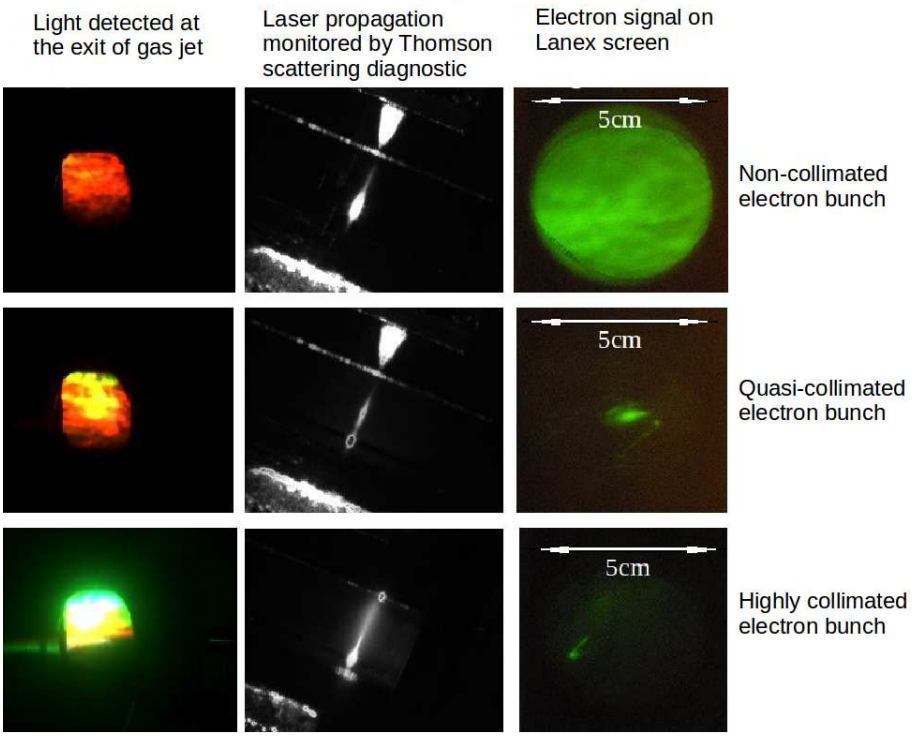

Figure 8.10: A typical behaviour of forward transmitted laser pulse and its correlation with electron bunch profile.

exit edge of the gas jet. The length of the magnetic field region was 50 mm and the Lanex screen was placed at 30 cm from the magnet exit. Figure 8.11 shows an energy spectrum of an electron signal obtained during the experiment. The image displays a two mono-energetic

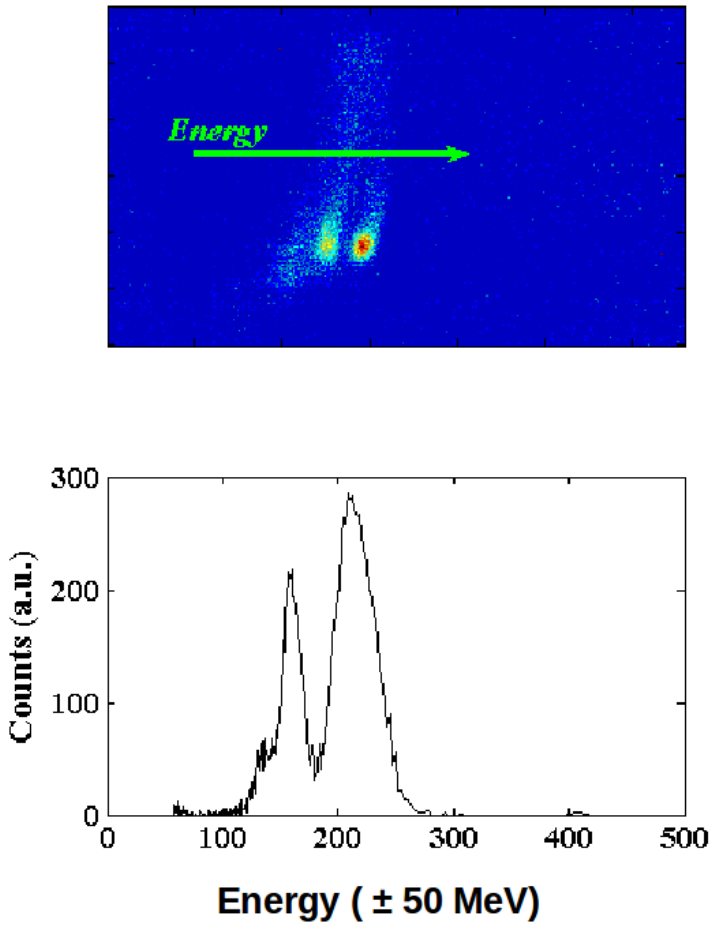

Figure 8.11: Electron bunch deflected by a permanent magnetic field and its corresponding spectrum obtained during the first phase of the experiment. The image display the mono-energetic feature in multi MeV energy range.

peaks in multi MeV energy range.

8.4 Conclusion

The main objective in the first phase of the SITE experiment was to explore the minimum conditions for stable and high energetic (100s of MeV) electron generation. The minimum requirements were successfully achieved with good reproducibility of the electron signal and bunch quality. Electron bunches with small divergence and high directionality were generated. Even though the pointing stability of the laser pulse was quite good, beam break-

up was found to be critical in governing the shape of the electron bunch.

Part VI

Conclusion and references

Conclusions and future prospects

In this thesis experimental studies on high intensity laser matter interaction were presented. The main objective of the thesis was understanding the process of laser pulse propagation in plasmas and subsequent generation of energetic electrons. For this purpose various aspects of high power short pulse laser interaction with gases and underdense plasmas have been studied experimentally and numerically. Experiments were performed with both, moderate and high power laser systems. Many diagnostics were employed to study and control the laser matter interaction. Most important one is the time-resolved interferometry, which provide information on plasma density evolution and Thomson scattering, which proved to be very useful during the experiment. Some issues regarding stable propagation of laser pulse in plasma was also studied. It was found that stable propagation of laser pulses is possible even in high density gas target.

The generation of energetic electrons was explored with different gas targets. With low power laser system it was found that low atomic number gas targets, like helium, are good for producing low diverging electrons. However, the energy of these electrons was limited to only few MeV's. With high atomic number gas target, like nitrogen, large diverging electrons with few tens of MeV of energy can be produced. Moreover, the high atomic number gas targets have displayed an extraordinary behaviour in modulating the frequency spectrum of the laser pulse. In nitrogen and argon gases large frequency up-shift of the incident laser pulse was recorded. Such a huge variation in frequency of the laser pulse during propagation has never reported before (to our best knowledge). These time-integrated images of frequency variation implies that proper control of the laser and gas medium could produce controlled modification of the laser spectrum. These observation can also be used as a potential tool for very intense laser pulses where direct measurement of laser parameters is not possible. In addition, these observation also partially distinguish between the different interaction regimes during the propagation. For example, highly non-linear regime can be

distinguished from other weakly non-linear or linear regime based on the observation of the propagation region. The frequency modulation will be more important where propagation is non-linear. This way one can distinguish different regions during the propagation and can qualitatively make an estimation about laser intensity changes during propagation.

One of the most important issue in laser matter interaction is to search for stable propagation of laser pulses in plasmas. Tremendous progress in this direction has been made in past years. Stable propagation of single laser pulse, without any external guiding, seems to be difficult specially with high atomic number gas targets. In the present work, we found that a moderate power laser pulse can propagate without any early optical or ionization induced defocusing, even in high atomic number gas targets and at high pressure. The experimental observation suggests that nature of the target medium plays a crucial role in guiding the laser pulse. Proper choice of target is found to be essential within an available laser pulse parameters, as it can enhanced or spoil the laser pulse propagation in plasmas.

The work presented in this thesis is significant from fundamental laser plasma interaction study point of view. The work will be extended further to explore the effect of external axial magnetic field on the stable propagation of the laser pulses and on the divergence of the electron bunch profile. We intend to study the frequency up-shift process in more detail and with different atomic species; to find a way to generate new compact radiation sources.

List of publications

[1] **N. C. Pathak**, C. A. Cecchetti, A. Gamucci, A. Giulietti, D. Giulietti, P. Koester, L. Labate ,T. Levato, L. Nizzoli, F. Piastra and L. A. Gizzi, "Influence of atomic species on laser pulse propagation in underdense plasmas", *Accepted in Nuclear Instruments and Methods in Physics Research A.*

[2] T. Levato, **N. C. Pathak**, C. A. Cecchetti, O. Ciricosta, P. Koester, L. Labate, A. Giulietti, D. Giulietti, F. De Angelis, E. Di Fabrizio, P. Delogu and L. A. Gizzi, "Fabrication of $3\mu m$ diameter pin hole array (PHA) on thick W substrates", *AIP proc. ULIS* **1209**, 59 (2009).

[3] T. Levato, L. Labate, **N. C. Pathak**, C. Cecchetti, P. Koester, E. Di Fabrizio, P. Delogu, A. Giulietti, D. Giulietti and L.A. Gizzi, "Pin-hole array production and detailed data analysis for advanced single-shot X-ray imaging of laboratory plasmas", *Nuclear Instruments and Methods in Physics Research A* **623** , 842 (2010).

[4] L. A. Gizzi, C. Benedetti, S. Betti, C. A. Cecchetti, A. Gamucci, A. Giulietti, D. Giulietti, P. koester, L. Labate, T. Levato, F. Michienzi, **N. Pathak**, A. Sgattoni, G. Turchetti and F. Vittori, "Laser Plasma Acceleration: First experimental results from the Plasmon-X project", *Proc. of channelling 2008 conference*, 485 (2010).

[5] L. Labate, F. Anelli, A. Bacci, D. Batani, M. Bellaveglia, C. Benedetti, R. Benocci, L. Cacciotti, C. Cecchetti, O. Ciricosta, A. Clozza, L. Cultrera, G. Pirro, N. Drenska, R. Faccini, M. Ferrario, D. Fillippetto, S. Gallo, S. Fioravanti, A. Gamucci, G. Gatti, A. Ghigo, A. Giulietti, D. Giulietti, P. Koester, T. Levato, V. Lollo, E. Pace, **N. Pathak**, A. Rossi, L. Serafini, G. Turchetti, C. Vaccarezza, P. Valente, C. Vicario, L. Gizzi. "A self-injection acceleration test experiment for the FLAME laser", *Radiation Effects and Defects in Solids* **165**, 787 (2010).

[6] R. Faccini, F. Anelli, A. Bacci, D. Batani, M. Bellavegli, R. Benocci, C. Benedetti, L. Cacciotti, C.A.Cecchetti, A.Clozza , L. Cultrera, G. Di Pirro, N. Drenska, F. Anelli, M. Ferrario , D. Filippetto, S. Fioravanti, A. Gallo, A. Gamuccih, G. Gatti, A. Ghigo, A. Giulietti, D. Giuliett, L. A. Gizzi, P. Koester, L. Labate, T. Levato, V. Lollo, P. Londrillo, S. Martellotti, E. Pace, **N. Pathak**, A. Rossi, F. Tania, L. Serafini, G. Turchetti, C. Vaccarezza and P. Valente, "Multi-GeV Electron Spectrometer", *Nuclear Instruments and Methods in Physics Research A* **623** , 704 (2010).

[7] S. Betti, A. Giulietti, D. Giulietti, L. A. Gizzi, M. Vaselli, C. A. Cecchetti, A. Gamucci, P. koester, L. Labate, **N. Pathak**, T. Levato, A. A. Andreev, T. Ceccotti, P. Martin and P. Monot, "Towards Laser-Driven Quasi-Monochromatic Ion Bunches via Ultrathin Targets Nano-Structuring", *AIP proc. ULIS*, **1209**, 15 (2009).

[8] **Manuscript in preparation**
A. Giulietti, **N. C. Pathak**, C. A. Cecchetti, D. Giulietti, T. Hosokai, P. Koester, H. Kotaki, L. Labate, T. Levato and L. A. Gizzi, "Space- and time-resolved observation of strong laser frequency up-shifting during ultrafast plasma formation".

[9] **Manuscript in preparation**
T. Levato, L. Labate, **N. C. Pathak**, F. Piastra, C. A. Cecchetti, N. Drenska, R. Faccini, D. Giulietti, S. Martellotti, P. Valente and L. A. Gizzi, "Pointing stability and beam quality in GeV-scale laser-plasma acceleration".

[10] **Manuscript in preparation**
T. Levato, M. Calvetti, **N. C. Pathak**, V. Lollo, F. Piastra, D. Giulietti, L. Labate and L. A. Gizzi, "First preliminary results from the new Frascati Laser for Acceleration and Multidisciplinary Experiments (FLAME) at National Laboratory of Frascati (LNF).".

Bibliography

[1] T.H. Mainman, *Nature* **187**, 493 (1960).

[2] D. Strickland and G. Mourou, *Opt. Commun.* **56**, 219 (1985).

[3] P. Maine, D. Strickland, P. Bado, M. Pessot and G. Mourou, *IEEE J. Quantum Electron* **24**, 398 (1988).

[4] T. Brabec and F. Krausz, *Rev. Mod. Phys.* **72**, 545 (2000).

[5] P. Gibbon and E. Förster, *Plasma Phys. control. Fusion* **38**, 769 (1996).

[6] K.A. Brueckner and S. Jorna, *Rev. Mod. Phys.* **46**, 325 (1974).

[7] R. Kodama, P. A. Norreys, K. Mima, A. E. Dangor, R. G. Evans, H. Fujita, Y. Kitagawa, K. Krusheinick, T. Miyakoshi, N. Miyanaga, T. Norimatsu, S. J. Rose, T. Shozaki, K. Shigemori, A. Sunahara, M. Tampo, K. A. Tanaka, Y. Toyama, T. Yamanaka and M. Zepf, *Nature* **412**, 798 (2001).

[8] R. Kodama, H. Shiraga, K. Shigemori, Y. Toyama, S. Fujioka, H. Azechi, H. Fujita, H. Habara, T. Hall, Y. Izawa, T. Jitsuno, Y. Kitagawa, K. Krusheinick, K. Lancaster, K. Mima, K. Nagai, M. Nakai, H. Nishimura, T. Noriatsu, P. A. Norreys, S. Sakabe, K. Tanaka, A. Youssef, M. Zepf and T. Yamanaka, *Nature* **418**, 933 (2001).

[9] K. A. Tanaka, R. Kodama, H. Fujita, M. Heya, N. Izumi, Y. Kato, Y. Kitagawa, K. Mima, N. Miyanaga, T. Norimatsu, A. Pukhov, A. Sunahara, K. Takahashi, M. Allen, H. Habara, T.Iwatani, T. Matusita, T. Miyakosi, M. Mori, H. Setoguchi, T. Sonomoto, M. Tanpo. S.Tohyama, H. Azuma, T. Kawasaki, T. Komeno, O. Maekawa, S. Matsuo, T. Shozaki, Ka Suzuki, H. Yoshida, T. Yamanaka, Y. Sentoku, F. Weber, T. W. Barbee and L. DaSilva , *Phys. Plasmas* **7**, 2014 (2000).

[10] J.D. Lindl, P. Amendt, R.L. Berger, S.G., Glendinning, S.H. Glenzer, S.W. Haan, R.L. Kauffman, O.L. Landen and L.J. Suter, *Phys. Plasmas* **11**, 339 (2004).

[11] T. Tajima and J. Dawson, *Phys. Rev. Lett.* **43**, 267 (1979).

[12] E. Esarey, P. Sprangle, J. Krall and A. Ting, *IEEE Trans. Plasma Sci.* **24**, 252 (1996).

[13] K. Nakajima, *Las. Part. Beams* **18**, 519 (2000).

[14] M.J. Hogan, C.D. Barnes, C.E, Clayton et al., *Phys. Rev. Lett.* **95**, 054802 (2005).

[15] C. Joshi and T. Katsouleas, *Phys. Today*, p-47 (2003)

[16] K. Witte, C. Ghan, J Meyer-ter-Vehn, G. Pretzler, A. Pukhov and G. Tsakiris, *Plasma Phys. Control. Fusion* **44**, B221 (1999).

[17] C. Joshi, *Phys. Plasmas* **14**, 055501 (2007).

[18] E. Esarey, C.B. Schroeder and W.P. Leemans, *Rev. Mod. Phys.* **81**, 1229 (2009).

[19] T. Katsouleas, *Nature* **431**, 515 (2004).

[20] R. Bingham, J.T. Mendonca and P.K. Shukla, *Plasma Phys. control. Fusion* **46**, R1 (2004).

[21] M.E. Wright, *Symmetery* **2**, 12 (2005).

[22] M.N. Rosenbluth and C.S. Liu, *Phys. Rev. Lett.* **29**, 701 (1972).

[23] F. Dorchies, F. Amiranoff, V. Malka, J.R. Marques, A. Modena, D. Bernard, F. Jacquet, Ph. Mine, B. Cros, G. Matthieussent, P. Mora, A. Solodov, J. Morillo and Z. Najmudin, *Phys. Plasmas* **6**, 2903 (1999).

[24] Z. Najmudin, K. Krushelnick, E.L. Clark, S.P.D. Mangles, B. Walton, A.E. Dangor, S. Fritzler, V. Malka, E. Lefebvre, D. Gordon, F.S. Tsung and C. Joshi, *Phys. Plasmas* **10**, 2071 (2003).

[25] S.P.D. Mangles, B.R. Walton, M. Tzzoufras, Z. Najmudin, R.J. Clarke, A.E. Dangor, R.G. Evans, S. Fritzler, A. Gopal, C.H. Gomez, W.B. Mori, W. Rozmus, M. Tatarakis, A.G.R. Thomas, F.S. Tsung, M.S. Wei and K.Krushelnick, *Phys. Rev. Lett.* **94**, 245001 (2005).

[26] C. Ghan, G.D. Tatakiris, A. Pukhov, J. Meyer-ter-Vehn, G. Pretzler, P. Thirolf, D. Habs and K.J. Witte, *Phys. Rev. Lett.* **83**, 4772 (1999).

[27] A. Pukhov and J. Meyer-ter-Vehn, *Appl. Phys. B* **74**, 355 (2002).

[28] I. Kostyukov, A. Pukhov and S. Kiselev, *Phys. Plasmas* **11**, 5256 (2004).

[29] K. Nakajima, D. Fisher, T.Kawakubo, H. Nakahishi, A. Ogata, Y. Kato, Y. Kitagawa, R. Kodama, K. Mima, H. Shiraga, K. Suzuki, Y. Yamakawa, T. Zhang, Y. Sakawa, T. Shoji, Y. Nishida, N. Yugami, M. Downer and T. Tajima, *Phys. Rev. Lett.* **74**, 4428 (1995).

[30] F. Amiranoff, S. Baton, D. Bernard, B. Cros, D. Descamps, F. Dorchies, F. Jacquet, V. Malka, J.R. Marques, G. Matthieussent, P. Mine, A. Modena, P. Mora, J.Morillo and Z. Najmudin, *Phys. Rev. Lett.* **81**, 995 (1998).

[31] F. Dorchies, F. Amiranoff, V. Malka, J.R. Marques, A. Modena, D. Bernard, F. Jacquet, P. Mine, B. Cros, G. Matthieussent, P. Mora, A. Solodov, J. Morillo and Z. Najmudin, *Phys. Plasmas* **6**, 2903 (1999).

[32] A. Modena, Z. Najmudin, A.E. Dangor, C.E. Clayton, K.A. Marsh, C. Joshi, V. Malka, C.B. Darrow, C. Danson, D. Neely and F.N. Walsh, *Nature* **377**, 606 (1995).

[33] C.E. Clayton, C. Joshi, C. Darrow and D. Umstadter, *Phys. Rev. Lett.* **54**, 2343 (1985).

[34] F.A. miranoff et al, *Phys. Rev. Lett.* **81**, 985 (1992).

[35] C.T. Hsieh, C.M. Huang, C.L. Chang, Y.C. Ho, Y.S. Chen, J.Y. Lin, J. Wang and S.Y. Chen, *Phys. Rev. Lett.* **96**, 095001 (2006).

[36] M. Everett et al., *Nature* **368**, 527 (1994).

[37] S.P.D. Mangles, C.D. Murphy, Z. Najmudin, A.G.R. Thomas et al., *Nature* **431**, 535 (2004).

[38] J. Faure, Y. Glinec, A. Pukhov, S. Kiselev, S. Gordienko, E. Lefebvre, J.P. Rousseau, F. Burg and V. Malka, *Nature* **431**, 538 (2004).

[39] C.G.R. Geddes, Cs. Toth, J. Van Tilborg, E. Esarey, C.B. Schroeder, D. Brumwiler, C. Nietre, J. Cary and W.P. Leemans, *Nature* **431**, 541 (2004).

[40] C.G. Durfee and H.M. Milchberg, *Phys. Rev. Lett.* **71**, 2409 (1993).

[41] J. Faure, C. Rechatin, A. Norlin, A. Lifschitz, Y. Glinec and V. Malka, *Nature* **444**, 737 (2006).

[42] W.P. Leemans, D. Rodgers, P.E. Catravas, C.G.R. Geddes, G. Fubiani, E. Esarey, B.A. Shadwick, R. Donahue and A. Smith, *Phys. Plasmas* **8**, 2510 (2001).

[43] M.I.K. Santala, Z. Najmudin, E.L. Clark, M. Tatarakis, K. Krusheinick, A.E. Dangor, V. Malka, J. Faure, R. Allott and R.J. Clarke, *Phys. Rev. Lett* **86**, 1227 (2001).

[44] M.I.K. Santala, M. Zepf, F.N. Beg, E.L. Clark, A.E. Dangor, K. Krusheinick, M. Tatarakis, I. Watts, K.W.D. Ledingham, T. McCanny, I. Spencer, A.C. Machacek, R. Allott, R.J. Clarke and P.A. Norreys, *Appl. Phys. Lett* **78**, 19 (2001).

[45] K.W.D. Ledingham, P. McKenna and R.P. Singhal, *Science* **300**, 1107 (2003).

[46] A. Rousse, K. Ta Phuoc, R. Shah, A. Pukhov, E. Lefebvre, V. Malka, S. Kiselev, F. Burgy, J.P. Rousseau, D. Umstadter and D. Hulin, *Phys. Rev. Lett.* **93**, 135005 (2004).

[47] Z.M. sheng, K. Mima, J. Zhang and H. sanuki, *Phys. Rev. Lett.* **94**, 095003 (2005).

[48] H. Hamster, A. Sullivan, S. Gordon, W. White and R.W. Falcone, *Phys. Rev. Lett.* **71**, 2725 (1993).

[49] W.P. Leemans, C.G.R. Geddes, J. Faure, Cs. Toth, J. van Tilborg, C.B. Schroeder, E. Esarey, G. Fubiani, D. Auerbach, B. Marcelis, M.A. Carnahan, R.A. kaindl, J. Byrd and M.C. Martin, *Phys. Rev. Lett.* **91**, 074802 (2003).

[50] H. C. Wu and J. Meyer-ter-Vehn, 36^{th} *EPS Conference on Plamsa Phys.* **33**, 2027 (2009).

[51] B. Hitz, J. J. Ewing and J. Hecht, *Introduction to Laser technology,* Third Edition, IEEE Press, New York (2001).

[52] D. E. Spence, P. N. Kean and W. Sibbett, *Opt. Lett.* **16**, 42 (1991).

[53] see, for instance, chapter 3 in *Femtosecond Laser Pulses* by C. Rulliere, Springer Verlag, Berlin (1998).

[54] P. M. W. French, *Rep. Prog. Phys.* **58**, 169 (1995).

[55] W. T. Silfvast, *Laser Fundamentals*, Second Edition, Cambridge University Press (2004).

[56] P. Tournois, *Optics Communications* **140**, 4 (1997).

[57] F. Verluise, V. Laude, Z. Cheng, Ch. Spielmann and P. Tournois, *Optics Letters* **25**, 575 (2000).

[58] M. P. Kalashnikov, K. Osvay, I. M. Lachko, H. Schonnagel and W. Sandner, *Appl. Phys. B* **81**, 1059 (2005).

[59] V. L. Ginzburg, *Propagation of electromagnetic waves in plasmas*, Pergamon, New York (1964).

[60] F. F. Chen, *Introduction to plasma physics and controlled fusion*, Plenum Press, New York (1984).

[61] L. Tonks and I. Langmuir, *Phys. Rev.* **33**, 195 (1929).

[62] D. Bohm and E. P. Gross, *Phys. Rev* **75**, 1851 (1949).

[63] S. C. Wilks and W. L. Kruer, *IEEE J. Quantum Electron.* **33**, 1954 (1997).

[64] D. W. Forslund, J. M. Kindel and K. Lee, *Phys. Rev. Lett.* **39**, 284 (1977).

[65] K. Estabrook and W. L. Kruer, *Phys. Rev. Lett.* **40**, 42 (1978).

[66] U. Teubner, J. Bergmann, B. van Wonterghem, F. P. Schafer and R. Sauerbrey, *Phys. Rev. Lett. 70*, 794 (1993).

[67] F. Brunel, *Phys. Rev. Lett.* **59**, 52 (1987).

[68] S. Eliezer, *The interaction of high-power lasers with plasmas*, Series in plasma physics, IOP (2006).

[69] L. D. Landau and A. F. Lifshits, *Classical Theory of Fields*, 2nd edition ed. (Addison-Wesley, Reading. Mass., 1962).

[70] J. H. Eberly and A. Sleeper, *Phys. Rev.* **176**, 1570 (1968).

[71] A. Pukhov, *Lecture notes on laser-plasma interaction*.

[72] D. Bauer, P. Mulser and W. H. Steeb, *Phys. Rev. Lett.* **75**, 4622 (1995).

[73] B. Quesnel and P. Mora, *Phys. Rev. E* **58**, 3719 (1998).

[74] G. A. Askaryan, *Zh. Eksp. Teor. Fiz.* **42**, 1672 (1962).

[75] S. A. Akhmanov, A. P. Sukhorukov and R. V. Khokhlov, *Sovt. Phys. JETP* **24**, 198 (1967).

[76] S. A. Akhmanov, A. P. Sukhorukov and R. V. Khokhlov, *Sovt. Phys. JETP* **10**, 609 (1968).

[77] M. S. Sodha, A. K. Ghatak and V. K. Tripathi, *Prog. in optics* **13**, North Holland Amsterdam (1976).

[78] C. S. Liu and V. K. Tripathi, *Interaction of electromagnetic waves with electron beams and plasmas*, World Scientific, Singapore (1994).

[79] M. Hercher, *J. Opt. Soc. Am.* **54**, 563 (1964).

[80] G. Schmidt and W. Horton, *Comments Plasma Phys. controlled fusion* **9**, 85 (1985).

[81] C. E. Max, J. Arons and B. Lagdon, *Phys. Rev. Lett.* **33**, 209 (1974).

[82] H. Hora, *J. Opt. Soc. Am.* **65**, 882 (1975).

[83] C. E. Max, *Phys. Fluids* **19**, 74 (1976).

[84] Y. C. Lee, G. Z. Sun, E. Ott and P. Guzdar, *Phys. Fluids* **30**, 526 (1987).

[85] A. Borisov, A. V. Borovisky, V. V. Korobkin, A. M. Prokhorov, O. B. Shiryaev, X. M. Shi, T. S. Luk, A. McPherson, J. C. Solem, K. Boyer and C. K. Rhodes, *Phys. Rev. Lett.* **68**, 2309 (1992).

[86] P. Sprangle, C. M. Tang and E. Esarey, *IEEE Trans. Plasma Sci.* **PS-15**, 145 (1987).

[87] P. Sprangle, E. Esarey, A. Ting and G. Joyce, *Appl. Phys. Lett.* **53**, 2146 (1998).

[88] P. Sprangle and E. Esarey, *Phys. Rev. Lett.* **67**, 2021 (1991).

[89] E. Esarey, C. B. Schroeder, B. A. Shadwick, J. S. Wurtele and W. P. Leemans, *Phys. Rev. Lett.* **84**, 3081 (2000).

[90] E. Esarey, P. Sprangle and J. Krall, *IEEE J. Quantum Electron.* **33**, 1879 (1997).

[91] J. Faure, V. Malka, J. Marques, P. David, F. Amiranoff, K. Ta Phuoc and A. Rousse, *Phys. Plasmas* **9**, 756 (2002).

[92] C. Delfin, V. Lokhnygin, J. Mauritsson, A. Sjögren, C. G. Wahlström, A. Pukhov and G. D. Tsakiris, *Phys. Plasmas* **9**, 937 (2002).

[93] W. Lu, C. Huang, M. Zhou, W. B. Mori and T. Katsouleas, *Phys. Rev. Lett.* **96**, 165002 (2006).

[94] V. S. Popov, *Physics - Uspekhi*, **47**, 855 (2004).

[95] L. V. Keldysh, *Soviet Phys. JETP* **20**, 1307 (1964).

[96] H. R. Reiss, *Phys. Rev. A* **22**, 1786 (1980).

[97] M. Y. Ivanov, M. Spanner and O. Smirnova, *Jour. Mod. Optics* **52**, 165 (2005).

[98] P. Gibbon, *Short Pulse Laser Interaction With Matter*, Imperial College Press, London (2005).

[99] R. Shakeshaft, R. M. Potvliege, M. Dörr and W. E. Cooke, *Phys. Rev. A* **42**, 1656 (1990).

[100] G. L. Yudin and M. Y. Ivanov, *Phys. Rev A* **64**, 013409 (2001).

[101] A. Giulietti et al., Phys. Plasmas 13, 093103 (2006).

[102] A. Giulietti et al., Las. Part. Beams 25, 513 (2007).

[103] T. Hosokai, K. Kinoshita, A. Zhidkov, K. Nakamura, T. Watanabe, T. Ueda, H. Kotaki, M. Kando, K. Nakajima and M. Uesaka, *Phys. Rev. E* **67**, 036407 (2003).

[104] T. Hosokai, K. Kinoshita, A. Zhidkov, A. Maekawa, A. Yamazaki and M. , *Phys. Rev. Lett.* **97**, 075004 (2006).

[105] R. Benattar et al., Rev. Sci. Instrum., 50(12) (1979).

[106] P. Tomassini, A. Giulietti, L. A. Gizzi, M. Galimberti, D. Giulietti, M. Borghesi, and O. Willi, *Appl. Opt., vol.* **40**, 6561 (2001).

[107] M. Galimberti, *J. Opt. Soc. Amer. A* **24**, 304 (2007).

[108] L. A. Gizzi, M. Galimberti, A. Giulietti, D. Giulietti, P. Koester, L. Labate, P. Tomassini, P. Martin, T. Ceccotti, P. D'Oliveira and P. Monot, *Phys Rev. E* **74**, (2005).

[109] A. Gamucci, M. Galimberti, D. Giulietti, L. A. Gizzi, L. Labate, C. Petcu, P. Tomassini, and A. Giulietti, *Appl. Phys. B* **85**, 611 (2006).

[110] K. Kinoshita, T. Hosokai, T. Okhubo, A. Maekawa, A. Zhidkov and M. Uesaka, *Laser Phys.* **16**, 660 (2006)

[111] H. Ruhl, *Classical Particle Simulations with PSC Code*, Code documentation (unpublished).

[112] A. Giulietti, N. Bourgeois, T. Ceccotti, X. Davoine, S. Dobosz, P. D. Oliveira, M. Galimberi, J. Galy, A. Gamucci, D. Giulietti, L. A. Gizzi, D. J. Hamilton, E. Lefebvre, L. Labate, J. R. Marques, P. Monot, H. Popescu, F. Reau, G. sarri, P. Tomassini and P. Martin, *Phys. Rev. Lett.* **101**, 105002 (2008).

[113] W. L. Kruer, *The Physics of Laser Plasma Interactions*, Addison-Wesley Publishing Company (1988).

[114] T. Afshar-Rad, S. Coe, A. Giulietti, D. Giulietti and O. Willi, *Europhys. Lett.* **15**, 745 (1991).

[115] E. Yablonovitch, *Phys. Rev. Lett.* **31**, 877 (1973).

[116] W. M. Wood, C. W. Siders and M. C. Downer, *IEEE Trans. Plasma Sci.* **21**, 20 (1993).

[117] J. T. Mendonca, *Theory of Photon Acceleration*, Series in Plasma Physics, IOP (2001).

[118] E. Yablonovitch, *Phys. Rev. A* **10**, 1888 (1974).

[119] E. Yablonovitch, *Phys. Rev. Lett.* **31**, 877 (1973).

[120] E. Yablonovitch, *Phys. Rev. Lett.* **32**, 1101 (1974).

[121] W. M. Wood, G. Focht and M. C. Downer, *Optics Lett.* **13**, 984 (1988).

[122] M. Ciarrocca, J. P. Marangos, D. D. Burgess, M. H. R. Hutchinson, R. A. Smith, S. C. Rae and K. Burnett, *Optics Commun.* **110**, 425 (1994).

[123] C. Wilks, J. M. Dawson and W. B. Mori, *Phys. Rev. Lett.* **61**, 337 (1988).

[124] E. Esarey, A. Ting and P. Sprangle, *Phys. Rev. A* **42**, 3526 (1990).

[125] E. Esarey, G. Joyce and P. Sprangle, *Phys. Rev. A* **44**, 3908 (1991).

[126] V. B. Gildenburg, A. V. Kim, V. A. Krupnov, V. E. Semenov, A. M. Sergeev and N. A. zharova, *IEEE Trans. Plasma Sci.* **21**, 34 (1993).

[127] A. Bendib, A. Tahraoui, K. Kalache, P. chessa and P. Mora, *Optics Commun.* **142**, 146 (1997).

[128] C. S. Liu and V. K. Tripathi, *Phys. Plasmas* **7**, 4360 (2000).

[129] S. C. Rae, *Optics Commun.* **104**, 330 (1994).

[130] V. B. Gildenburg, V. I. Pozdnyakova and I. A. Shereshevskii, *Phys. Lett. A* **203**, 214 (1995).

[131] S. C. Rae and K. Burnett, *Phys. Rev. A* **46**, 1084 (1992).

[132] P. Chessa, E. De. Wispelaere, F. Dorchies, V. Malka, J. R. Marques, G. Hamoniaux, P. Mora and F. Amiranoff, *Phys. Rev. Lett.* **82**, 552 1999.

[133] J. K. Koga, N. Naumova, M. Kando, L. N. Tsintsadze, K. Nakajima, S. V. Bulanov, H. Dewa, H. Kotaki and T. Tajima, *Phys. Plasmas* **7**, 5223 (2000).

[134] C. D. Murphy, R. Trines, J. Vieira, A. J. W. Reitsma, R. Bingham, J. L. Collier, E. J. Divall, P. S. Foster, C. J. Hooker, A. J. Langley, P. A. Norreys, R. A. Fonseca, F. Fiuza, L. O. Silva, J. T. Mendonca, W. B. Mori, J. G. Gallacher, R. Viskup, D. A. Jaroszynski, S. P. D. Mangles, A. G. R. Thomas, K. Krushelnick and Z. Najmudin, *Phys. Plasmas* **13**, 033108 (2006).

[135] R. M. G. M Trines, C. D. Murphy, K. L. Lancaster, O. Chekhlov, P. A. Norreys, R. Bingham, J. T. Mendonca, L.O. Silva, S. P. D. Mangles, C. Kamperidis, A. Thomas, K. Krushelnick and Z. Najmudin, *Plasma Phys. Control. Fusion* **51**, 024008 (2009).

[136] J. Gao, *Phys. Rev. Lett.* **93**, 243001 (2004).

[137] J. Gao, *Appl. Phys. Lett* **88**, 091105 (2006).

[138] R. Faccini, F. Anelli, A. Bacci, D. Batani, M. Bellavegli, R. Benocci, C. Benedetti, L. Cacciotti, C.A.Cecchetti, A.Clozza , L. Cultrera, G. Di Pirro, N. Drenska, F. Anelli, M. Ferrario , D. Filippetto, S. Fioravanti, A. Gallo, A. Gamuccih, G. Gatti, A. Ghigo, A. Giulietti, D. Giuliett, L. A. Gizzi, P. Koester, L. Labate, T. Levato, V. Lollo, P. Londrillo, S. Martellotti, E. Pace, N. Pathak, A. Rossi, F. Tania, L. Serafini, G. Turchetti, C. Vaccarezza and P. Valente, *Nucl. Inst. Meth. Phys. Res. A* **623** , 704 (2010).

[139] L. Labate, F. Anelli, A. Bacci, D. Batani, M. Bellaveglia, C. Benedetti, R. Benocci, L. Cacciotti, C. Cecchetti, O. Ciricosta, A. Clozza, L. Cultrera, G. Pirro, N. Drenska, R. Faccini, M. Ferrario, D. Fillippetto, S. Gallo, S. Fioravanti, A. Gamucci, G. Gatti, A. Ghigo, A. Giulietti, D. Giulietti, P. Koester, T. Levato, V. Lollo, E. Pace, N. Pathak, A. Rossi, L. Serafini, G. Turchetti, C. Vaccarezza, P. Valente, C. Vicario, L. Gizzi. ”A self-injection acceleration test experiment for the FLAME laser”, *Radiation Effects and Defects in Solids* **165**, 787 (2010).